# New Insights into the Function of the APC/C Subunit, APC5

and

# Development of a Spheroid Model to Investigate Heterogeneity in Glioblastoma

By

Leigh O'Connor

This project is submitted in partial fulfilment of the requirements for the award of Master of Research (MRes)

School of Cancer Sciences
College of Medical and Dental Sciences
University of Birmingham
May 2014

# New Insights into the Function of the APC/C Subunit, APC5

This project is submitted in partial fulfilment of the requirements for the award of Master of Research (MRes)

# ABSTRACT

The Anaphase Promoting Complex/Cyclosome (APC/C) regulates progression through mitosis by targeting important cell cycle regulators for ubiquitin-mediated proteolysis. It consists of at least 13 different subunits; the function of many of which is unknown. Recent work in the Turnell laboratory has suggested that protein levels of the APC/C subunit APC5 vary during mitosis. APC5 has also been implicated in additional functions, aside from cell cycle regulation, in chromatin structure and transcriptional regulation. The aim of this study was to understand further the roles of APC5 in APC/C regulation and its relationship with chromatin. Here, I show that APC5 is degraded during mitosis in a spindle assembly checkpoint-independent manner. However, I also determined that a small proportion of the APC5 protein remained during mitosis, indicating distinct pools are present within the cell, possibly performing different functions. I found that APC5 binds to chromatin and Western blotting results suggest the presence of post-translationally modified APC5 associated with chromatin. I used mass spectrometric analysis of proteins immunoprecipitated with APC5 from chromatin fractions to discover a number of novel binding partners, including proteins involved in chromatin modification/transcription regulation, mRNA processing and translation, suggesting potential new functions for the APC/C.

# CONTENTS

# 1. INTRODUCTION

The cell cycle, or the process of cell division, consists of 5 stages: G0, G1, S, G2 and M (Fig. 1). DNA replication occurs during S phase and the cell undergoes mitosis and division during M phase. G1 and G2 are the 'gap' phases of the cycle, when the cell responds to environmental signals and commits to the cell cycle (G1) and when the cell prepares for entry to mitosis (G2). G0 is the 'resting' phase, which occurs when the cell is quiescent. Checkpoints exist at multiple points through the cycle, which sense aberrant or incomplete cell cycle events and signal to arrest the cycle, e.g. to ensure DNA is correctly replicated and repaired before the cell divides. Progression through the cell cycle is driven by the cyclin-dependent kinase (Cdk) family of serine/threonine kinases, along with their regulatory partners, cyclins. Although the levels of Cdks are constant, the levels of different cyclins vary throughout the cell cycle, allowing the formation of distinct complexes at each stage to trigger different events and ensure sequential progression through the cycle (Williams and Stoeber, 2011; Lim and Kaldis, 2013).

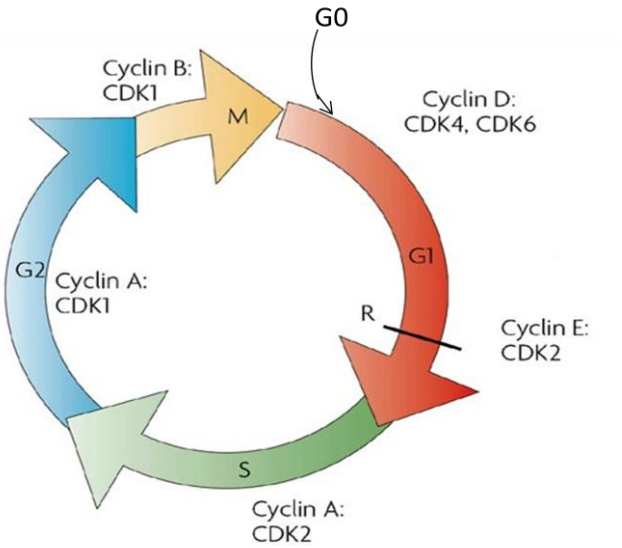


**Figure 1 – Diagram of the Cell Cycle**
The cell cycle is split into five stages: G0, G1, S, G2 and M, as shown. A number of checkpoints are present to control cell cycle progression, including the restriction point (R) at the end of G1 after which the cell will irreversibly enter the cycle. The cyclin-Cdk pairs present at each stage are shown. (Dehay and Kennedy, 2007).

Cell division needs to be tightly controlled to ensure each daughter cell inherits the correct number of chromosomes. This involves limiting the presence of cell cycle regulators, including cyclins, to only when their functions are required, both by regulating their transcription and through protein degradation, which guarantees the cell cycle is irreversible and progresses in the correct order (Benanti, 2012). Cell cycle-mediated protein degradation mainly occurs via the ubiquitin-proteasome pathway. This pathway utilises a series of enzymes to promote ubiquitination. Initially, the E1-activating enzyme catalyses activation of ubiquitin in an ATP-dependent step, before binding of ubiquitin to a cysteine in E1 via a thio-ester bond. Ubiquitin is transferred to an E2 ubiquitin-conjugating enzyme and covalently linked via a cysteine in the active site. The E2 enzyme then acts with an E3 ubiquitin ligase, to transfer the ubiquitin to a lysine residue in the target

protein. This process can be repeated to give polyubiquitinated proteins that are then targeted by the 26S proteasome for degradation (Fig. 2) (Hershko and Ciechanover, 1998). There is also evidence that multiple mono-ubiquitination can act as an alternative degradation signal, e.g. for cyclin B1 (Dimova et al., 2012). The E3 enzyme provides the substrate specificity in the reaction and thus, it is at this step that most regulation of the pathway occurs (Deshaies and Joazeiro, 2009).

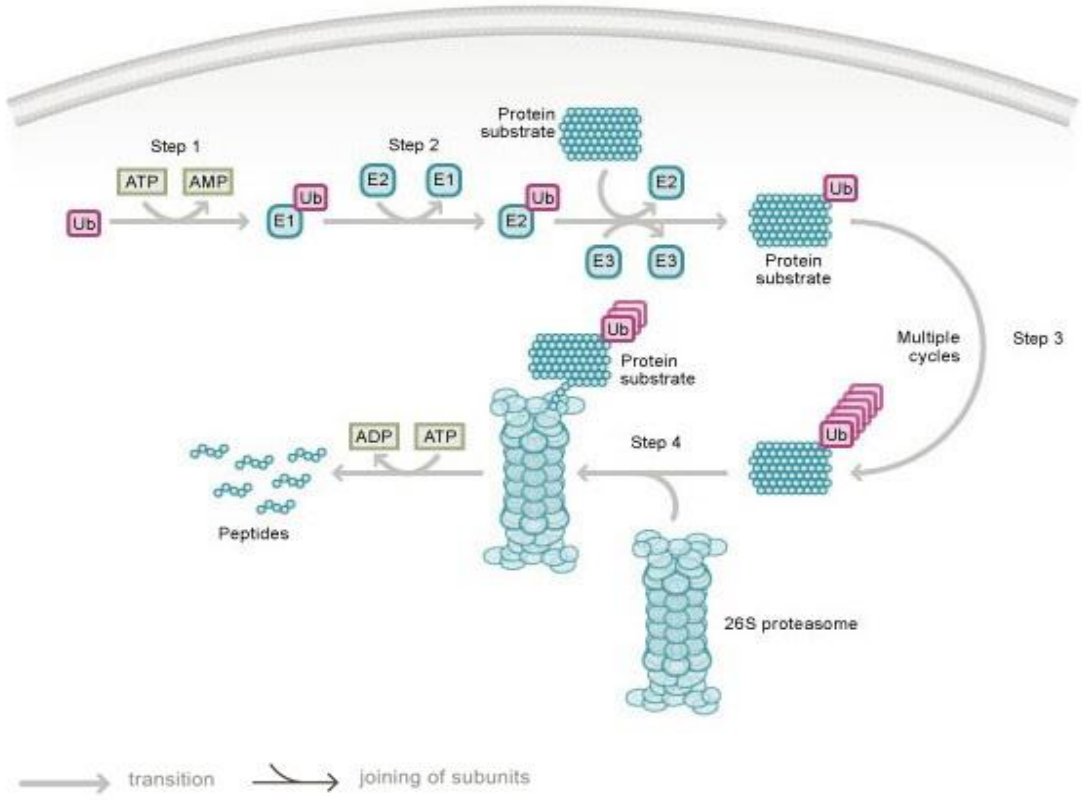


**Figure 2 – Ubiquitin-Proteasome Pathway**
Diagram illustrating the polyubiquitination process to target proteins for degradation. Ubiquitin is first activated by an ubiquitin-activating enzyme, E1 (step 1), before the activated ubiquitin is transferred to an ubiquitin conjugating enzyme, E2 (step 2). In step 3, ubiquitin is attached to the target protein by an E3 ubiquitin ligase and repeated to give a polyubiquitinated substrate, before it is degraded by the 26S proteasome in step 4 (Corn, 2007).

The anaphase promoting complex or cyclosome (APC/C) is an E3 ubiquitin ligase that targets many cell cycle regulators for degradation to control mitotic

progression and entry into S phase (Sudakin et al., 1995; Clijsters et al., 2013). The APC/C targets substrates for ubiquitin-mediated proteolysis in a temporally-coordinated manner in order to promote cell cycle progression (Fig. 3). Currently, the human APC/C is known to have at least 55 substrates, but the true figure is estimated to be more than 100 (Meyer and Rape, 2011). It becomes activated upon Nuclear Envelope Breakdown (NEBD), when it targets cyclin A and Nek2A (den Elzen and Pines, 2001; Hames et al., 2001). At metaphase, it directs the ubiquitination of Securin and cyclin B1 to enable metaphase-anaphase transition (Stemmann, 2001; Clute and Pines, 1999), before targeting Aurora kinases (as well as cyclin B1) to permit chromatid segregation and cytokinesis (Floyd et al., 2008). It remains active in G1 to maintain low levels of mitotic Cdk activity and allow for DNA replication licensing (Clijsters et al., 2013).

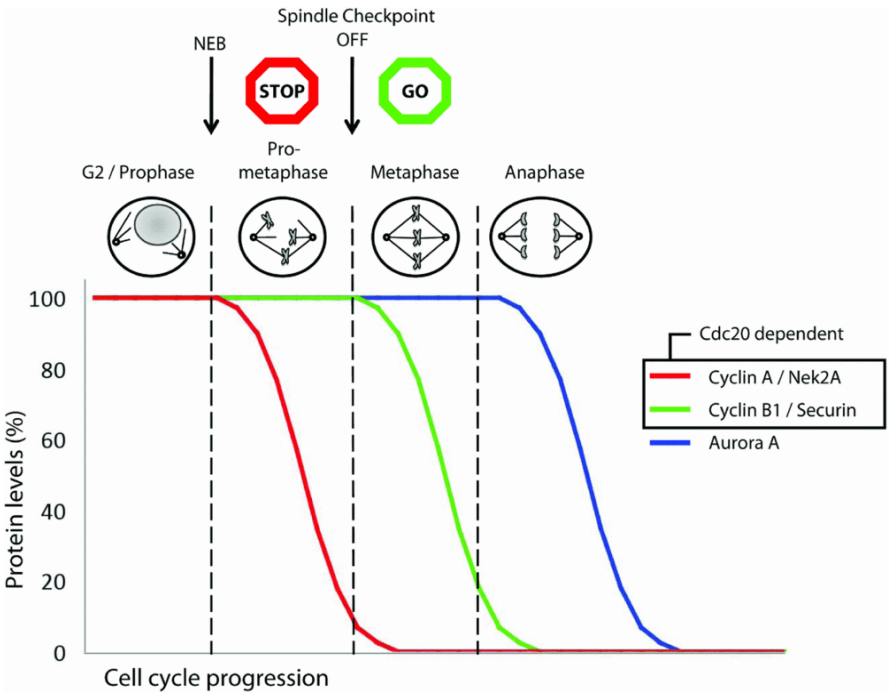


**Figure 3 – Temporal targeting of APC/C substrates (van Zon, 2010)**
Diagram illustrating the role of the APC/C in cell cycle progression, showing at which stage specific substrates are targeted and their sensitivity to spindle checkpoint activation.

The APC/C interacts with two different co-activators: Cdc20 from pro-metaphase to anaphase and Cdh1 from anaphase through G1 (Sudo et al., 2001). Studies have shown that these proteins function both to activate the APC/C (Fang et al., 1998) and to provide substrate specificity for the ubiquitination reaction, as Cdc20 and Cdh1 bind substrates independently of the APC/C (Pfleger et al., 2001). Substrates are recognised via specific sequences called degrons, most commonly the D box (RxxLxxI/VxN/D/E) and KEN box (KENxxxN/D) although there are many others (Glotzer et al., 1999; Pfleger et al., 2000). The co-activators have some preference for the specific degrons, with Cdc20 more dependent on the D box for substrate-binding and Cdh1 more dependent on the KEN box (Zur and Brandeis, 2002). The different, albeit overlapping, substrates of the co-activators means that different cell cycle regulators are degraded in the separate phases of APC/C-Cdc20 and APC/C-Cdh1 activity, giving an ordered progression through the cell cycle (Barford, 2011). However, Cdh1 is not essential for division and only the Aurora kinases are stabilised in cells not expressing Cdh1 (Izawa and Pines, 2011). Therefore, there must be other factors involved in the temporal regulation of substrate degradation.

Part of the answer likely lies in the structural complexity of the APC/C. It consists of at least 13 different protein subunits and has been studied by numerous biochemical and structural analyses, including X-ray crystallography of individual subunits (Wendt et al., 2001; Zhang et al., 2010), nano-electrospray mass spectrometry to analyse molecular weights and stoichiometry (Schreiber et al., 2011) and cryo-electron microscropy (cryo-EM) of reconstituted APC/C from an

overexpression system (Schreiber et al., 2011 [Fig. 4]). The APC/C can be subdivided into three subcomplexes. The first structural component is the catalytic subcomplex, consisting of APC2 (a Cullin-related ubiquitin ligase protein) and APC11 (a RING-type ubiquitin ligase) that form a tight complex and are alone sufficient to catalyse ubiquitination (Tang et al., 2001). It also includes APC10, which seems to form a co-receptor for the substrate degron (along with the co-activator), shown by a density bridge linking APC10, co-activator and substrate in the cryo-EM structure (Schreiber et al., 2011). The second subcomplex is composed of 3 or 4 layers of subunits containing 34-residue tetratricopeptide repeats (TPRs) – APC3, APC6, APC8 and APC7 in higher eukaryotes. The TPR complex mediates co-activator binding to the APC/C. Finally, APC1, APC4 and APC5 form the platform of the APC/C and connect the catalytic and TPR domains. The APC/C also interacts with two E2 enzymes – UbcH10 (needed for initiation) (Kirkpatrick et al., 2006) and UbE2S (required for elongation) (Garnett et al., 2009). Although the role of some of these subunits has recently been elucidated, the function of many and their possible roles in regulation of the APC/C are, as yet, unknown.

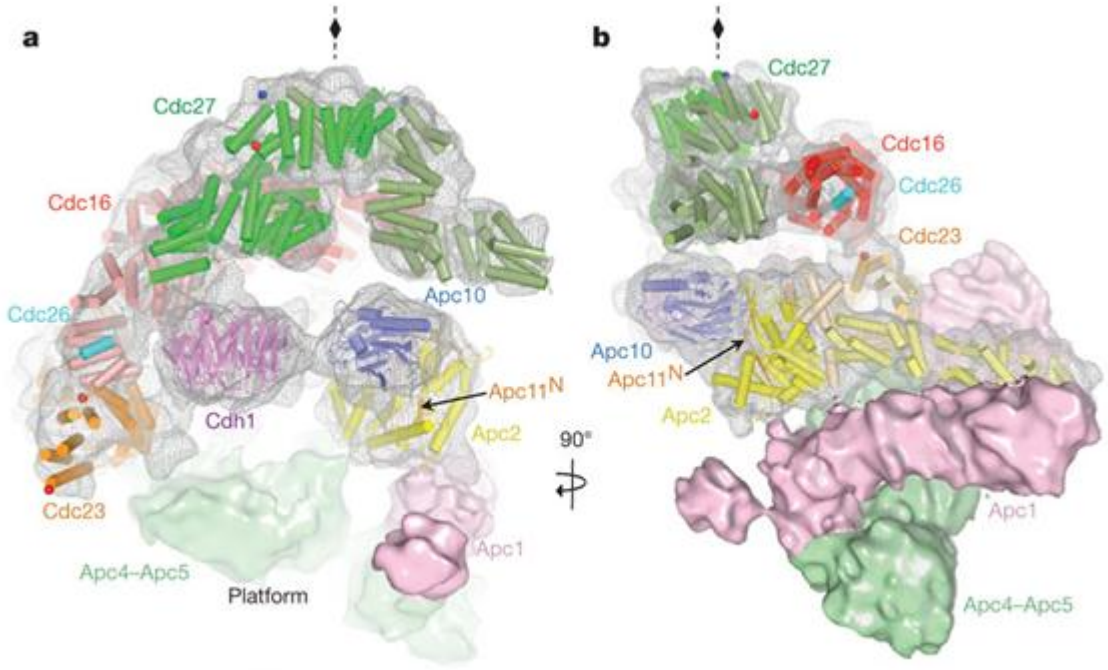


**Figure 4 – Model structure of the APC/C**
The structure of the yeast APC/C modelled on X-ray crystallographic structures of individual subunits docked onto the cryo-EM structure of the entire complex (Schreiber et al., 2011).

Another way that the timing of APC/C substrate ubiquitination is regulated is by the Spindle Assembly Checkpoint (SAC). During mitosis, Securin holds sister chromatids together, preventing the onset of anaphase (Funabiki et al., 1996). Cdk1-cyclin B1 phosphorylates and inhibits Separase and Cdh1, allowing time for the chromosomes to attach to the spindle and correctly align so that each chromatid is attached to opposite poles of the cell (Gorr et al., 2005). APC/C-Cdc20 then targets Securin and cyclin B1 for degradation, allowing progression into anaphase (Zur and Brandeis, 2001). However, the activity of APC/C-Cdc20 in pro-metaphase is inhibited until all chromatids are attached to the mitotic spindle (van Zon and Wolthuis, 2010). An unattached kinetochore triggers activation of the SAC to delay onset of anaphase and ensure correct segregation of chromosomes. This is mediated by the Mitotic Checkpoint Complex (MCC),

composed of the proteins Mad2, Mad3/BubR1, Bub3, which form an inhibitory complex with Cdc20 (Braunstein et al., 2007). Thus, this pathway ensures the APC/C functions in a timely manner during the cell cycle.

However, there are some substrates that escape the SAC, such as cyclin A and Nek2A which are degraded upon NEBD. Cyclin A associates with Cdk1 and Cdk2 to support progression through S and G2 phases (Pagano et al., 1992), while Nek2A is a centrosomal kinase required for the formation of the mitotic spindle (Fry et al., 2002). Live cell imaging first revealed that cyclin A begins to be degraded shortly after nuclear envelope breakdown (den Elzen and Pines, 2001), with Nek2A behaving similarly (Hames et al., 2001), and so are not affected by the SAC. These two proteins do not contain the conventional degrons and instead have different modes of binding to the APC/C. Cyclin A binds, via its N-terminus, to Cdc20 with high enough affinity to out-compete binding of BubR1. It also binds to Cks, the cyclin-dependent kinase cofactor, which recruits the complex to the APC/C for ubiquitination (Di Fiore and Pines, 2010). Nek2A contains a Met-Arg dipeptide C-terminal tail, similar to that found on the co-activators, allowing it to bind directly to the APC/C, even without Cdc20 (Hayes et al., 2006). Therefore, the MCC only prevents degradation of substrates with true D boxes that are dependent on Cdc20 for recruitment. Depletion of specific APC/C subunits using siRNA also revealed that Cdc20 binds to different sites on the APC/C depending on the SAC. When the SAC is active, only APC8 is necessary, whereas both APC3 and APC8 are required when the SAC is satisfied. Furthermore, APC10 is only necessary for the degradation of cyclin B1 and Securin, not for cyclin A,

suggesting that Cdc20 (at its position bound to APC3 and APC8) works with APC10 to provide a binding site for SAC-sensitive substrates only (Izawa and Pines, 2011; Fig. 5). This level of complexity allows the APC/C to actively regulate substrate specificity and timing of degradation during the cell cycle.

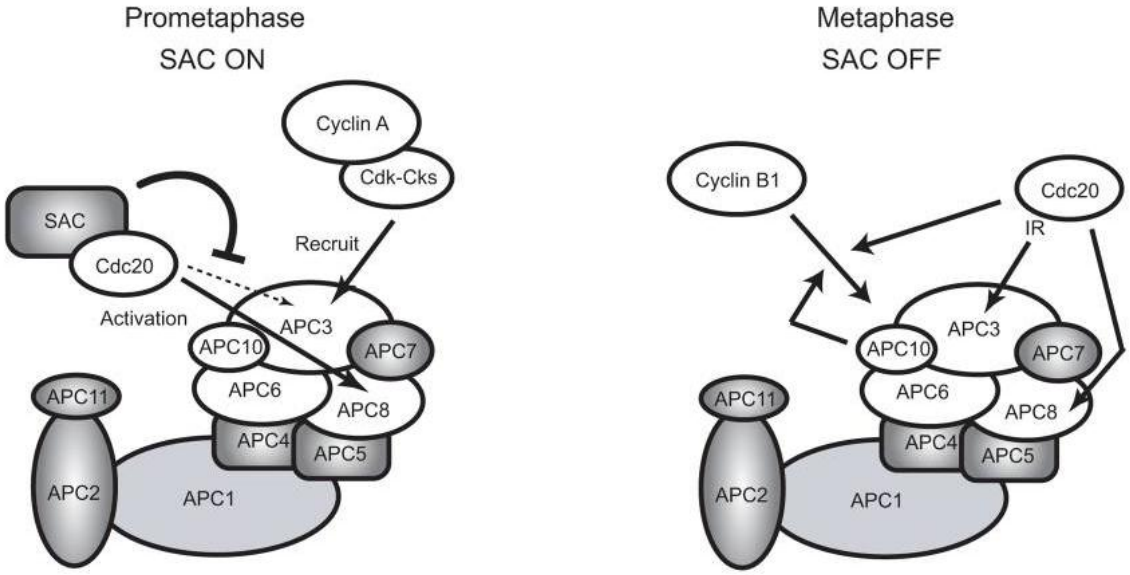


**Figure 5 – APC/C regulation during early mitosis**
When the SAC is active during prometaphase (left), the APC/C is inhibited by Cdc20 binding the MCC. During this stage, Cdc20 binds to the APC/C via APC8 and substrates such as cyclin A and Nek2A, which bind directly to the APC/C, can be targeted. In metaphase when the SAC has been satisfied (right), both APC3 and APC8 are required for Cdc20 binding and APC10 along with Cdc20 forms a co-receptor for APC/C substrates such as cyclin B1. The MCC proteins may prevent Cdc20 binding to APC3 and so prevent formation of the binding site for SAC-sensitive substrates while the SAC is active (Izawa and Pines, 2011).

The APC/C is subject to post-translational modifications (PTMs). It well known that the APC/C is activated by cyclin B1-CDK1 after entry to mitosis by phosphorylating the APC/C, mapped to sites in subunits APC3, APC6 and APC8 in *Saccharomyces cerevisiae* by mutagenesis (Rudner and Murray, 2000). It has been shown that this phosphorylation (the mitotic form) increases binding of the

co-activator Cdc20 (Kramer et al., 1998). More recently, a total of 71 phosphorylation sites on the APC/C have been identified, which seem to vary with the use of different mitotic arrest drugs (Sheen et al., 2008), indicating a role of phosphorylation in regulating of APC/C activity. Additionally, phosphorylation of Cdc20 (by the MCC) and Cdh1 inhibits their binding to the APC/C (Primorac and Musacchio, 2013). It may be that more phosphorylation sites are still to be found and recently, the Turnell group has found acetylation of APC/C subunits (unpublished data), showing there is more to be done to determine the role of PTMs in APC/C regulation.

Recent studies have reported that the APC/C has roles in the cell aside from cell cycle regulation. Experiments in yeast have suggested that the APC/C, specifically APC5, is required for chromatin assembly (Harkness et al., 2005). Multiple APC/C subunit mutants exhibited impaired total histone H3 levels and were also linked to changes in H3 modifications that indicated that specific histone acetyltransferases are required for APC/C-dependent cell cycle progression (Turner et al., 2010). In human cells, the APC/C subunits APC5 and APC7 were found to interact with the transcriptional activators CBP and p300 (Turnell et al., 2005). APC5 and APC7 enhanced CBP/p300-dependent transcription and were also found associated with CBP/p300-regulated promoters. Knockdown of APC5 and APC7 led to decreased H4 acetylation at promoters, showing they stimulate CBP/p300 acetyltransferase activity and thus affect transcription (Turnell et al., 2005). These data suggested that different APC/C subunits could have distinct functions in the cell.

### *1.1 Hypothesis and Aims*

The aim of the present study was to determine more about the specific functions of the individual APC/C subunits – specifically APC5. Unpublished observations in the Turnell laboratory suggest that APC5 protein levels change during the cell cycle and that APC5 contains potential degrons within its primary sequence. It was hypothesised that the timely changes in APC5 protein levels are important for the regulation of mitotic progression, but the molecular basis of the control of APC5 levels is currently unknown. To further understand the roles of APC5 in the cell, the aims this project were as follows:

1. Validate APC5 protein levels in mitosis
2. Investigate the stability of APC5 in mitosis
3. Develop a Tetracycline-inducible FLAG-APC5 system to validate results from endogenous proteins
4. Investigate the role of APC5 phosphorylation in regulation of APC5 protein levels
5. Identify APC5 binding partners in chromatin to learn more about the function of APC5 in chromatin

# 2. MATERIALS AND METHODS

*2.1 Cell Culture*

HeLa cells were grown in Dulbecco's Modified Eagle's Medium (DMEM), modified with HEPES and supplemented with 2 mM L-glutamine and 8% (v/v) foetal calf serum (FCS), and incubated at 37°C until confluent. For cell subculture, the medium was removed and the cells washed in PBS, before incubating at 37°C with trypsin solution (TrypLE express, Gibco) until cells had detached from the dish. Trypsin was inactivated with the addition of DMEM and the cells harvested by centrifugation (1500 rpm, 5 mins). The pellet was resuspended in DMEM and plated at the appropriate cell density.

*2.2 Cell Synchronisation*

HeLa cells were incubated overnight in DMEM (supplemented with 8% [v/v] FCS and 2 mM L-glutamine) and the appropriate concentration of inhibitor: 400 ng/ml nocodazole; 1 µM taxol; 9µM RO3306. Mitotic cells were harvested by shake-off, followed by centrifugation (1500 rpm, 5 mins) and the pellet washed in cold saline and resuspended in lysis buffer (9 M urea, 50 mM Tris [pH 7.4] and 0.15 M β-mercaptoethanol). Asynchronous and G2/M-arrested cells were washed with cold saline and harvested by scraping after incubation for 5 mins with lysis buffer.

Where appropriate, a protein synthesis inhibitor (anisomycin,100 µM) or proteasome inhibitor (MG132, 10 µM) was added approximately 18 hours following addition of the cell cycle inhibitor and the cells harvested at set time points.

For inhibitor release, cells were washed twice in DMEM (8% FCS) and fresh medium added, before harvesting (as above) at set time points following release.

*2.3 Plasmid Amplification and Purification*

The plasmid DNA (pcDNA5/FRT-3xFLAG-APC5-TR) was first transfected into E. coli cells that are recombination- and endonuclease A- deficient. For bacterial transformation, 100 ng of the purified DNA was mixed with 20 µl DH5α E. coli and incubated at 42°C for 1 min to heat shock the cells. 0.5 ml LB broth was added to the bacteria and thereafter incubated at 37°C for 45 mins, before selecting for transformants on LB agar plates containing 100 µg/ml ampicillin. Bacterial cells were transferred to 5 ml LB broth (with 5 µl ampicillin) and grown for 5 hours before incubating in 250 ml broth overnight. The plasmid was purified following the manufacturer's instructions (Sigma maxiprep). 0.1 volume sodium acetate (pH 5.0) and 0.7 volume isopropanol was added and centrifuged for 30 mins at 9000 rpm. The pellet was washed twice in 70% ethanol, before resuspension in the appropriate volume of water to dissolve the DNA. DNA concentration was determined using a nanodrop (Thermo Scientific Nanodrop 2000).

*2.4 Transfection*

HeLa Tetracycline-responsive Flp-In cells (Life Technologies), that have a Flp Recombination Target (FRT) site integrated into the genome, were grown to confluence and transferred to OptiMEM (Gibco) low serum medium. Cells were co-transfected using lipofectamine 2000 (Life Technologies) with the

pcDNA5/FRT-3xFLAG-APC5-TR vector and a Flp recombinase expression plasmid pOG44, according to the manufacturer's protocol of the Flp-In system (Life Technologies). Transfected cells were subjected to blasticidin/hygromycin selection and single colonies selected to give monoclonal cell foci, as well as collecting all cells on a single plate to obtain polyclonal cell lines. The expression vector was induced with the addition of either 1 µg/ml or 0.1 µg/ml Doxycycline (a stable tetracycline analogue).

*2.5 Western Blotting*

Cell lysates were sonicated (Microson Ultrasonic Cell Disrupter) for 10-15 sec at power setting 4 and centrifuged for 20 min at 13000 rpm. The protein concentration was determined using a Bradford assay (Bio-Rad) and 50 µg of each protein sample was mixed with an equal volume of loading buffer (1 volume of 10% w/v SDS to 2 volumes of 9 M urea in 50 mM Tris (pH 7.4) plus 5% (v/v) β-mercaptoethanol), before boiling for 5 min at 95°C.

The proteins were separated using sodium dodecyl sulphate-polyacrylaminde gel electrophoresis (SDS-PAGE) and subsequently transferred to nitrocellulose paper using a wet-transfer method. The membranes were washed using TBST (0.1% [v/v] Tween™ 20, 0.2 M sodium chloride [NaCl] and 0.02 M Tris [pH 7.6]) and incubated with a blocking agent (5% powered milk or 5% BSA in TBST) for at least 30 min. The membranes were placed in bags, sealed with the primary antibody (made to the correct dilution in the appropriate blocking agent) (Table 1) and left on a rocker for a minimum of 3 hours. The blots were washed in TBST to remove

any unbound antibody and incubated with the appropriate secondary antibody for 2-3 hours on a shaker. Blots were washed with TBST on an orbital shaker every 15 min for 1 hr, before the addition of enhanced chemiluminescent (ECL) substrate with hydrogen peroxide for 1-2 min. The blots were exposed to x-ray film for the appropriate time and developed.

| **Antibody** | **Dilution** | **Species** | **Blocking Agent** | **Supplier** |
|---|---|---|---|---|
| Actin | 1:20000 | Mouse | Milk | Sigma |
| APC3 | 1:1000 | Mouse | Milk | BD Biosciences |
| APC5 | 1:1000 | Mouse | Milk | Home-made mAB |
| APC7 | 1:2000 | Rabbit | Milk | Home-made pAB |
| Cdc20 | 1:1000 | Mouse | Milk | Santa Cruz |
| Cdh1 | 1:1000 | Mouse | Milk | Santa Cruz |
| Cyclin A | 1:1000 | Mouse | Milk | Santa Cruz |
| Cyclin B1 | 1:1000 | Mouse | Milk | CR-UK |
| FLAG | 1:1000 | Mouse | Milk | Sigma |
| Geminin | 1:500 | Rabbit | Milk | Santa Cruz |
| H4K8Ac | 1:500 | Rabbit | Milk | Life Technologies |
| Nek2A | 1:500 | Mouse | Milk | Abcam |
| Phospho-H3 | 1:500 | Rabbit | BSA | Cell Signalling |
| TIF1γ | 1:1000 | Rabbit | Milk | Home-made pAB |
| UbcH10 | 1:500 | Rabbit | Milk | Home-made pAB |

**Table 1 – Antibodies used in Western Blotting**

*2.6 RNA Preparation and RT-qPCR*

RNA was purified using the Qiagen RNeasy Mini Kit, according to manufacturer's instructions. Briefly, HeLa cells were harvested (as above) using the lysis buffer provided (Buffer RLT). The cells were homogenised by centrifugation at 13200

rpm for 2 mins in a QIAshredder spin column (cat. no. 79654). One volume of 70% ethanol was added and the sample transferred to an RNeasy spin column, before centrifugation at 12000 rpm for 15 secs to leave nucleic acids bound to the column. The sample was then washed in Buffer RW1 and centrifuged at 12000 rpm for 15 secs, before DNase1 (in Buffer RDD) was added to digest DNA. The sample was again washed with Buffer RW1 and centrifuged (12000 rpm, 15 secs), followed by two washes with Buffer RPE, the first centrifuged as before and the second for 2 mins at 12000 rpm. The RNA was eluted from the column by adding 50 µl of RNase-free water and centrifuging for 1 min at 12000 rpm.

The RNA concentration was measured using a nanodrop (Thermo Scientific Nanodrop 2000) and reverse transcription PCR (RT-PCR) performed with the Promega Reverse Transcription System. Water was added to 500 ng RNA to a final volume of 4.9 µl and incubated at 70°C for 10 mins. A master mix was prepared using: 2 µl $MgCl_2$, 1 µl 10x RT buffer, 1 µl 10 mM dNTPs, 0.25 µl RNasin Ribonuclease Inhibitor, 0.5 µl random primers and 0.3125 µl AMV Reverse Transcriptase, per sample, and 5 µl added to each RNA sample. The tubes were incubated at room temperature for 10 mins and one PCR cycle ran at 42°C for 1 hour, 95°C for 5 mins and 4°C for 5 mins. Water was then added to the generated cDNA to give a final concentration of ~10 ng/µl.

A master mix of 10 µl Taqman 2x MasterMix (Life Technologies), 1 µl Taqman Assay Probe and 7 µl water was added to 2 µl cDNA. The probes used were for the genes: APC5 (FAM) and GAPDH (FAM) as a control housekeeping gene. The

qPCR reaction was performed (7500 Real Time PCR System, Life Technologies) and the cycle number (Ct) for each sample analysed. The GAPDH Ct was subtracted from the corresponding APC5 Ct to obtain the δCt and the average δCt for asynchronous cells subjected from the result, to analyse any changes compared to asynchronous cells. The value was then converted to a percentage change in gene expression.

*2.7 Chromatin Isolation*

The procedure was carried out as previously described (Wysocka et al., 2001). Cells were washed twice with PBS then harvested by scraping and centrifuged at 1000 rpm for 2 minutes. The cell pellet was resuspended in Buffer A containing 10 mM HEPES (pH 7.9), 10 mM KCl, 1.5 mM $MgCl_2$, 0.34 M sucrose, 10% (v/v) glycerol, 1 mM DTT and 0.1% (v/v) Triton X-100. The samples were incubated on ice for 8 minutes, before centrifugation (1300 x g, 4°C, 5 min). The supernatant was isolated and centrifuged at 20000 x g, 4°C, for 5 min to give the cytoplasmic fraction, while the pellet was washed with Buffer A and incubated for 30 min in Buffer B (3 mM EDTA, 0.2 mM EGTA, 1 mM DTT) to lyse the nuclear membrane. It was then centrifuged at 1700 x g, 4°C, 5 min, to obtain the nucleoplasmic fraction (supernatant) and the chromatin fraction (pellet). A proportion of the chromatin fraction was then washed in a salt solution to elute chromatin-binding proteins and resuspended in lysis buffer or RIPA buffer (25mM Tris-HCl (pH 7.6), 150mM NaCl, 1% [v/v] NP-40, 1% [w/v] sodium deoxycholate, 0.1% [v/v] SDS) when followed by immunoprecipitation experiments.

*2.8 Immunoprecipitation - Mass Spectrometry (IP-MS)*

Protein samples, prepared in NETN lysis buffer (250 mM NaCl, 20 mM Tris-Cl (pH 8.0), 0.5 mM EDTA, 0.5 % [v/v] Nonidet P-40 [NP-40]), were split into two: antibody was added to one tube and the other left without antibody to act as a control for non-specific binding. The samples were incubated, spinning, overnight at 4°C, before the addition of 50µl protein G sepharose beads and incubation for 3 hours at 4°C on a rotator. The beads were spun down and washed 4 times with NETN lysis buffer and sample buffer added containing 50 mM DTT to elute the protein from the beads. The samples were boiled for 5 min at >80°C, spun down briefly and loaded onto NuPAGE 4-12% Tris/Bis-tris gels (Life Technologies) to separate the proteins. The gels were incubated with colloidal coomassie reagent overnight to stain the protein bands and then washed several times in 1% (v/v) acetic acid to remove background stain.

Individual slices of the gel were then cut out and washed twice in 50% (v/v) acetonitrile/ 50 mM ammonium bicarbonate for 45 min to remove the SDS and stain from the gel. The gel was incubated in 50 mM DTT/10% (v/v) acetonitrile/ 50 mM ammonium bicarbonate at 56°C for 1 hr, followed by incubation in 100 mM iodoacetamide/10% (v/v) acetonitrile/50 mM ammonium bicarbonate for 30 min in the dark. The gel slices were washed three times for 15 min in 10% (v/v) acetonitrile/40 mM ammonium bicarbonate and dried using a vacuum centrifuge. 10% (v/v) acetonitrile/40 mM ammonium bicarbonate was added to a trypsin solution to activate the enzyme, before incubating with the samples overnight. Any liquid, containing the peptides from the gel, was then transferred to a new

tube, the gel incubated with 3% (v/v) formic acid on a shaker for 1 hr and the process repeated. The peptides were then dried using a vacuum centrifuge, resuspended in 1% (v/v) acetonitrile/1% (v/v) formic acid and run on a quadrupole time-of-flight (QTOF) mass spectrometer (maXis Impact, Bruker). Fragmentation data produced were then searched against a theoretical database (Mascot, Matrix Science) and analysed on ProteinScape (Bruker).

# 3. RESULTS

*3.1 APC5 Protein Levels are Reduced During Mitosis*

Previous unpublished studies have suggested that APC5 protein levels vary during mitosis. To validate changes in APC5 levels in mitosis, HeLa cells were treated with nocodazole, a spindle inhibitor, to synchronise cells in the prophase stage of mitosis. The cells were then released from nocodazole inhibition, cells harvested at set time points and APC5 protein levels assessed by Western blotting (Fig. 6).

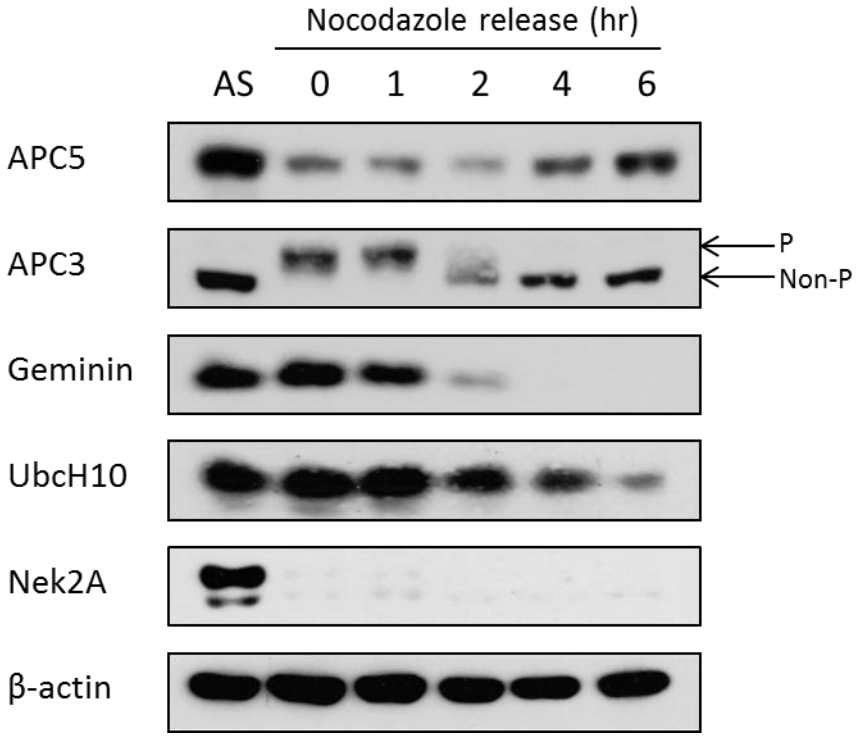


**Figure 6 – Levels of APC/C subunits and substrates in mitosis**
Cells were incubated with nocodazole for 18 hours and released into normal medium, before harvesting at set time points between 0 and 6 hours, as shown. The cells were lysed, proteins quantified and a Western blot performed to look at the relative levels of both APC/C subunits and its known substrates at each time point, compared to those found in asynchronous cells (labelled as 'AS'). P – phosphorylated.

The results show a decrease in the levels of APC5 in mitosis, which then begin to increase as the cells exit mitosis. APC3 is present in its phosphorylated mitotic form during the early time points, verifying that the cells are in mitosis. Furthermore, the levels of known APC/C substrates, Geminin and Nek2A, are seen to decrease during the time course, showing that the APC/C is still active despite the reduction in APC5 protein. These data indicate that APC5 protein levels are reduced during mitosis. However, there is still some protein present that is resistant to loss, suggesting that different pools of APC5 could be present in the cell to perform distinct functions.

*3.2 Loss of APC5 Protein is not SAC-Sensitive*

The present study has shown APC5 protein levels are reduced during mitosis (Fig. 6). In order to determine the exact timing of APC5 degradation, HeLa cells were treated with RO3306 (a Cdk1-inhibitor), nocodazole or taxol (a spindle-stabiliser) to synchronise cells at different stages in mitosis (i.e. at G2/M, in pro-metaphase before spindle assembly and in anaphase before spindle disassembly). Western blotting was used to compare the levels of APC5 in each of the inhibitor-treated cells (Fig. 7).

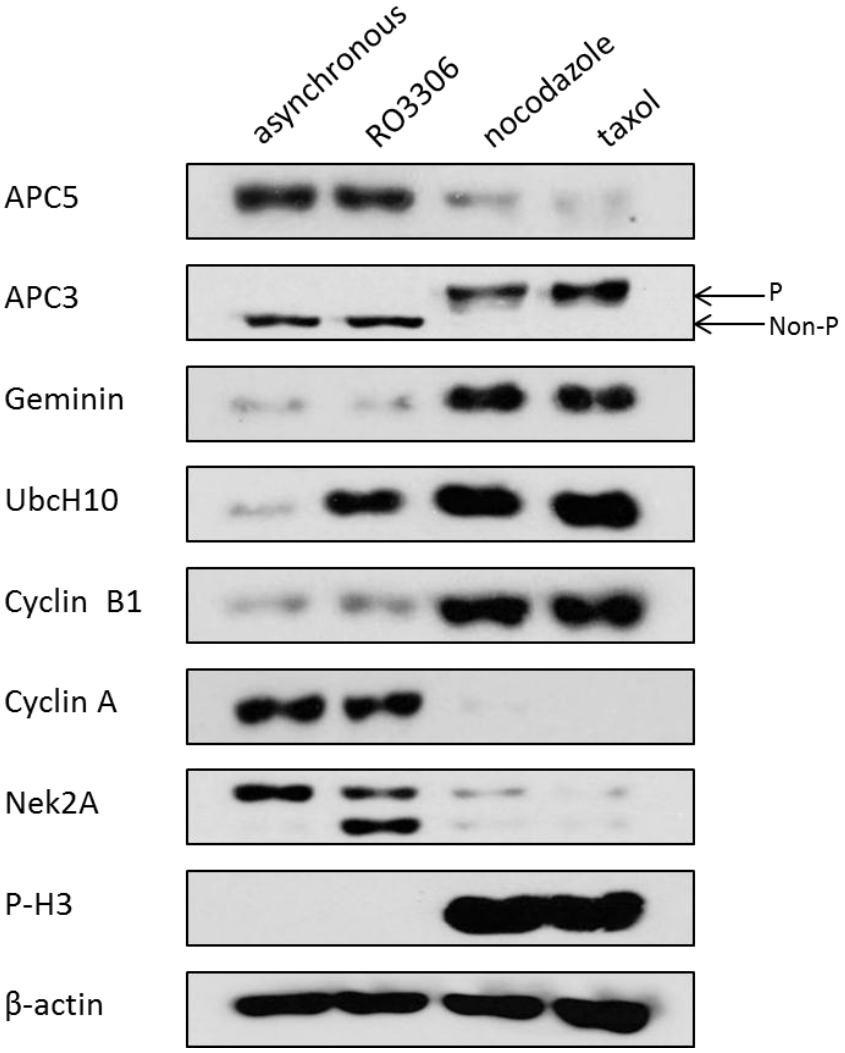


**Figure 7 – Levels of APC/C substrates and subunits at different stages in the cell cycle**
HeLa cells were grown in normal media with the addition of RO3306, nocodazole or taxol for 18 hours, along with asynchronous cells with no cell cycle inhibitor. The cells were harvested and lysed, and a Western blot performed to analyse the relative levels of APC/C substrates and subunits at varying stages of the cell cycle, compared to asynchronous. Phospho-histone H3 (Ser10) (P-H3) was used to indicate the cell cycle stage, being present during mitosis, and β-actin used as a loading control.

The results show that APC5 levels are reduced compared to asynchronous and RO3306-treated cells in both nocodazole- and taxol-synchronised cells. Moreover, the levels of APC5 follow a similar pattern to that shown by SAC-

insensitive APC/C substrates, cyclin A and Nek2A, as opposed to SAC-dependent substrates such as cyclin B1 and Geminin. This suggests that APC5 protein levels are not SAC-sensitive. It may be that APC5, with its possible degron sequences, is marked for degradation by the APC/C and thus is a way to self-regulate APC/C. APC5 does not seem to contain a C-terminal MR dipeptide sequence like Nek2A and a BLAST search revealed no significant sequence similarity between APC5 and the N-terminal APC/C-binding region of cyclin A. Thus, APC5 may be degraded by a different mechanism.

### *3.3 APC5 Protein Stability*

APC5 protein levels are seen to decrease during mitosis. To assess whether this is an effect at the level of protein stability, HeLa cells were treated with nocodazole for 18 hours to synchronise cells in mitosis, then anisomycin, a protein synthesis inhibitor, was added. The levels of APC5 were monitored at set time points to determine the protein half-life in mitotic cells compared to the protein half-life in asynchronous cells (Fig. 8a).

The results, however, showed little change in APC5 levels following anisomycin treatment. This was a surprising result as the levels of APC5 have been shown to decrease during mitosis, but it is likely that the APC5 level had already reached its minimum during nocodazole synchronisation, before anisomycin was applied and thus no change was seen at these time points.

Therefore, the experiment was repeated using RO3306 to synchronise HeLa cells at the G2/M transition. Cells were simultaneously released, to progress into mitosis, and anisomycin added to analyse APC5 half-life from mitotic entry. Some cells were not released and anisomycin added while still inhibited to act as the control (Fig. 8b).

Western blotting again showed little change in APC5 levels over time. This indicates that APC5 levels are not altered following RO3306 release, but more work is needed to validate this. An explanation for the mechanisms by which APC5 might be reduced during mitosis will be considered in the discussion.

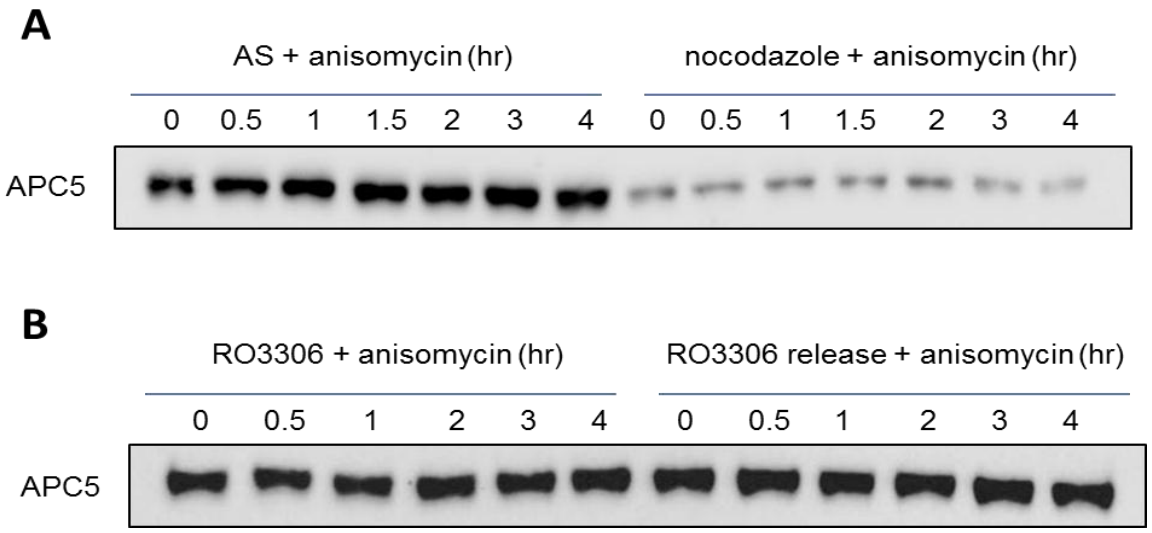


**Figure 8 – APC5 protein stability in mitosis**
**(A)** HeLa cells were grown until confluent and were either treated with nocodazole to synchronise in mitosis or were left untreated to remain asynchronous (AS). After 18 hours, 100 µM anisomycin (a protein synthesis inhibitor) was applied to the cells and the cells harvested at set time points from 0 hour to 4 hours. Western blotting was used to monitor the levels of APC5 over time in asynchronous compared to mitotic cells. **(B)** HeLa cells were treated with RO3306, a Cdk1 inhibitor to synchronise cells at G2/M. After 18 hours, cells were either further treated with anisomycin (100 µM) or the cells were released from inhibition into fresh media containing anisomycin (100 µM). Cells were harvested at the time points shown and Western blotting used to measure changes in APC5 protein levels in each sample.

To rule out any transcriptional effects for changes in APC5 levels, qRT-PCR was used to measure changes in APC5 transcript levels during mitosis. HeLa cells were synchronised in mitosis with nocodazole or taxol, harvested and the RNA isolated (as described in Materials and Methods, section 2.6). The RNA was reverse transcribed and a qPCR reaction performed in triplicate with the cDNA product using probes for APC5 and GAPDH as a control (Fig. 9).

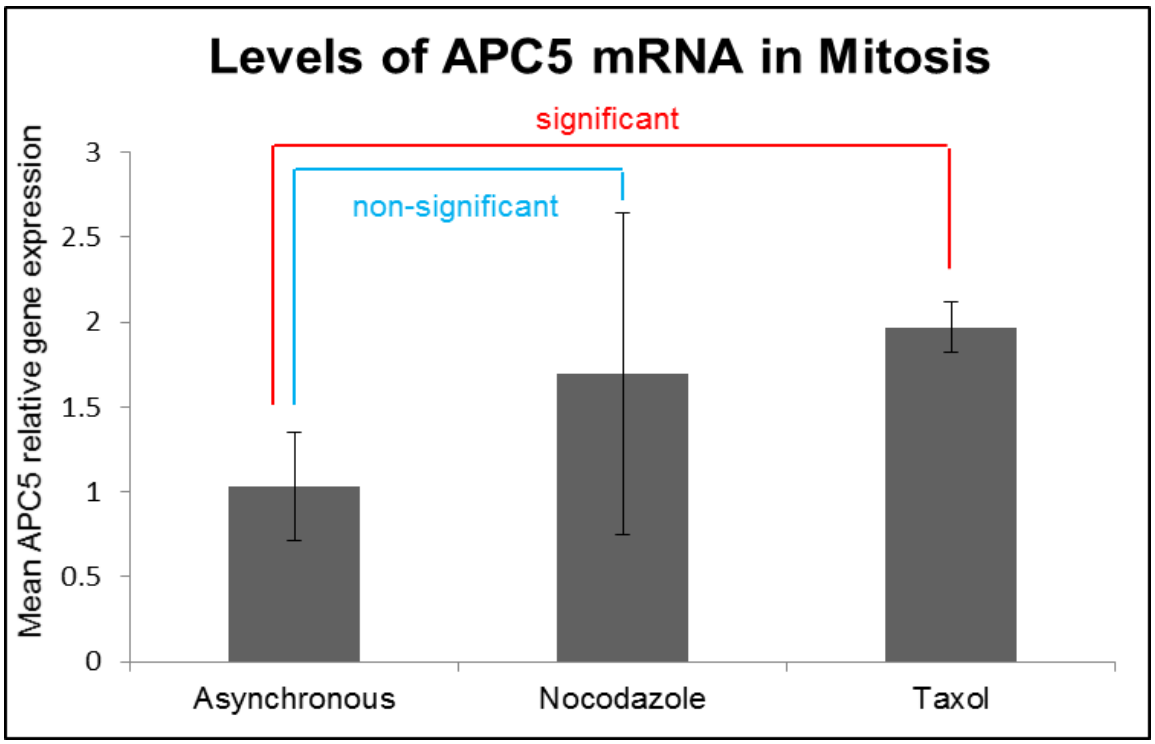


**Figure 9 – Changes in APC5 relative gene expression levels in mitotis**
HeLa cells were treated with nocodazole or taxol for 18 hours to synchronise cells in mitosis, harvested and the RNA isolated. RT-PCR was performed, followed by qPCR to analyse quantities of APC5 mRNA, relative to that of the housekeeping gene GAPDH. The experiment was repeated three times and the averages determined, with error bars calculated using the standard deviation. Statistical analysis revealed a significant difference between asynchronous and taxol-treated cells (significant at $p<0.05$).

The results for the taxol samples (although the RNA obtained in the third repeat was too dilute to be of use) showed a significant increase in the expression of the

APC5 gene in mitotic compared to asynchronous cells, with a T test score of 0.0224. These data support the hypothesis that the changes seen in APC5 occur at the level of protein stability, as opposed to changes in transcription levels. It is difficult to draw conclusions from the data for the nocodazole samples, as the high variance between the three repeats skewed the T test and suggested no significant change (0.349), however there does not appear to be a decrease in APC5 mRNA levels, again supporting the hypothesis. This experiment would need to be repeated to draw firm conclusions about levels of APC5 gene expression in mitosis.

### *3.4 FLAG-APC5 Protein Levels are Reduced in Mitosis*

Experiments so far have indicated that APC5 protein levels are reduced in mitosis. To validate these findings, a cell line was created that expressed FLAG-tagged APC5. HeLa Flp-In cells were transfected with a vector containing the sequence for FLAG-tagged APC5, which was integrated into the genome using the Flp recombinase enzyme. Expression of FLAG-APC5 was induced using Doxycyclin, while retaining expression of the endogenous APC5 protein. Expression of FLAG-APC5 was verified in three polyclonal strains by Western blotting following Doxycyclin treatment for 24 or 48 hours (Fig. 10). The results show all three clones express FLAG-APC5 and that 24 hours induction is sufficient. Both endogenous and FLAG-tagged APC5 can be seen with the APC5-specific antibody.

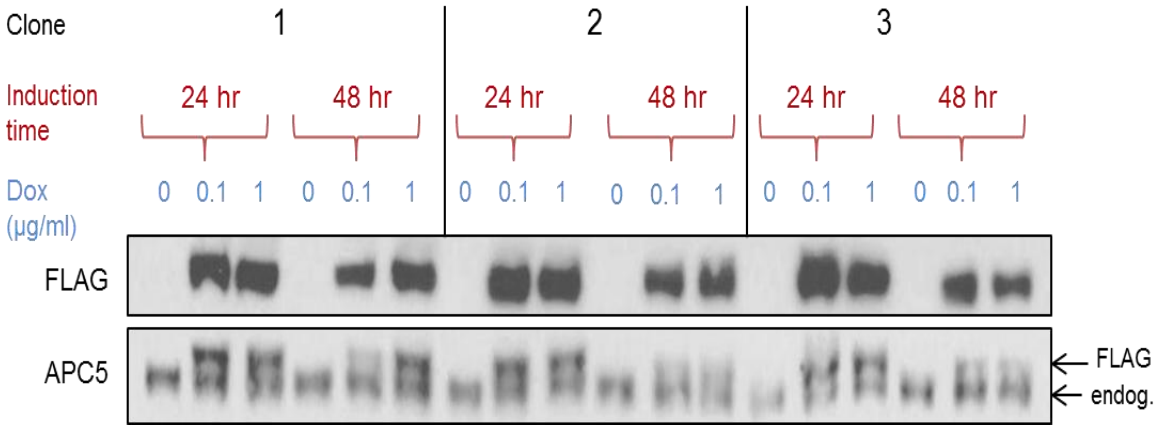


**Figure 10 – Expression of FLAG-tagged APC5 in transfected HeLa FRT cells**
Polyclonal HeLa FRT cells containing the gene encoding FLAG-tagged APC5 were generated and grown until confluent in blasticidin- and hygromycin-containing media. Doxycycline (Dox) was used at either 0.1 or 1 µg/ml to induce expression of the FLAG-APC5 in each population (1, 2 and 3). Cells were harvested after 24 and 48 hours, lysed and the protein concentration measured. Western blotting was used to monitor levels of FLAG-APC5 protein, along with endogenous APC5 (endog.).

Cells from each clone were treated with Doxycyclin for 24 hours, before addition of nocodazole or taxol to synchronise cells in mitosis. The cells were harvested and Western blotting used to investigate changes in the levels of FLAG-APC5 and endogenous APC/C subunits in mitosis (Fig. 11).

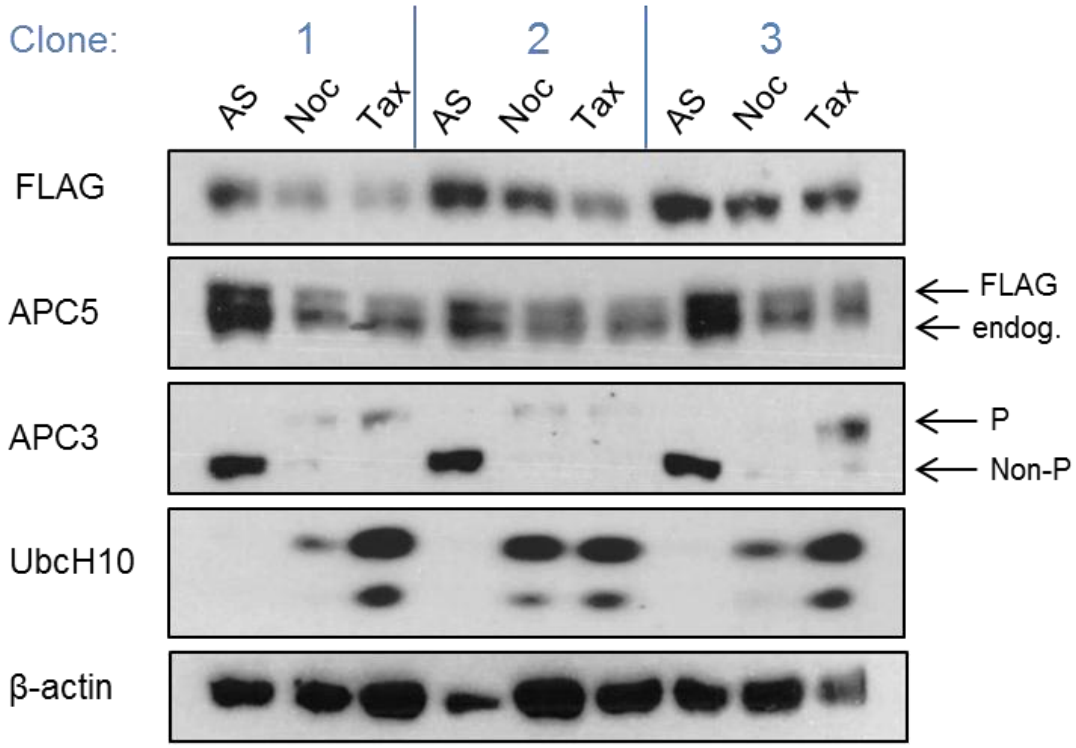


**Figure 11 – FLAG-APC5 levels decrease in mitosis**
Polyclonal HeLa FRT cells, containing the gene for FLAG-tagged APC5 were treated with 1 µg/ml doxycycline for 24 hours to induce FLAG-APC5 expression, before the addition of either nocodazole or taxol for 18 hours to arrest cells in mitosis. Mitotic cells were harvested by knock-off, lysed and the protein concentration measured. Western blotting was performed to analyse levels of FLAG-APC5 and endogenous APC5 in each condition compared to that in asynchronous (AS) cells. APC3 and UbcH10 were used to indicate mitotic arrest, with distinctive blots in mitosis vs. AS, while β-actin was included as a loading control.

The results show a decrease in FLAG-APC5 levels upon treatment with both nocodazole and taxol, similar to that seen for endogenous APC5. The decrease in FLAG-APC5 levels compared to asynchronous cells may be less than that observed for endogenous APC5 due to the continued transcription of FLAG-APC5 during mitosis. However, these results suggest that FLAG-APC5 protein levels are also reduced during mitosis.

The Western blots for APC3 and UbcH10 confirm that the cells are in mitotic arrest, with APC3 showing a mitotic phosphorylated form and UbcH10 levels increasing. However, APC3 shows lower levels than that normally seen and UbcH10 demonstrates a second band, perhaps a splice variant. These changes suggest that FLAG-APC5 could be having an effect on the APC/C and there may be further differences in these cells compared to HeLa cells.

Three monoclonal strains of FLAG-APC5-containing HeLa FRT cells were also generated and the expression of FLAG-APC5 verified (Fig. 12). Although these cell lines should be genetically identical, due to having the same point of genome integration, they may be useful for future studies in comparison to the polyclonal lines.

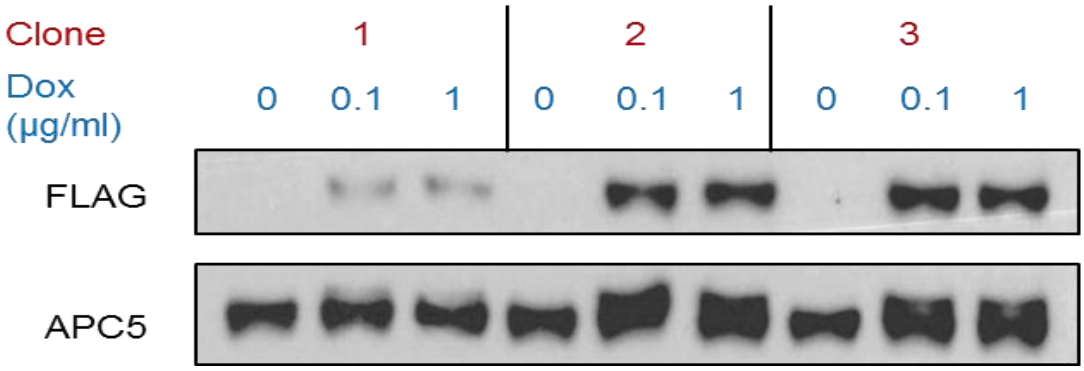


**Figure 12 – Expression of FLAG-tagged APC5 in transfected HeLa FRT monoclonal cells**
HeLa FRT cells were transfected with a plasmid containing the sequence for FLAG-tagged APC5, along with a Flp Recombinase target site, to allow genome integration. Cells were selected using blasticidin and hygromycin and individual cell colonies isolated and grown to confluence. The FLAG-APC5 gene was induced using doxycycline (Dox) at either 0.1 or 1 µg/ml and cells harvested after 24 hours, lysed and the protein concentration measured. Western blotting was used to monitor levels of FLAG-APC5 protein, along with endogenous APC5.

*3.5 Phosphorylation Status of APC5 in Mitosis*

This study has so far shown that, although APC5 protein levels are reduced during mitosis, a proportion of the protein remains. From this, one hypothesis is that different pools of APC5 are performing different functions in the cell, of which some are degraded in mitosis. It might be that APC5 has different post-translational modifications, thus distinguishing the proteins and marking them for degradation. As phosphorylation of APC/C subunits is known to be important in regulation, APC5 could be differentially phosphorylated. To investigate the phosphorylation status of APC5 in mitosis, MG132, a proteasome inhibitor, was used to enable analysis of the phosphorylation of the APC5 that is normally degraded in mitosis. Mass spectrometry was to be used to analyse the phosphorylation status of APC5 from mitotic cells treated with MG132, compared to those without MG132 treatment.

To confirm MG132 does indeed prevent APC5 degradation, cells were first synchronised with nocodazole or taxol for 18 hours, before addition of MG132. Western blotting was used to measure the levels of APC5 (Fig. 13a). However, although a slight increase in Nek2A was seen with MG132 in asynchronous and nocodazole/taxol-treated cells, there was little change in the levels of APC5 upon addition of MG132. This result may have been due to most of the APC5 already being degraded following nocodazole treatment, before the MG132 was added.

To investigate this possibility, nocodazole/taxol and MG132 were added simultaneously to HeLa cells and the procedure repeated (Fig. 13b). The results

showed MG132 treatment restored levels of both APC5 and Nek2A to asynchronous levels. Taken together, these data suggest that APC5 is targeted for degradation by the 26S proteasome in nocodazole/taxol-treated cells. However, the results for APC3 demonstrate a loss of its phosphorylation (Fig. 13b). Recent work in the laboratory has also found a decrease in protein phosphorylation levels by mass spectrometry (Minshall and Turnell, unpublished), suggesting that MG132 interferes with cellular phosphorylation status. Unfortunately, therefore, the experiment to investigate phosphorylation status could not be performed.

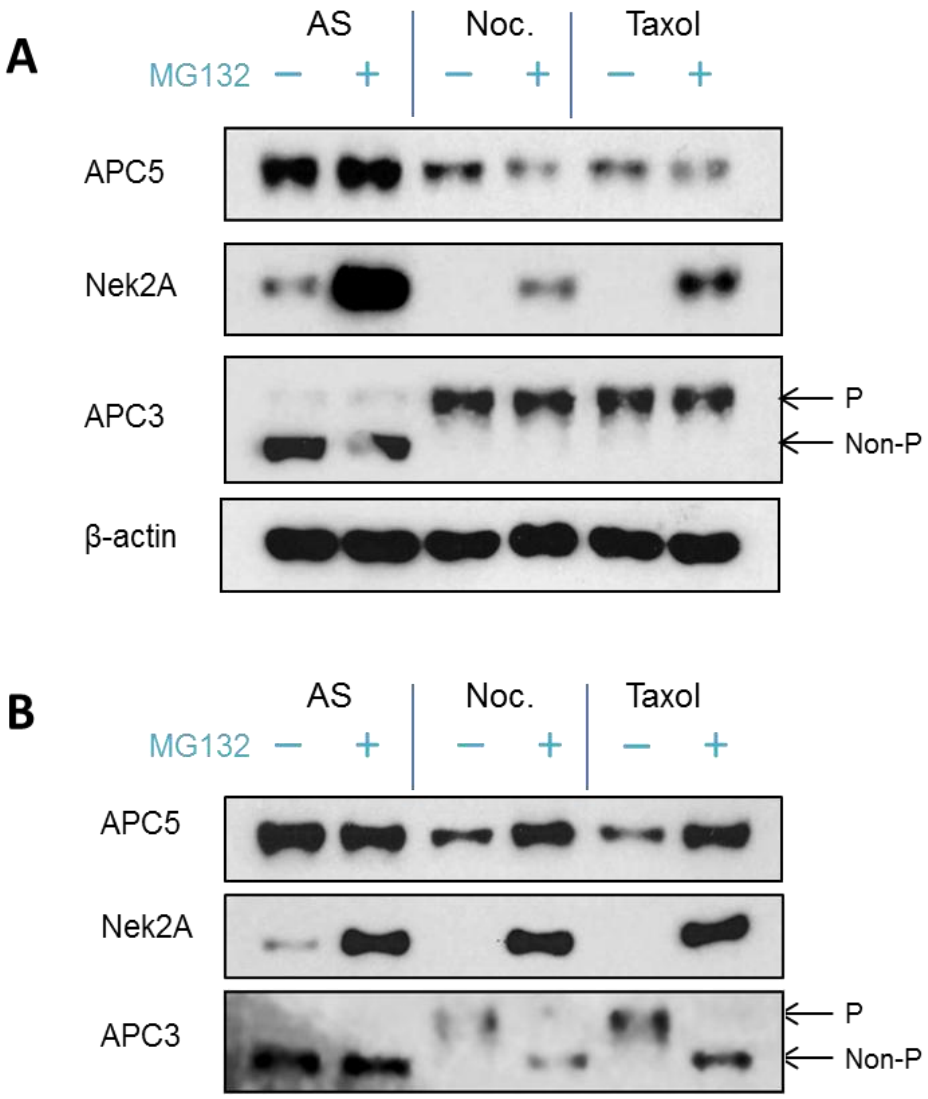


**Figure 13 – Changes in the levels of APC/C substrates and subunits following inhibition of the proteasome**

**(A)** HeLa cells were either untreated or subjected to treatment with nocodazole or taxol for 18 hours to induce mitotic arrest, before addition of the proteasome inhibitor MG132 to half of the cells. Cells were lysed and the relative levels of some APC/C subunits and substrates compared + or – 10 μM MG132, in mitotic and asynchronous cells, using Western blotting. β-actin was used as a loading control. **(B)** As for (A), except the nocodazole/taxol and MG132 were added simultaneously and the cells incubated overnight before harvesting. P – phosphorylated.

*3.6 APC5 Binds to Chromatin*

Previous studies have implicated APC5 in transcriptional regulation and chromatin structure. To further investigate the roles of APC5 outside the APC/C, HeLa cells were harvested, chromatin isolated and the levels of APC5 and APC/C subunits in each cellular fraction measured using Western blotting (Fig. 14).

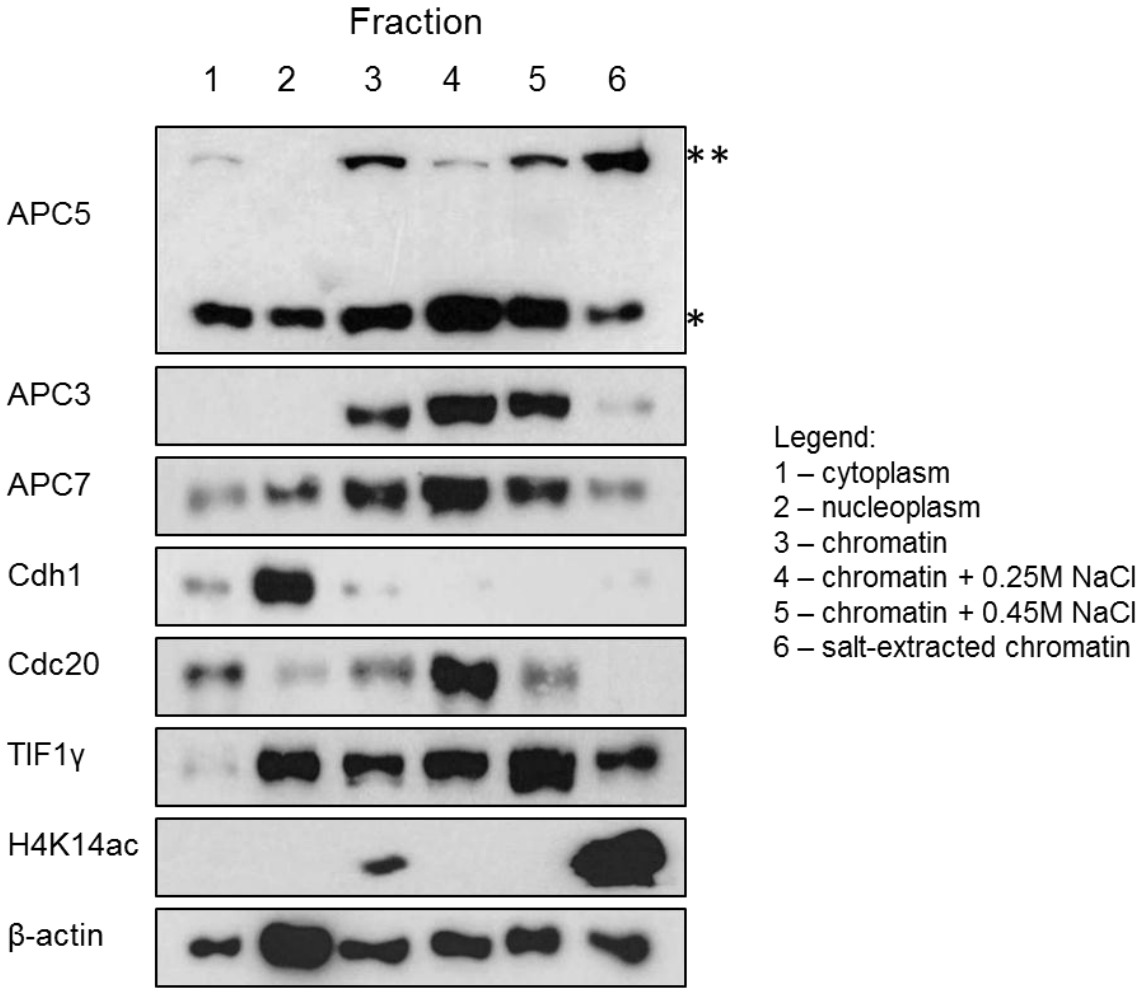


**Figure 14 – Levels of APC/C subunits in different cellular fractions**
HeLa cells were grown until confluent and harvested, before undergoing chromatin isolation. Samples were collected from each fraction and protein concentration measured. Western blotting was used to investigate the levels of APC/C subunits and co-activator proteins in each cellular fraction. TIF1γ was used as a control because it is known to bind chromatin, H4K14ac was used to confirm the presence of chromatin in the corresponding fractions and β-actin was used as a loading control. * - expected molecular weight band for APC5; ** - observed higher molecular weight band.

The results show that APC5 is found in all cellular fractions, including on the chromatin and can be eluted from the chromatin with the addition of salt. Interestingly, a second band for APC5 is present in the chromatin fractions indicating a higher molecular weight protein. This is likely to be either: non-specific antibody binding, a splice variant or post-translationally-modified APC5 (such as poly-ubiquitination, which could give such an increase in molecular weight). Furthermore, the APC/C subunits APC3 and APC7 are located mostly in the chromatin fractions (Fig. 14). A difference is seen between the locations of the two co-activators – Cdc20 is found in the chromatin, whereas there is almost no Cdh1, which is instead found in the nucleoplasm. This indicates that the function of the APC/C in chromatin is co-activator specific.

To investigate whether the higher molecular weight protein present in the APC5 blot was an APC5 species, the chromatin preparation procedure was repeated using HeLa Flp-In cells expressing FLAG-APC5 and Western blotting used to see if the band was present in the blots using the FLAG antibody (Fig. 15).

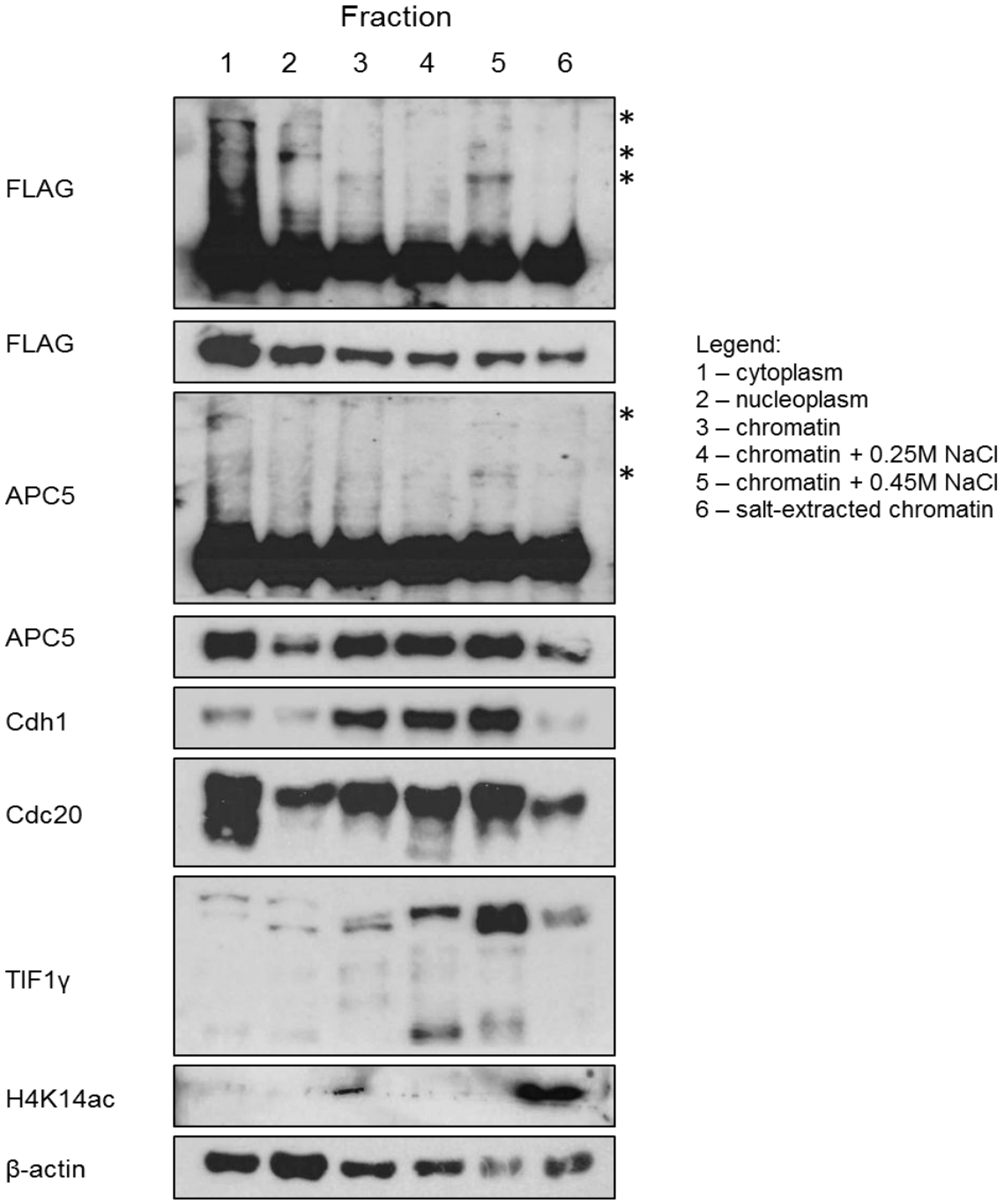


**Figure 15 – FLAG-APC5 is modified in chromatin**
HeLa Flip-In cells containing the FLAG-APC5 gene were grown in the presence of Doxycylin for 24 hours to induce expression before being harvested and undergoing a chromatin isolation procedure. Protein concentration from each cellular fraction was measured and a Western blot performed to investigate the levels of FLAG-APC5 and endogenous APC5, plus APC/C co-activator proteins, in each cellular fraction. TIF1γ was used as a control because it is known to bind chromatin, H4K14ac was used to confirm the presence of chromatin in the corresponding fractions and β-actin was used as a loading control. * - possible post-translational modifications.

The results do not show the distinct second band previously seen for APC5, but a number of higher molecular weight bands are seen in both the APC5 and FLAG-APC5 blots, indicating that APC5 and FLAG-APC5 are post-translationally modified in chromatin. Therefore, the band may be due to post-translational modifications on APC5, such as polyubiquitination, and the band is unlikely to be non-specific antibody binding. The difference seen between the two cell types might be because of the FLAG-tag disrupting normal APC/C function and APC5 modifications.

Moreover, there is also a change in the levels of the co-activators following FLAG-APC5 expression (Fig. 15). Cdh1, previously only found in the cytoplasm and nucleoplasm in HeLa, is now mostly located in the chromatin fractions of the FLAG-APC5-expressing Flp-In cells. Multiple bands of Cdc20 (as well as TIF1γ) can also be observed in the FLAG-APC5 cells. This suggests there could be inherent differences between the cells, making the findings difficult to compare. These results indicate, however, that the APC/C associates with chromatin.

### *3.7 Function of APC5 in Chromatin*

APC5 has previously been found to bind to chromatin (Harkness et al., 2005; Turnell et al., 2005; Turner et al., 2010) and results here confirmed the association. To further investigate the role of APC5 in chromatin, the binding partners of APC5 in chromatin were identified using IP-MS. HeLa cells were harvested and a chromatin preparation procedure carried out. APC5 IPs were completed using the nucleoplasm, solute from chromatin washed with 0.25 M

NaCl and salt-extracted chromatin resuspended in RIPA. Mass spectrometry was performed with the IP products and lists compiled of the proteins present, which were then analysed to account for non-specific binding, by comparison to a protein G-only control (Fig. 16). A large number of proteins were identified in the 0.25 M NaCl-washed chromatin sample, thus proteins particularly involved with gene expression were selected for analysis (Fig. 16b). A full list of the proteins identified can be found in the Appendix.

**A**

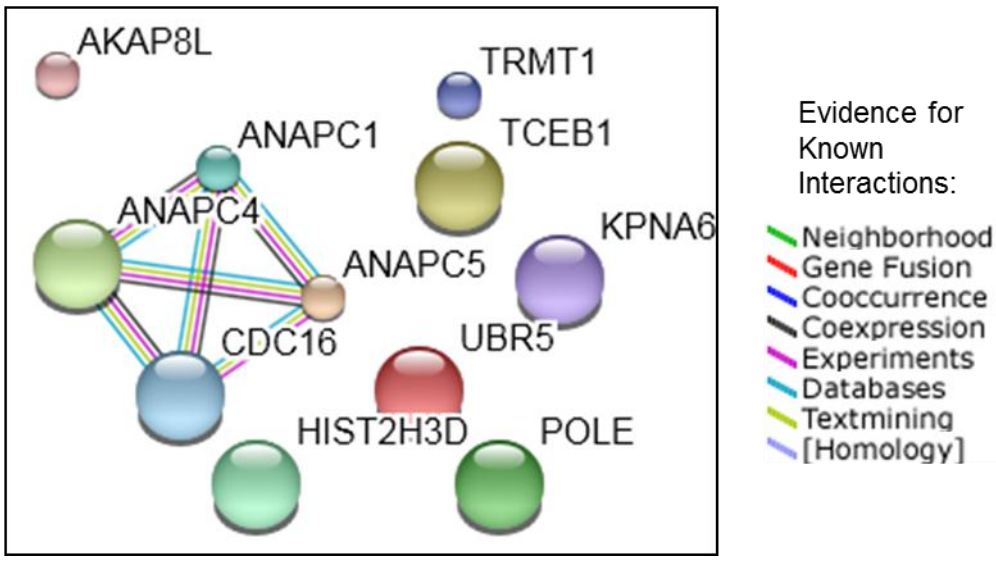

**B**

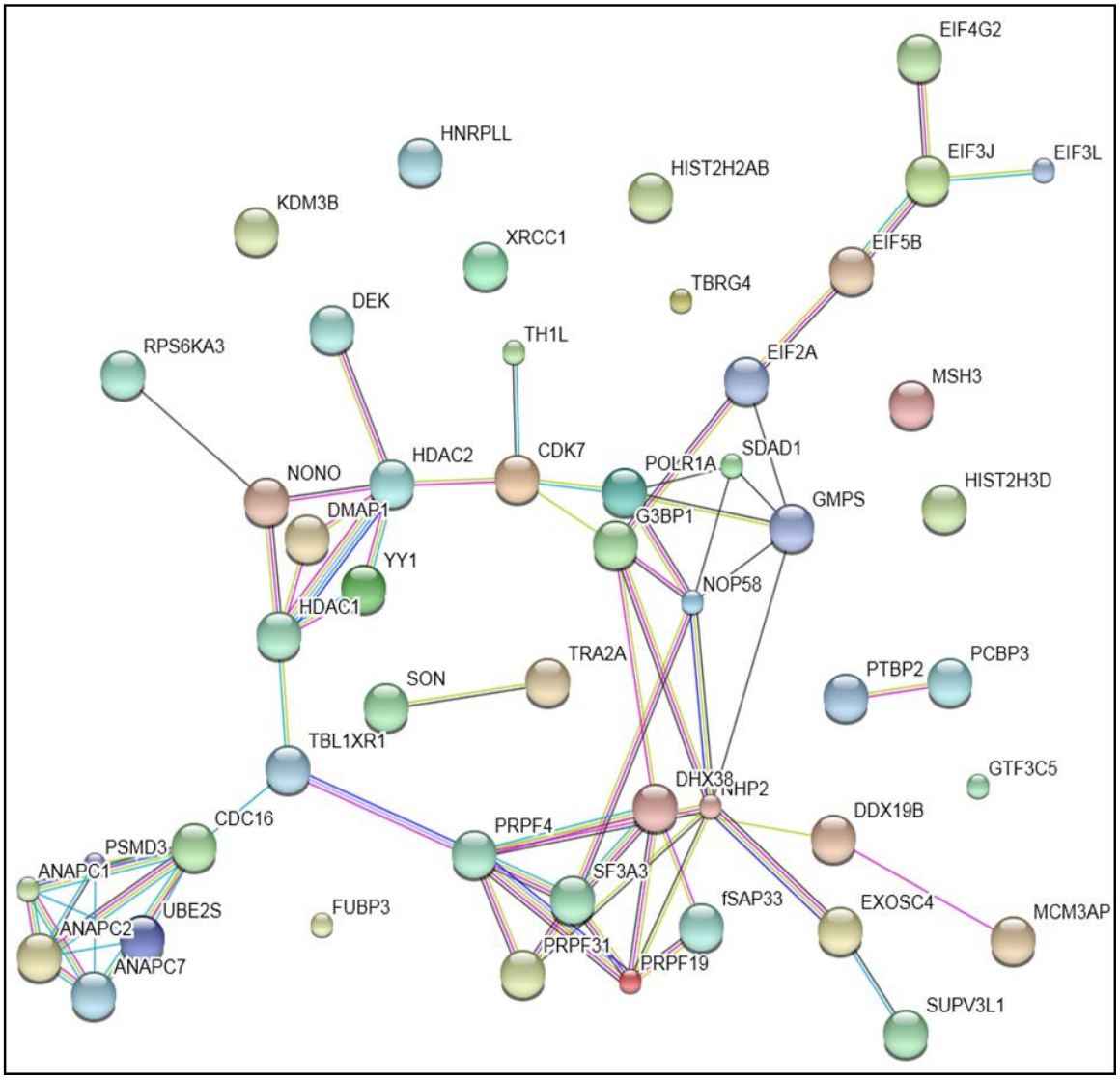


Evidence for Known Interactions:

- Neighborhood
- Gene Fusion
- Cooccurrence
- Coexpression
- Experiments
- Databases
- Textmining
- [Homology]

C

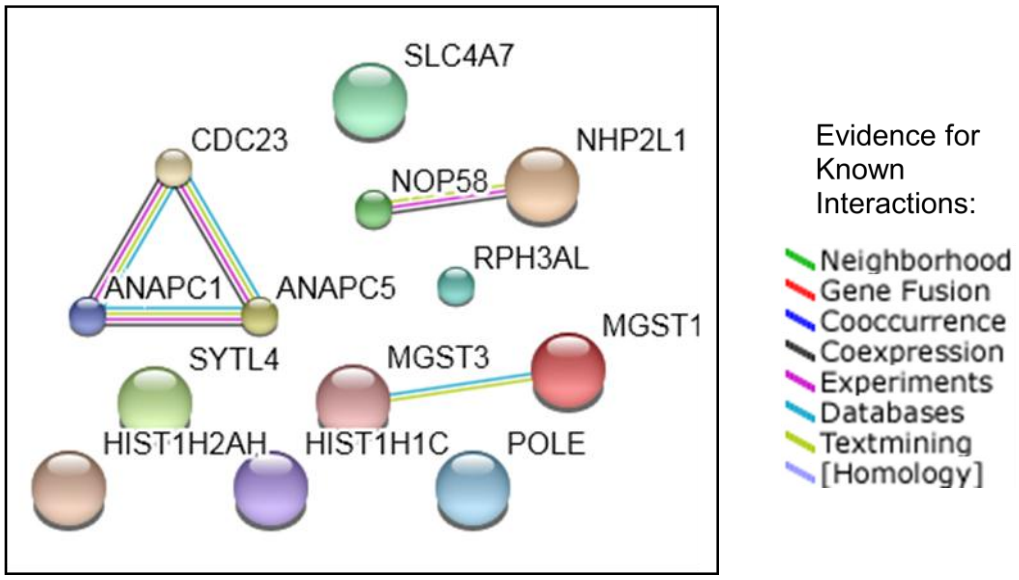


**Figure 16 – APC5 IP-MS reveals possible new functions for the APC/C in chromatin**

HeLa cells were grown until confluent, harvested and used in a chromatin preparation procedure. APC5 IP experiments were performed from three cell fractions: **(A)** nucleoplasm, **(B)** solute obtained from chromatin washed with 0.25M NaCl and **(C)** salt-extracted chromatin resuspended in RIPA buffer. Mass spectrometry was performed with the IP products. Fragmentation patterns were processed and compared to a protein database to identify the proteins present. Lists were compiled and analysed to account for non-specific binding, by comparison to a protein G- only control, and obvious contaminants were removed. A large number of proteins were identified in the 0.25M NaCl-washed chromatin sample (B), thus those proteins particularly involved with gene expression were selected for clarity. The lines between proteins indicate known interactions, with the different types of evidence colour-coded as indicated.
Diagrams were prepared using STRING 9.1 (**string**-db.org)

APC/C IPs from the nucleoplasmic fraction have been well studied and the results here provide a control for the method by confirming that APC/C subunits can be identified and that the APC5 IP was successful (Fig. 16a)

The results from the salt-washed chromatin sample revealed possible novel APC5 interactions with a range of proteins (Fig. 16b). These include proteins involved with transcriptional regulation, such as the histone modifiers HDAC1/2 and DMAP1, which mediate transcriptional repression, and a transcription factor called YY1, which acts on a variety of genes. NONO was also identified: a protein implicated in transcriptional regulation and splicing that has also been found to interact with HDAC1/2, showing a transcriptional regulation network that APC5 is potentially involved with. Furthermore, a number of proteins implicated in pre-mRNA processing were identified, including splicing factors such as SF3A3 and PRPF31 and an RNA helicase DHX38, plus an RNA exosome component (EXOSC4) and factors for mRNA export from the nucleus (DDX19B). Additionally, several proteins required for translation initiation were detected e.g. EIF2A, EIF3J. This suggests the APC/C could have additional functions in the cell.

Few results were obtained from the chromatin fraction (Fig. 16c), due to the difficulty of performing IPs for proteins within chromatin and the insolubility of chromatin. However, these data support roles for the APC/C in chromatin, such as in transcriptional regulation, and provide potential new areas for investigation to further understand the functions of APC/C in the cell.

# 4. DISCUSSION

Levels of the APC/C subunit, APC5, have been seen to change during mitosis, leading to the hypothesis that these changes are important in mitotic regulation. In this study, the use of nocodazole and taxol inhibitors to synchronise HeLa cells in mitosis has revealed a decrease in APC5 protein levels in mitosis (Fig. 7). This decrease in APC5 is controlled at the protein level by degradation, shown by prevention of the APC5 loss with the use of the proteasomal inhibitor MG132 (Fig. 13b) (as opposed to a reduction in gene expression, as suggested by qRT-PCR [Fig. 9]). However, the protein responsible for targeting APC5 for degradation is still unknown.

Experiments to determine the half-life of APC5 following release into mitosis revealed little change in APC5 levels over time (Fig. 8). One possible explanation of these data is that APC5 degradation is linked to the SAC. In nocodazole/taxol-treated cells, there is robust activation of the SAC as it is activated in each cell and at every kinetochore in the cell. In RO3306-released cells, however, there is a gradual activation of the SAC, both between cells and within each cell as each kinetochore attaches individually, mimicking normal progression. Thus, it may be that a robust SAC is required to observe the decrease in APC5 levels. APC5 could be targeted for degradation locally (at individual kinetochores) in order to promote the SAC and inhibit APC/C activity to prevent the cell's transition to anaphase until all chromosomes are aligned correctly on the spindle.

Consequently, the staggered APC5 degradation in the cell population means little variation is seen in the Western blot results.

It is possible that the APC/C self-regulates, supported by the presence of possible degrons in the APC5 primary sequence and that APC5 degradation is SAC-independent with levels following a similar pattern to that of known SAC-insensitive APC/C substrates such as Nek2A and cyclin A (Fig. 7). On the other hand, it could be targeted for degradation by other ubiquitin ligases, such as an SCF protein, for example β-TRCP which is known to be active in mitosis (Nakayama and Nakayama, 2005). To investigate these possibilities, APC/C inhibitors, such as proTAME, could be used to see if there are changes in APC5 levels in mitosis. The identified potential degrons could also be mutated to see if protein stability is affected.

In addition, the involvement of APC5 in the SAC could be further studied. This was hypothesised with the assumption that the cells were effectively synchronised and released. Figure 7 suggests that RO3306 brings about G2/M inhibition successfully, but further experiments are needed to verify that the cells here were indeed being released and progressing into mitosis. Therefore, the RO3306-release half-life experiments should be repeated and the progression into mitosis additionally verified by monitoring mitotic indicators such as phosphorylation of APC3 and degradation of cyclin B1. FACS analysis could also indicate effective inhibition of cells with RO3306 (at 4n), as well as release through mitosis. Secondly, real-time fluorescence microscopy, using fluorescently-labelled APC5

(such as previously used to study cyclin A degradation [den Elzen and Pines, 2001]), could be used to study both the timing of APC5 degradation during mitosis, providing more insight into function, and the involvement in the SAC by indicating any local degradation of APC5 near kinetochores.

However, not all of the APC5 present in cells is degraded in mitosis. Half-life experiments in nocodazole-treated cells indicated that the remaining protein is very stable (Fig. 8a). These data suggest that this pool of APC5 may be performing a distinct function, possibly distinguished by different post-translational modifications or subcellular location. One of the functions of APC5 aside from the APC/C is involved with chromatin structure and transcriptional regulation (Harkness et al., 2005; Turnell et al., 2005; Turner et al., 2010). Western blotting revealed APC5 bound to chromatin in HeLa cells, but also revealed a second higher molecular weight band in the chromatin fractions (Fig. 14), which could indicate either non-specific antibody binding, a splice variant or post-translational modification such as polyubiquitin, approximated from the increase in molecular weight.

Polyubiquitin has many roles in the cell beyond protein degradation, with various types of chains consisting of linkages through all seven lysines in its sequence, as well as the N-terminal methionine, and can be branched or non-branched (Kessler, 2013). This allows it to perform different functions e.g. K63 polyubiquitination plays a key role in cell signalling (NFκB activation) and DNA repair, while K11- or K48-linked chains target proteins for degradation (Kulathu and Komander, 2012;

Matsumoto et al., 2010). Therefore, it is plausible that polybiquitin is involved in APC5 function in chromatin. Alternatively, many TFs are destroyed by ubiquitin-mediated proteolysis, such as Myc. Both stable and unstable pools of Myc are present in cells (Tworkowski et al., 2002) and the region signalling ubiquitin-mediated proteolysis overlaps with the transcriptional activation region. A close correlation between the ability of the activation domain to activate transcription and to signal proteolysis has also been reported (Salghetti et al., 2000). Thus, polyubiquitination of APC5 and its degradation could be linked to its ability to act as a transcriptional activator.

The next step would be to perform a Western blot for ubiquitin on APC5 in chromatin to verify its presence. siRNA could also be used to knock down APC5 and see if the higher molecular weight band is still observed to rule out any non-specific antibody effects. Multiple bands were also seen for cells expressing FLAG-APC5 (Fig. 15), supporting post-translational modification. However, the bands were less distinct and blots for other proteins were also different, suggesting there could be innate differences between the cells or the FLAG-tag could be interfering with normal function. The next experiment would be to check that FLAG-APC5 is incorporated into the APC/C using IP-Western blotting (to detect interactions with APC/C subunits) and that it is still functional using in vitro activity assays (looking at ubiquitination of target substrates with purified APC/C components). This could be followed by a repeat of the Western blot to verify the results and also repeat using monoclonal HeLa FRT cells to look for any differences.

The function of APC5 in chromatin was further investigated using IP-MS (Fig. 16). It was found to interact with TFs and histone modifiers, consistent with previous findings of APC5 as a transcriptional regulator (Turnell et al., 2005) and suggesting some possible new gene targets. Some of the histone modifiers included HDAC1/2. Previous studies have found that some APC/C subunits are acetylated (Turnell laboratory, unpublished) and this may be associated with different times of the cell cycle or different activities. Thus, it may be hypothesised that the HDACs not only deacetylate histones, but can also act on the APC/C to regulate activity in different stages of the cell cycle. This could be further investigated by monitoring the association of APC/C subunits to HDAC1/2 in different stages of the cell cycle, using cell cycle inhibitors, by Western blotting. It is also consistent with past findings that the APC/C can modulate acetyltransferase activities in chromatin and can lead to altered histone acetylation patterns in yeast (Turnell et al. 2005; Turner et al., 2010). Moreover, the MS results suggest additional functions of the APC/C, perhaps in RNA processing and translation regulation, consistent with past studies that have reported interactions of APC5 with the poly(A) binding protein, which is bound to the internal ribosome entry site on mRNA, leading to repression of translation (Koloteva-Levine, et al., 2004). However, all interactions need to be first validated by IP-Western blotting.

Western blotting with various cellular fractions from HeLa cells also revealed an interesting pattern of co-activator localisation. A large proportion of Cdc20 was found bound to chromatin (eluting with 0.25 M NaCl), whereas very little Cdh1 was found in the chromatin fractions, with the majority present in the nucleoplasm (Fig.

14), suggesting that the chromatin functions of the APC/C could be co-activator specific. The APC/C has been reported to interact with p300/CBP to regulate transcription of a gene (Turnell et al., 2005). More recently, Cdc20 was discovered to modulate the transcriptional activity of the APC/C-CBP/p300 complex to positive regulate expression of *UBCH10* expression and was found bound to the promoter region (Nath et al., 2011). Therefore, this result is consistent with past findings. However, a different pattern of localisation of the two co-activators was seen when a polyclonal HeLa FRT cell line expressing FLAG-tagged APC5 was used (Fig. 15). The differences could be due to inherent differences between the cell lines (as multiple bands were seen for Cdc20 too) or the FLAG-tag could be interfering with normal APC/C regulation, for example tightly binding to Cdh1 and bringing it down to the chromatin. The experiments would need to be repeated with both cell lines and the monoclonal HeLa FRT cells, as well as possibly investigating differences compared to other cell lines, e.g. A549. Chromatin Immunoprecipitation could be used to verify co-activator binding to chromatin and reveal binding sites in the DNA to determine any possible gene targets.

It is possible that the different pools of APC5 are distinguished by different post-translational modifications, such as phosphorylation which is common in the APC/C. To study this, a proteasome inhibitor MG132 was used to enable analysis of the marks on normally degraded APC5 proteins. Although APC5 degradation was prevented, the phosphorylation status of the cell seemed to be affected (Fig. 13b) and so the experiment could not continue in the time available. The

procedure could be repeated using another proteasome inhibitor e.g. MG115, followed by MS to observe APC5 phosphorylation levels and determine the specific sites of phosphorylation.

In conclusion, this study has shown that APC5 is degraded during mitosis, in a SAC-insensitive manner, which may be involved in APC/C regulation and control of mitotic progression. APC5 has been found to bind to chromatin and possible new functions for the APC/C in chromatin identified. However, there are many more questions yet to answer, including identifying the protein responsible for targeting APC5 for degradation and investigating the role of post-translational modifications in determining the various functions of the APC/C in the cell.

# 5. REFERENCES


Barford, D. (2011). Structural insights into anaphase-promoting complex function and mechanism. *Philos.Trans.R.Soc.Lond.B.Biol.Sci., 366*(1584), 3605-3624.

Benanti, J. A. (2012). Coordination of cell growth and division by the ubiquitin–proteasome system. *Semin.Cell Dev.Biol., 23*(5), 492-498.

Braunstein, I., Miniowitz, S., Moshe, Y., & Hershko, A. (2007). Inhibitory factors associated with anaphase-promoting complex/cylosome in mitotic checkpoint. *Proc.Natl.Acad.Sci.U.S.A., 104*(12), 4870-4875.

Clijsters, L., Ogink, J., & Wolthuis, R. (2013). The spindle checkpoint, APC/CC(dc20), and APC/CC(dh1) play distinct roles in connecting mitosis to S phase. *J.Cell Biol., 201*(7), 1013-1026.

Clute, P., & Pines, J. (1999). Temporal and spatial control of cyclin B1 destruction in metaphase. *Nat.Cell Biol., 1*(2), 82-87.

Corn, P. G. (2007). Role of the ubiquitin proteasome system in renal cell carcinoma. *BMC Biochem., 8 Suppl 1*, S4.

Dehay, C., & Kennedy, H. (2007). Cell-cycle control and cortical development. *Nat.Rev.Neurosci., 8*(6), 438-450.

den Elzen, N., & Pines, J. (2001). Cyclin A is destroyed in prometaphase and can delay chromosome alignment and anaphase. *J.Cell Biol., 153*(1), 121-136.

Deshaies, R. J., & Joazeiro, C. A. (2009). RING domain E3 ubiquitin ligases. *Annu.Rev.Biochem., 78*, 399-434.

Di Fiore, B., & Pines, J. (2010). How cyclin A destruction escapes the spindle assembly checkpoint. *J.Cell Biol., 190*(4), 501-509.

Dimova, N. V., Hathaway, N. A., Lee, B. H., Kirkpatrick, D. S., Berkowitz, M. L., Gygi, S. P., et al. (2012). APC/C-mediated multiple monoubiquitylation provides an alternative degradation signal for cyclin B1. *Nat.Cell Biol., 14*(2), 168-176.

Fang, G., Yu, H., & Kirschner, M. W. (1998). Direct binding of CDC20 protein family members activates the anaphase-promoting complex in mitosis and G1. *Mol.Cell, 2*(2), 163-171.

Floyd, S., Pines, J., & Lindon, C. (2008). APC/CCdh1 targets aurora kinase to control reorganization of the mitotic spindle at anaphase.*18*(21), 1649-1658.

Fry, A. M. (2002). The Nek2 protein kinase: A novel regulator of centrosome structure. *Oncogene, 21*(40), 6184-6194.

Funabiki, H., Yamano, H., Kumada, K., Nagao, K., Hunt, T., & Yanagida, M. (1996). Cut2 proteolysis required for sister-chromatid seperation in fission yeast. *Nature, 381*(6581), 438-441.

Garnett, M. J., Mansfeld, J., Godwin, C., Matsusaka, T., Wu, J., Russell, P., et al. (2009). UBE2S elongates ubiquitin chains on APC/C substrates to promote mitotic exit. *Nat.Cell Biol., 11*(11), 1363-1369.

Glotzer, M., Murray, A. W., & Kirschner, M. W. (1991). Cyclin is degraded by the ubiquitin pathway. *Nature, 349*(6305), 132-138.

Gorr, I. H., Boos, D., & Stemmann, O. (2005). Mutual inhibition of separase and Cdk1 by two-step complex formation. *Mol.Cell, 19*(1), 135-141.

Hames, R. S., Wattam, S. L., Yamano, H., Bacchieri, R., & Fry, A. M. (2001). APC/C-mediated destruction of the centrosomal kinase Nek2A occurs in early mitosis and depends upon a cyclin A-type D-box. *Embo j., 20*(24), 7117-7127.

Harkness, T. A., Arnason, T. G., Legrand, C., Pisclevich, M. G., Davies, G. F., & Turner, E. L. (2005). Contribution of CAF-I to anaphase-promoting-complex-mediated mitotic chromatin assembly in saccharomyces cerevisiae. *Eukaryot.Cell., 4*(4), 673-684.

Hayes, M. J., Kimata, Y., Wattam, S. L., Lindon, C., Mao, G., Yamano, H., et al. (2006). Early mitotic degradation of Nek2A depends on Cdc20-independent interaction with the APC/C. *Nat.Cell Biol., 8*(6), 607-614.

Hershko, A., & Ciechanover, A. (1998). The ubiquitin system. *Annu.Rev.Biochem., 67*, 425-479.

Izawa, D., & Pines, J. (2011). How APC/C-Cdc20 changes its substrate specificity in mitosis. *Nat.Cell Biol., 13*(3), 223-233.

Kessler, B. M. (2013). Ubiquitin - omics reveals novel networks and associations with human disease. *Curr.Opin.Chem.Biol., 17*(1), 59-65.

Kirkpatrick, D. S., Hathaway, N. A., Hanna, J., Elsasser, S., Rush, J., Finley, D., et al. (2006). Quantitative analysis of in vitro ubiquitinated cyclin B1 reveals complex chain topology. *Nat.Cell Biol., 8*(7), 700-710.

Koloteva-Levine, N., Pinchasi, D., Pereman, I., Zur, A., Brandeis, M., & Elroy-Stein, O. (2004). The Apc5 subunit of the anaphase-promoting complex/cyclosome interacts with poly(A) binding protein and represses internal ribosome entry site-mediated translation. *Mol.Cell.Biol., 24*(9), 3577-3587.

Kramer, E. R., Gieffers, C., Holzl, G., Hengstschlager, M., & Peters, J. M. (1998). Activation of the human anaphase-promoting complex by proteins of the CDC20/Fizzy family. *Curr.Biol., 8*(22), 1207-1210.

Kulathu, Y., & Komander, D. (2012). Atypical ubiquitylation - the unexplored world of polyubiquitin beyond Lys48 and Lys63 linkages. *Nat.Rev.Mol.Cell Biol., 13*(8), 508-523.

Lim, S., & Kaldis, P. (2013). Cdks, cyclins and CKIs: Roles beyond cell cycle regulation. *Development, 140*(15), 3079-3093.

Matsumoto, M. L., Wickliffe, K. E., Dong, K. C., Yu, C., Bosanac, I., Bustos, D., et al. (2010). K11-linked polyubiquitination in cell cycle control revealed by a K11 linkage-specific antibody. *Mol.Cell, 39*(3), 477-484.

Meyer, H., & Rape, M. (2011). Processive ubiquitin chain formation by the anaphase-promoting complex. *Semin.Cell Dev.Biol., 22*(6), 544-550.

Nakayama, K. I., & Nakayama, K. (2005). Regulation of the cell cycle by SCF-type ubiquitin ligases. *Semin.Cell Dev.Biol., 16*(3), 323-333.

Nath, S., Banerjee, T., Sen, D., Das, T., & Roychoudhury, S. (2011). Spindle assembly checkpoint protein Cdc20 transcriptionally activates expression of ubiquitin carrier protein UbcH10. *J.Biol.Chem., 286*(18), 15666-15677.

Pagano, M., Pepperkok, R., Verde, F., Ansorge, W., & Draetta, G. (1992). Cyclin A is required at two points in the human cell cycle. *Embo j., 11*(3), 961-971.

Pfleger, C. M., & Kirschner, M. W. (2000). The KEN box: An APC recognition signal distinct from the D box targeted by Cdh1. *Genes Dev., 14*(6), 655-665.

Pfleger, C. M., Lee, E., & Kirschner, M. W. (2001). Substrate recognition by the Cdc20 and Cdh1 components of the anaphase-promoting complex. *Genes Dev., 15*(18), 2396-2407.

Primorac, I., & Musacchio, A. (2013). Panta rhei: The APC/C at steady state. *J.Cell Biol., 201*(2), 177-189.

Rudner, A. D., & Murray, A. W. (2000). Phosphorylation by Cdc28 activates the Cdc20-dependent activity of the anaphase-promoting complex. *J.Cell Biol., 149*(7), 1377-1390.

Schreiber, A., Stengel, F., Zhang, Z., Enchev, R. I., Kong, E. H., Morris, E. P., et al. (2011). Structural basis for the subunit assembly of the anaphase-promoting complex. *Nature, 470*(7333), 227-232.

Steen, J. A., Steen, H., Georgi, A., Parker, K., Springer, M., Kirchner, M., et al. (2008). Different phosphorylation states of the anaphase promoting complex in response to antimitotic drugs: A quantitative proteomic analysis. *Proc.Natl.Acad.Sci.U.S.A., 105*(16), 6069-6074.

Stemmann, O., Zou, H., Gerber, S. A., Gygi, S. P., & Kirschner, M. W. (2001). Dual inhibition of sister chromatid separation at metaphase. *Cell, 107*(6), 715-726.

*String 9.1.* Retrieved January, 2014, from http://string-db.org/

Sudakin, V., Ganoth, D., Dahan, A., Heller, H., Hershko, J., Luca, F. C., et al. (1995). The cyclosome, a large complex containing cyclin-selective ubiquitin ligase activity, targets cyclins for destruction at the end of mitosis. *Mol.Biol.Cell, 6*(2), 185-197.

Sudo, T., Ota, Y., Kotani, S., Nakao, M., Takami, Y., Takeda, S., et al. (2001). Activation of Cdh1-dependent APC is required for G1 cell cycle arrest and DNA damage-induced G2 checkpoint in vertebrate cells. *Embo j., 20*(22), 6499-6508. doi:10.1093/emboj/20.22.6499

Tang, Z., Li, B., Bharadwaj, R., Zhu, H., Ozkan, E., Hakala, K., et al. (2001). APC2 cullin protein and APC11 RING protein comprise the minimal ubiquitin ligase module of the anaphase-promoting complex. *Mol.Biol.Cell, 12*(12), 3839-3851.

Turnell, A. S., Stewart, G. S., Grand, R. J., Rookes, S. M., Martin, A., Yamano, H., et al. (2005). The APC/C and CBP/p300 cooperate to regulate transcription and cell-cycle progression. *Nature, 438*(7068), 690-695.

Turner, E. L., Malo, M. E., Pisclevich, M. G., Dash, M. D., Davies, G. F., Arnason, T. G., et al. (2010). The saccharomyces cerevisiae anaphase-promoting complex interacts with multiple histone-modifying enzymes to regulate cell cycle progression. *Eukaryot.Cell., 9*(10), 1418-1431.

van Zon, W., & Wolthuis, R. M. (2010). Cyclin A and Nek2A: APC/C-Cdc20 substrates invisible to the mitotic spindle checkpoint. *Biochem.Soc.Trans., 38*(Pt 1), 72-77.

Wendt, K. S., Vodermaier, H. C., Jacob, U., Gieffers, C., Gmachl, M., Peters, J. M., et al. (2001). Crystal structure of the APC10/DOC1 subunit of the human anaphase-promoting complex. *Nat.Struct.Biol., 8*(9), 784-788.

Williams, G. H., & Stoeber, K. (2012). The cell cycle and cancer. *J.Pathol., 226*(2), 352-364.

Wysocka, J., Reilly, P. T., & Herr, W. (2001). Loss of HCF-1-chromatin association precedes temperature-induced growth arrest of tsBN67 cells. *Mol.Cell.Biol., 21*(11), 3820-3829.

Zhang, Z., Roe, S. M., Diogon, M., Kong, E., El Alaoui, H., & Barford, D. (2010). Molecular structure of the N-terminal domain of the APC/C subunit Cdc27 reveals a homo-dimeric tetratricopeptide repeat architecture. *J.Mol.Biol., 397*(5), 1316-1328.

Zur, A., & Brandeis, M. (2001). Securin degradation is mediated by fzy and fzr, and is required for complete chromatid separation but not for cytokinesis. *Embo j., 20*(4), 792-801.

Zur, A., & Brandeis, M. (2002). Timing of APC/C substrate degradation is determined by fzy/fzr specificity of destruction boxes. *Embo j., 21*(17), 4500-4510.

# 6. APPENDIX – APC5 IP-MS Data

HeLa cells were grown until confluent, harvested and used in a chromatin preparation procedure. APC5 IP experiments were performed from three cell fractions: nucleoplasm, solute from 0.25M NaCl-washed chromatin and salt-extracted chromatin resuspended in RIPA buffer. In-gel tryptic digest was performed on the IP products, before running on a mass spectrometer. Fragmentation patterns were processed and compared to a protein database to identify the proteins present. Lists were compiled and analysed to account for non-specific binding, by comparison to a protein G- only control, and obvious contaminants were removed. Full protein lists obtained for each fraction are shown below.

## *6.1 Nucleoplasm*

| Accession | Protein | Scores | #Peptides |
|---|---|---|---|
| APC1_HUMAN | Anaphase-promoting complex subunit 1 OS=Homo sapiens GN=ANAPC1 PE=1 SV=1 | 638.8 (M:638.8) | 17 |
| CDC16_HUMAN | Cell division cycle protein 16 homolog OS=Homo sapiens GN=CDC16 PE=1 SV=2 | 222.4 (M:222.4) | 4 |
| UBR5_HUMAN | E3 ubiquitin-protein ligase UBR5 OS=Homo sapiens GN=UBR5 PE=1 SV=2 | 151.2 (M:151.2) | 3 |
| H32_HUMAN | Histone H3.2 OS=Homo sapiens GN=HIST2H3A PE=1 SV=3 | 150.5 (M:150.5) | 4 |
| APC4_HUMAN | Anaphase-promoting complex subunit 4 OS=Homo sapiens GN=ANAPC4 PE=1 SV=2 | 147.4 (M:147.4) | 4 |
| AKP8L_HUMAN | A-kinase anchor protein 8-like OS=Homo sapiens GN=AKAP8L PE=1 SV=2 | 63.5 (M:63.5) | 1 |
| TRM1_HUMAN | N(2),N(2)-dimethylguanosine tRNA methyltransferase OS=Homo sapiens GN=TRMT1 PE=1 SV=1 | 52.9 (M:52.9) | 2 |
| APC5_HUMAN | Anaphase-promoting complex subunit 5 OS=Homo sapiens GN=ANAPC5 PE=1 SV=2 | 42.2 (M:42.2) | 1 |
| IMA7_HUMAN | Importin subunit alpha-7 OS=Homo sapiens GN=KPNA6 PE=1 SV=1 | 39.3 (M:39.3) | 1 |
| DPOE1_HUMAN | DNA polymerase epsilon catalytic subunit A OS=Homo sapiens GN=POLE PE=1 SV=5 | 31.9 (M:31.9) | 1 |
| ELOC_HUMAN | Transcription elongation factor B polypeptide 1 OS=Homo sapiens GN=TCEB1 PE=1 SV=1 | 31.2 (M:31.2) | 1 |

*6.2 Chromatin + 0.25 M NaCl*

| Accession | Protein | Scores | #Peptides |
|---|---|---|---|
| NONO_HUMAN | Non-POU domain-containing octamer-binding protein OS=Homo sapiens GN=NONO PE=1 SV=4 | 1197.2 (M:1197.2) | 23 |
| HNRLL_HUMAN | Heterogeneous nuclear ribonucleoprotein L-like OS=Homo sapiens GN=HNRPLL PE=1 SV=1 | 710.3 (M:710.3) | 13 |
| API5_HUMAN | Apoptosis inhibitor 5 OS=Homo sapiens GN=API5 PE=1 SV=2 | 584.1 (M:584.1) | 14 |
| TCPH_HUMAN | T-complex protein 1 subunit eta OS=Homo sapiens GN=CCT7 PE=1 SV=2 | 549.4 (M:549.4) | 12 |
| HDAC1_HUMAN | Histone deacetylase 1 OS=Homo sapiens GN=HDAC1 PE=1 SV=1 | 528.8 (M:528.8) | 11 |
| G3BP1_HUMAN | Ras GTPase-activating protein-binding protein 1 OS=Homo sapiens GN=G3BP1 PE=1 SV=1 | 519.0 (M:519.0) | 10 |
| PCBP3_HUMAN | Poly(rC)-binding protein 3 OS=Homo sapiens GN=PCBP3 PE=1 SV=1 | 426.4 (M:426.4) | 7 |
| EHD2_HUMAN | EH domain-containing protein 2 OS=Homo sapiens GN=EHD2 PE=1 SV=2 | 414.5 (M:414.5) | 9 |
| EIF3L_HUMAN | Eukaryotic translation initiation factor 3 subunit L OS=Homo sapiens GN=EIF3L PE=1 SV=1 | 405.4 (M:405.4) | 6 |
| HDAC2_HUMAN | Histone deacetylase 2 OS=Homo sapiens GN=HDAC2 PE=1 SV=2 | 398.7 (M:398.7) | 9 |
| TCPZ_HUMAN | T-complex protein 1 subunit zeta OS=Homo sapiens GN=CCT6A PE=1 SV=3 | 388.0 (M:388.0) | 8 |
| TCPB_HUMAN | T-complex protein 1 subunit beta OS=Homo sapiens GN=CCT2 PE=1 SV=4 | 276.0 (M:276.0) | 6 |
| GNAI3_HUMAN | Guanine nucleotide-binding protein G(k) subunit alpha OS=Homo sapiens GN=GNAI3 PE=1 SV=3 | 267.9 (M:267.9) | 5 |
| NELFD_HUMAN | Negative elongation factor C/D OS=Homo sapiens GN=TH1L PE=1 SV=2 | 260.0 (M:260.0) | 6 |
| FUBP3_HUMAN | Far upstream element-binding protein 3 OS=Homo sapiens GN=FUBP3 PE=1 SV=2 | 258.6 (M:258.6) | 5 |
| SHOC2_HUMAN | Leucine-rich repeat protein SHOC-2 OS=Homo sapiens GN=SHOC2 PE=1 SV=2 | 224.1 (M:224.1) | 4 |
| PTBP2_HUMAN | Polypyrimidine tract-binding protein 2 OS=Homo sapiens GN=PTBP2 PE=1 SV=1 | 222.6 (M:222.6) | 7 |

| | | | |
|---|---|---|---|
| H32_HUMAN | Histone H3.2 OS=Homo sapiens GN=HIST2H3A PE=1 SV=3 | 222.0 (M:222.0) | 6 |
| APC7_HUMAN | Anaphase-promoting complex subunit 7 OS=Homo sapiens GN=ANAPC7 PE=1 SV=3 | 222.0 (M:222.0) | 5 |
| NOP58_HUMAN | Nucleolar protein 58 OS=Homo sapiens GN=NOP58 PE=1 SV=1 | 212.8 (M:212.8) | 5 |
| GBB1_HUMAN | Guanine nucleotide-binding protein G(I)/G(S)/G(T) subunit beta-1 OS=Homo sapiens GN=GNB1 PE=1 SV=3 | 207.4 (M:207.4) | 4 |
| SEC13_HUMAN | Protein SEC13 homolog OS=Homo sapiens GN=SEC13 PE=1 SV=3 | 197.2 (M:197.2) | 3 |
| SNX27_HUMAN | Sorting nexin-27 OS=Homo sapiens GN=SNX27 PE=1 SV=2 | 194.3 (M:194.3) | 3 |
| RPA1_HUMAN | DNA-directed RNA polymerase I subunit RPA1 OS=Homo sapiens GN=POLR1A PE=1 SV=2 | 176.2 (M:176.2) | 5 |
| RS10L_HUMAN | Putative 40S ribosomal protein S10-like OS=Homo sapiens GN=RPS10P5 PE=5 SV=1 | 172.6 (M:172.6) | 3 |
| PSMD3_HUMAN | 26S proteasome non-ATPase regulatory subunit 3 OS=Homo sapiens GN=PSMD3 PE=1 SV=2 | 171.3 (M:171.3) | 4 |
| SON_HUMAN | Protein SON OS=Homo sapiens GN=SON PE=1 SV=3 | 168.9 (M:168.9) | 4 |
| SF3A3_HUMAN | Splicing factor 3A subunit 3 OS=Homo sapiens GN=SF3A3 PE=1 SV=1 | 167.6 (M:167.6) | 6 |
| SUV3_HUMAN | ATP-dependent RNA helicase SUPV3L1, mitochondrial OS=Homo sapiens GN=SUPV3L1 PE=1 SV=1 | 166.9 (M:166.9) | 4 |
| PP1B_HUMAN | Serine/threonine-protein phosphatase PP1-beta catalytic subunit OS=Homo sapiens GN=PPP1CB PE=1 SV=3 | 160.1 (M:160.1) | 4 |
| RALY_HUMAN | RNA-binding protein Raly OS=Homo sapiens GN=RALY PE=1 SV=1 | 158.7 (M:158.7) | 4 |
| PRP31_HUMAN | U4/U6 small nuclear ribonucleoprotein Prp31 OS=Homo sapiens GN=PRPF31 PE=1 SV=2 | 153.5 (M:153.5) | 3 |
| PP1G_HUMAN | Serine/threonine-protein phosphatase PP1-gamma catalytic subunit OS=Homo sapiens GN=PPP1CC PE=1 SV=1 | 150.5 (M:150.5) | 4 |
| EHD4_HUMAN | EH domain-containing protein 4 OS=Homo sapiens GN=EHD4 PE=1 SV=1 | 149.5 (M:149.5) | 3 |
| KDM3B_HUMAN | Lysine-specific demethylase 3B OS=Homo sapiens GN=KDM3B PE=1 SV=1 | 149.5 (M:149.5) | 3 |
| DD19B_HUMAN | ATP-dependent RNA helicase DDX19B OS=Homo sapiens GN=DDX19B PE=1 SV=1 | 146.8 (M:146.8) | 3 |
| IMA7_HUMAN | Importin subunit alpha-7 OS=Homo sapiens GN=KPNA6 PE=1 SV=1 | 140.6 (M:140.6) | 3 |

| | | | |
|---|---|---|---|
| PRP16_HUMAN | Pre-mRNA-splicing factor ATP-dependent RNA helicase PRP16 OS=Homo sapiens GN=DHX38 PE=1 SV=2 | 137.6 (M:137.6) | 5 |
| MAP7_HUMAN | Ensconsin OS=Homo sapiens GN=MAP7 PE=1 SV=1 | 133.2 (M:133.2) | 2 |
| PERQ2_HUMAN | PERQ amino acid-rich with GYF domain-containing protein 2 OS=Homo sapiens GN=GIGYF2 PE=1 SV=1 | 132.7 (M:132.7) | 3 |
| NUP62_HUMAN | Nuclear pore glycoprotein p62 OS=Homo sapiens GN=NUP62 PE=1 SV=3 | 132.4 (M:132.4) | 2 |
| PP1A_HUMAN | Serine/threonine-protein phosphatase PP1-alpha catalytic subunit OS=Homo sapiens GN=PPP1CA PE=1 SV=1 | 132.2 (M:132.2) | 4 |
| SYYC_HUMAN | Tyrosyl-tRNA synthetase, cytoplasmic OS=Homo sapiens GN=YARS PE=1 SV=4 | 130.8 (M:130.8) | 3 |
| CYFP1_HUMAN | Cytoplasmic FMR1-interacting protein 1 OS=Homo sapiens GN=CYFIP1 PE=1 SV=1 | 129.9 (M:129.9) | 4 |
| CKAP4_HUMAN | Cytoskeleton-associated protein 4 OS=Homo sapiens GN=CKAP4 PE=1 SV=2 | 128.0 (M:128.0) | 2 |
| DDX6_HUMAN | Probable ATP-dependent RNA helicase DDX6 OS=Homo sapiens GN=DDX6 PE=1 SV=2 | 125.9 (M:125.9) | 2 |
| MSH3_HUMAN | DNA mismatch repair protein Msh3 OS=Homo sapiens GN=MSH3 PE=1 SV=3 | 124.6 (M:124.6) | 3 |
| IMA2_HUMAN | Importin subunit alpha-2 OS=Homo sapiens GN=KPNA2 PE=1 SV=1 | 124.0 (M:124.0) | 1 |
| NHP2_HUMAN | H/ACA ribonucleoprotein complex subunit 2 OS=Homo sapiens GN=NHP2 PE=1 SV=1 | 119.0 (M:119.0) | 2 |
| IF2P_HUMAN | Eukaryotic translation initiation factor 5B OS=Homo sapiens GN=EIF5B PE=1 SV=4 | 118.5 (M:118.5) | 2 |
| ABCD3_HUMAN | ATP-binding cassette sub-family D member 3 OS=Homo sapiens GN=ABCD3 PE=1 SV=1 | 118.3 (M:118.3) | 3 |
| TBRG4_HUMAN | Protein TBRG4 OS=Homo sapiens GN=TBRG4 PE=1 SV=1 | 115.2 (M:115.2) | 4 |
| IF4G2_HUMAN | Eukaryotic translation initiation factor 4 gamma 2 OS=Homo sapiens GN=EIF4G2 PE=1 SV=1 | 113.5 (M:113.5) | 4 |
| EIF2A_HUMAN | Eukaryotic translation initiation factor 2A OS=Homo sapiens GN=EIF2A PE=1 SV=3 | 113.1 (M:113.1) | 2 |
| DDX56_HUMAN | Probable ATP-dependent RNA helicase DDX56 OS=Homo sapiens GN=DDX56 PE=1 SV=1 | 112.0 (M:112.0) | 2 |

| | | | |
|---|---|---|---|
| AMPM2_HUMAN | Methionine aminopeptidase 2 OS=Homo sapiens GN=METAP2 PE=1 SV=1 | 107.0 (M:107.0) | 3 |
| CPNE3_HUMAN | Copine-3 OS=Homo sapiens GN=CPNE3 PE=1 SV=1 | 106.5 (M:106.5) | 2 |
| TYY1_HUMAN | Transcriptional repressor protein YY1 OS=Homo sapiens GN=YY1 PE=1 SV=2 | 98.5 (M:98.5) | 2 |
| ELMO2_HUMAN | Engulfment and cell motility protein 2 OS=Homo sapiens GN=ELMO2 PE=1 SV=2 | 97.4 (M:97.4) | 2 |
| RPAB3_HUMAN | DNA-directed RNA polymerases I, II, and III subunit RPABC3 OS=Homo sapiens GN=POLR2H PE=1 SV=4 | 91.1 (M:91.1) | 1 |
| FKB15_HUMAN | FK506-binding protein 15 OS=Homo sapiens GN=FKBP15 PE=1 SV=2 | 90.6 (M:90.6) | 2 |
| CDC16_HUMAN | Cell division cycle protein 16 homolog OS=Homo sapiens GN=CDC16 PE=1 SV=2 | 90.6 (M:90.6) | 2 |
| H2A2B_HUMAN | Histone H2A type 2-B OS=Homo sapiens GN=HIST2H2AB PE=1 SV=3 | 89.9 (M:89.9) | 2 |
| KS6A3_HUMAN | Ribosomal protein S6 kinase alpha-3 OS=Homo sapiens GN=RPS6KA3 PE=1 SV=1 | 89.6 (M:89.6) | 2 |
| IMA1_HUMAN | Importin subunit alpha-1 OS=Homo sapiens GN=KPNA1 PE=1 SV=2 | 89.5 (M:89.5) | 2 |
| KC1A_HUMAN | Casein kinase I isoform alpha OS=Homo sapiens GN=CSNK1A1 PE=1 SV=2 | 89.2 (M:89.2) | 2 |
| CDK7_HUMAN | Cell division protein kinase 7 OS=Homo sapiens GN=CDK7 PE=1 SV=1 | 88.5 (M:88.5) | 2 |
| TF3C5_HUMAN | General transcription factor 3C polypeptide 5 OS=Homo sapiens GN=GTF3C5 PE=1 SV=2 | 88.1 (M:88.1) | 2 |
| DEK_HUMAN | Protein DEK OS=Homo sapiens GN=DEK PE=1 SV=1 | 86.6 (M:86.6) | 2 |
| UBP14_HUMAN | Ubiquitin carboxyl-terminal hydrolase 14 OS=Homo sapiens GN=USP14 PE=1 SV=3 | 86.5 (M:86.5) | 1 |
| APC1_HUMAN | Anaphase-promoting complex subunit 1 OS=Homo sapiens GN=ANAPC1 PE=1 SV=1 | 84.9 (M:84.9) | 2 |
| E2AK2_HUMAN | Interferon-induced, double-stranded RNA-activated protein kinase OS=Homo sapiens GN=EIF2AK2 PE=1 SV=2 | 83.7 (M:83.7) | 2 |
| EXOS4_HUMAN | Exosome complex exonuclease RRP41 OS=Homo sapiens GN=EXOSC4 PE=1 SV=3 | 80.5 (M:80.5) | 2 |
| XRCC1_HUMAN | DNA repair protein XRCC1 OS=Homo sapiens GN=XRCC1 PE=1 SV=1 | 80.0 (M:80.0) | 2 |
| ITPR1_HUMAN | Inositol 1,4,5-trisphosphate receptor type 1 OS=Homo sapiens GN=ITPR1 PE=1 SV=2 | 79.6 (M:79.6) | 2 |

| | | | |
|---|---|---|---|
| ZFPL1_HUMAN | Zinc finger protein-like 1 OS=Homo sapiens GN=ZFPL1 PE=1 SV=2 | 78.6 (M:78.6) | 2 |
| DDX49_HUMAN | Probable ATP-dependent RNA helicase DDX49 OS=Homo sapiens GN=DDX49 PE=1 SV=1 | 77.2 (M:77.2) | 1 |
| ISY1_HUMAN | Pre-mRNA-splicing factor ISY1 homolog OS=Homo sapiens GN=ISY1 PE=1 SV=2 | 74.6 (M:74.6) | 2 |
| SRP72_HUMAN | Signal recognition particle 72 kDa protein OS=Homo sapiens GN=SRP72 PE=1 SV=3 | 74.1 (M:74.1) | 2 |
| ANC2_HUMAN | Anaphase-promoting complex subunit 2 OS=Homo sapiens GN=ANAPC2 PE=1 SV=1 | 74.0 (M:74.0) | 1 |
| LCK_HUMAN | Tyrosine-protein kinase Lck OS=Homo sapiens GN=LCK PE=1 SV=6 | 72.9 (M:72.9) | 2 |
| PRP19_HUMAN | Pre-mRNA-processing factor 19 OS=Homo sapiens GN=PRPF19 PE=1 SV=1 | 72.5 (M:72.5) | 2 |
| EIF3J_HUMAN | Eukaryotic translation initiation factor 3 subunit J OS=Homo sapiens GN=EIF3J PE=1 SV=2 | 69.1 (M:69.1) | 2 |
| RPF2_HUMAN | Ribosome production factor 2 homolog OS=Homo sapiens GN=RPF2 PE=1 SV=2 | 69.0 (M:69.0) | 2 |
| DDX55_HUMAN | ATP-dependent RNA helicase DDX55 OS=Homo sapiens GN=DDX55 PE=1 SV=2 | 67.2 (M:67.2) | 1 |
| MCM3A_HUMAN | 80 kDa MCM3-associated protein OS=Homo sapiens GN=MCM3AP PE=1 SV=2 | 66.8 (M:66.8) | 2 |
| TBL1R_HUMAN | F-box-like/WD repeat-containing protein TBL1XR1 OS=Homo sapiens GN=TBL1XR1 PE=1 SV=1 | 66.7 (M:66.7) | 2 |
| RM14_HUMAN | 39S ribosomal protein L14, mitochondrial OS=Homo sapiens GN=MRPL14 PE=1 SV=1 | 66.6 (M:66.6) | 1 |
| SMRD2_HUMAN | SWI/SNF-related matrix-associated actin-dependent regulator of chromatin subfamily D member 2 OS=Homo sapiens GN=SMARCD2 PE=1 SV=2 | 66.5 (M:66.5) | 1 |
| NU153_HUMAN | Nuclear pore complex protein Nup153 OS=Homo sapiens GN=NUP153 PE=1 SV=2 | 64.1 (M:64.1) | 2 |
| PNO1_HUMAN | RNA-binding protein PNO1 OS=Homo sapiens GN=PNO1 PE=1 SV=1 | 62.2 (M:62.2) | 1 |
| UBE2S_HUMAN | Ubiquitin-conjugating enzyme E2 S OS=Homo sapiens GN=UBE2S PE=1 SV=2 | 61.3 (M:61.3) | 2 |

| | | | |
|---|---|---|---|
| PDC6I_HUMAN | Programmed cell death 6-interacting protein OS=Homo sapiens GN=PDCD6IP PE=1 SV=1 | 60.8 (M:60.8) | 1 |
| GUAA_HUMAN | GMP synthase [glutamine-hydrolyzing] OS=Homo sapiens GN=GMPS PE=1 SV=1 | 60.4 (M:60.4) | 2 |
| FA98A_HUMAN | Protein FAM98A OS=Homo sapiens GN=FAM98A PE=1 SV=1 | 59.6 (M:59.6) | 1 |
| TRA2A_HUMAN | Transformer-2 protein homolog alpha OS=Homo sapiens GN=TRA2A PE=1 SV=1 | 59.4 (M:59.4) | 2 |
| RFA3_HUMAN | Replication protein A 14 kDa subunit OS=Homo sapiens GN=RPA3 PE=1 SV=1 | 59.2 (M:59.2) | 2 |
| CPT1A_HUMAN | Carnitine O-palmitoyltransferase 1, liver isoform OS=Homo sapiens GN=CPT1A PE=1 SV=2 | 58.7 (M:58.7) | 1 |
| SELB_HUMAN | Selenocysteine-specific elongation factor OS=Homo sapiens GN=EEFSEC PE=1 SV=4 | 58.5 (M:58.5) | 1 |
| COPB_HUMAN | Coatomer subunit beta OS=Homo sapiens GN=COPB1 PE=1 SV=3 | 58.3 (M:58.3) | 2 |
| 2AAA_HUMAN | Serine/threonine-protein phosphatase 2A 65 kDa regulatory subunit A alpha isoform OS=Homo sapiens GN=PPP2R1A PE=1 SV=4 | 58.0 (M:58.0) | 2 |
| SNUT2_HUMAN | U4/U6.U5 tri-snRNP-associated protein 2 OS=Homo sapiens GN=USP39 PE=1 SV=2 | 58.0 (M:58.0) | 1 |
| ERD22_HUMAN | ER lumen protein retaining receptor 2 OS=Homo sapiens GN=KDELR2 PE=1 SV=1 | 57.5 (M:57.5) | 1 |
| MK67I_HUMAN | MKI67 FHA domain-interacting nucleolar phosphoprotein OS=Homo sapiens GN=MKI67IP PE=1 SV=1 | 56.0 (M:56.0) | 1 |
| PRP4_HUMAN | U4/U6 small nuclear ribonucleoprotein Prp4 OS=Homo sapiens GN=PRPF4 PE=1 SV=2 | 55.6 (M:55.6) | 2 |
| SDA1_HUMAN | Protein SDA1 homolog OS=Homo sapiens GN=SDAD1 PE=1 SV=2 | 55.3 (M:55.3) | 2 |
| TITIN_HUMAN | Titin OS=Homo sapiens GN=TTN PE=1 SV=2 | 55.1 (M:55.1) | 1 |
| TF2H1_HUMAN | General transcription factor IIH subunit 1 OS=Homo sapiens GN=GTF2H1 PE=1 SV=1 | 53.4 (M:53.4) | 1 |
| STXB1_HUMAN | Syntaxin-binding protein 1 OS=Homo sapiens GN=STXBP1 PE=1 SV=1 | 53.4 (M:53.4) | 1 |
| IMA4_HUMAN | Importin subunit alpha-4 OS=Homo sapiens GN=KPNA4 PE=1 SV=1 | 52.2 (M:52.2) | 1 |

| | | | |
|---|---|---|---|
| CLPB_HUMAN | Caseinolytic peptidase B protein homolog OS=Homo sapiens GN=CLPB PE=1 SV=1 | 51.3 (M:51.3) | 1 |
| C19L1_HUMAN | CWF19-like protein 1 OS=Homo sapiens GN=CWF19L1 PE=1 SV=2 | 50.8 (M:50.8) | 1 |
| ACO13_HUMAN | Acyl-coenzyme A thioesterase 13 OS=Homo sapiens GN=ACOT13 PE=1 SV=1 | 50.7 (M:50.7) | 1 |
| WDR5_HUMAN | WD repeat-containing protein 5 OS=Homo sapiens GN=WDR5 PE=1 SV=1 | 50.5 (M:50.5) | 1 |
| S35E1_HUMAN | Solute carrier family 35 member E1 OS=Homo sapiens GN=SLC35E1 PE=1 SV=2 | 50.5 (M:50.5) | 1 |
| LASS2_HUMAN | LAG1 longevity assurance homolog 2 OS=Homo sapiens GN=LASS2 PE=1 SV=1 | 49.7 (M:49.7) | 1 |
| T2EA_HUMAN | General transcription factor IIE subunit 1 OS=Homo sapiens GN=GTF2E1 PE=1 SV=2 | 49.7 (M:49.7) | 1 |
| NIP7_HUMAN | 60S ribosome subunit biogenesis protein NIP7 homolog OS=Homo sapiens GN=NIP7 PE=1 SV=1 | 49.5 (M:49.5) | 1 |
| RFX3_HUMAN | Transcription factor RFX3 OS=Homo sapiens GN=RFX3 PE=2 SV=2 | 49.2 (M:49.2) | 1 |
| PSDE_HUMAN | 26S proteasome non-ATPase regulatory subunit 14 OS=Homo sapiens GN=PSMD14 PE=1 SV=1 | 48.9 (M:48.9) | 1 |
| RB12B_HUMAN | RNA-binding protein 12B OS=Homo sapiens GN=RBM12B PE=1 SV=2 | 48.8 (M:48.8) | 1 |
| QPCTL_HUMAN | Glutaminyl-peptide cyclotransferase-like protein OS=Homo sapiens GN=QPCTL PE=1 SV=1 | 48.0 (M:48.0) | 1 |
| IDH3A_HUMAN | Isocitrate dehydrogenase [NAD] subunit alpha, mitochondrial OS=Homo sapiens GN=IDH3A PE=1 SV=1 | 47.8 (M:47.8) | 1 |
| CCNH_HUMAN | Cyclin-H OS=Homo sapiens GN=CCNH PE=1 SV=1 | 47.4 (M:47.4) | 1 |
| OXSR1_HUMAN | Serine/threonine-protein kinase OSR1 OS=Homo sapiens GN=OXSR1 PE=1 SV=1 | 47.2 (M:47.2) | 1 |
| NUP37_HUMAN | Nucleoporin Nup37 OS=Homo sapiens GN=NUP37 PE=1 SV=1 | 46.5 (M:46.5) | 1 |
| PO2F1_HUMAN | POU domain, class 2, transcription factor 1 OS=Homo sapiens GN=POU2F1 PE=1 SV=2 | 46.3 (M:46.3) | 1 |
| WDR3_HUMAN | WD repeat-containing protein 3 OS=Homo sapiens GN=WDR3 PE=1 SV=1 | 45.8 (M:45.8) | 1 |

| | | | |
|---|---|---|---|
| MAT1_HUMAN | CDK-activating kinase assembly factor MAT1 OS=Homo sapiens GN=MNAT1 PE=1 SV=1 | 44.5 (M:44.5) | 2 |
| DMAP1_HUMAN | DNA methyltransferase 1-associated protein 1 OS=Homo sapiens GN=DMAP1 PE=1 SV=1 | 44.4 (M:44.4) | 2 |
| SOSSC_HUMAN | SOSS complex subunit C OS=Homo sapiens GN=SSBIP1 PE=1 SV=1 | 44.3 (M:44.3) | 1 |
| IF2A_HUMAN | Eukaryotic translation initiation factor 2 subunit 1 OS=Homo sapiens GN=EIF2S1 PE=1 SV=3 | 44.3 (M:44.3) | 1 |
| SCAM2_HUMAN | Secretory carrier-associated membrane protein 2 OS=Homo sapiens GN=SCAMP2 PE=1 SV=2 | 43.8 (M:43.8) | 1 |
| RBM46_HUMAN | Probable RNA-binding protein 46 OS=Homo sapiens GN=RBM46 PE=2 SV=1 | 43.7 (M:43.7) | 1 |
| PSMD1_HUMAN | 26S proteasome non-ATPase regulatory subunit 1 OS=Homo sapiens GN=PSMD1 PE=1 SV=2 | 43.6 (M:43.6) | 1 |
| ORC2_HUMAN | Origin recognition complex subunit 2 OS=Homo sapiens GN=ORC2L PE=1 SV=2 | 43.3 (M:43.3) | 1 |
| MGN_HUMAN | Protein mago nashi homolog OS=Homo sapiens GN=MAGOH PE=1 SV=1 | 42.4 (M:42.4) | 1 |
| NF1_HUMAN | Neurofibromin OS=Homo sapiens GN=NF1 PE=1 SV=2 | 42.3 (M:42.3) | 1 |
| VPS16_HUMAN | Vacuolar protein sorting-associated protein 16 homolog OS=Homo sapiens GN=VPS16 PE=1 SV=2 | 42.3 (M:42.3) | 1 |
| TERA_HUMAN | Transitional endoplasmic reticulum ATPase OS=Homo sapiens GN=VCP PE=1 SV=4 | 42.0 (M:42.0) | 2 |
| NFIC_HUMAN | Nuclear factor 1 C-type OS=Homo sapiens GN=NFIC PE=1 SV=2 | 41.8 (M:41.8) | 1 |
| THOC4_HUMAN | THO complex subunit 4 OS=Homo sapiens GN=THOC4 PE=1 SV=3 | 41.2 (M:41.2) | 1 |
| NACC1_HUMAN | Nucleus accumbens-associated protein 1 OS=Homo sapiens GN=NACC1 PE=1 SV=1 | 40.0 (M:40.0) | 1 |
| SLFN5_HUMAN | Schlafen family member 5 OS=Homo sapiens GN=SLFN5 PE=1 SV=1 | 39.3 (M:39.3) | 1 |
| SC61B_HUMAN | Protein transport protein Sec61 subunit beta OS=Homo sapiens GN=SEC61B PE=1 SV=2 | 38.7 (M:38.7) | 1 |
| CALR_HUMAN | Calreticulin OS=Homo sapiens GN=CALR PE=1 SV=1 | 37.9 (M:37.9) | 1 |
| TF2H4_HUMAN | General transcription factor IIH subunit 4 OS=Homo sapiens GN=GTF2H4 PE=2 SV=1 | 37.7 (M:37.7) | 1 |

| | | | |
|---|---|---|---|
| NGDN_HUMAN | Neuroguidin OS=Homo sapiens GN=NGDN PE=1 SV=1 | 37.2 (M:37.2) | 1 |
| EXOS6_HUMAN | Exosome complex exonuclease MTR3 OS=Homo sapiens GN=EXOSC6 PE=1 SV=1 | 36.4 (M:36.4) | 1 |
| NHEJ1_HUMAN | Non-homologous end-joining factor 1 OS=Homo sapiens GN=NHEJ1 PE=1 SV=1 | 36.3 (M:36.3) | 1 |
| YIF1B_HUMAN | Protein YIF1B OS=Homo sapiens GN=YIF1B PE=1 SV=1 | 35.9 (M:35.9) | 1 |
| NIPA_HUMAN | Nuclear-interacting partner of ALK OS=Homo sapiens GN=ZC3HC1 PE=1 SV=1 | 35.7 (M:35.7) | 1 |
| EDC4_HUMAN | Enhancer of mRNA-decapping protein 4 OS=Homo sapiens GN=EDC4 PE=1 SV=1 | 35.3 (M:35.3) | 1 |
| PHF5A_HUMAN | PHD finger-like domain-containing protein 5A OS=Homo sapiens GN=PHF5A PE=1 SV=1 | 35.0 (M:35.0) | 1 |
| VPS53_HUMAN | Vacuolar protein sorting-associated protein 53 homolog OS=Homo sapiens GN=VPS53 PE=1 SV=1 | 34.7 (M:34.7) | 1 |
| UNC5B_HUMAN | Netrin receptor UNC5B OS=Homo sapiens GN=UNC5B PE=1 SV=2 | 34.3 (M:34.3) | 1 |
| AZI1_HUMAN | 5-azacytidine-induced protein 1 OS=Homo sapiens GN=AZI1 PE=1 SV=2 | 34.3 (M:34.3) | 1 |
| DOCK5_HUMAN | Dedicator of cytokinesis protein 5 OS=Homo sapiens GN=DOCK5 PE=1 SV=3 | 34.0 (M:34.0) | 1 |
| AP1M1_HUMAN | AP-1 complex subunit mu-1 OS=Homo sapiens GN=AP1M1 PE=1 SV=3 | 33.5 (M:33.5) | 1 |
| RL3L_HUMAN | 60S ribosomal protein L3-like OS=Homo sapiens GN=RPL3L PE=1 SV=3 | 33.2 (M:33.2) | 1 |
| CSN6_HUMAN | COP9 signalosome complex subunit 6 OS=Homo sapiens GN=COPS6 PE=1 SV=1 | 33.0 (M:33.0) | 1 |
| AURKB_HUMAN | Serine/threonine-protein kinase 12 OS=Homo sapiens GN=AURKB PE=1 SV=2 | 32.8 (M:32.8) | 1 |
| RL1D1_HUMAN | Ribosomal L1 domain-containing protein 1 OS=Homo sapiens GN=RSL1D1 PE=1 SV=3 | 32.4 (M:32.4) | 1 |
| GOGA7_HUMAN | Golgin subfamily A member 7 OS=Homo sapiens GN=GOLGA7 PE=1 SV=2 | 32.2 (M:32.2) | 1 |
| LRC47_HUMAN | Leucine-rich repeat-containing protein 47 OS=Homo sapiens GN=LRRC47 PE=1 SV=1 | 31.8 (M:31.8) | 1 |
| TEKT2_HUMAN | Tektin-2 OS=Homo sapiens GN=TEKT2 PE=1 SV=1 | 30.0 (M:30.0) | 1 |

*6.3 Salt-Extracted Chromatin*

| Accession | Protein | Scores | #Peptides |
|---|---|---|---|
| APC5_HUMAN | Anaphase-promoting complex subunit 5 OS=Homo sapiens GN=ANAPC5 PE=1 SV=2 | 338.2 (M:338.2) | 7 |
| APC1_HUMAN | Anaphase-promoting complex subunit 1 OS=Homo sapiens GN=ANAPC1 PE=1 SV=1 | 314.8 (M:314.8) | 9 |
| H2A1H_HUMAN | Histone H2A type 1-H OS=Homo sapiens GN=HIST1H2AH PE=1 SV=3 | 115.6 (M:115.6) | 4 |
| H12_HUMAN | Histone H1.2 OS=Homo sapiens GN=HIST1H1C PE=1 SV=2 | 106.1 (M:106.1) | 2 |
| MGST3_HUMAN | Microsomal glutathione S-transferase 3 OS=Homo sapiens GN=MGST3 PE=1 SV=1 | 63.8 (M:63.8) | 1 |
| RPH3L_HUMAN | Rab effector Noc2 OS=Homo sapiens GN=RPH3AL PE=1 SV=1 | 29.7 (M:29.7) | 1 |
| NOP58_HUMAN | Nucleolar protein 58 OS=Homo sapiens GN=NOP58 PE=1 SV=1 | 28.6 (M:28.6) | 1 |
| SYTL4_HUMAN | Synaptotagmin-like protein 4 OS=Homo sapiens GN=SYTL4 PE=1 SV=1 | 27.7 (M:27.7) | 1 |
| DPOE1_HUMAN | DNA polymerase epsilon catalytic subunit A OS=Homo sapiens GN=POLE PE=1 SV=5 | 25.6 (M:25.6) | 1 |
| S4A7_HUMAN | Sodium bicarbonate cotransporter 3 OS=Homo sapiens GN=SLC4A7 PE=1 SV=2 | 24.8 (M:24.8) | 1 |
| NH2L1_HUMAN | NHP2-like protein 1 OS=Homo sapiens GN=NHP2L1 PE=1 SV=3 | 24.6 (M:24.6) | 1 |
| MGST1_HUMAN | Microsomal glutathione S-transferase 1 OS=Homo sapiens GN=MGST1 PE=1 SV=1 | 23.7 (M:23.7) | 1 |
| CDC23_HUMAN | Cell division cycle protein 23 homolog OS=Homo sapiens GN=CDC23 PE=1 SV=3 | 23.0 (M:23.0) | 1 |

# Development of a Spheroid Model to Investigate Heterogeneity in Glioblastoma

This project is submitted in partial fulfilment of the requirements for the award of Master of Research (MRes)

# ABSTRACT

Glioblastoma (GBM) is the most common and most aggressive form of brain cancer. Current treatment involves concomitant radiotherapy and chemotherapy with the drug Temozolomide (TMZ), but the median survival is still only around a year. Transcriptional profiling studies revealed different subtypes of GBM with distinct patterns of gene expression that are linked to specific genetic alterations. In this study, cell lines were used to represent the different subtypes. They were cultured as 3D spheroids, which have been shown to be more representative of GBM tumours than monolayers. Confocal imaging of polyclonal spheroids showed the subtypes form distinct populations that reflect their preference for different positions within the spheroid, suggesting an arrangement that confers a survival advantage to the cells. The effect of TMZ treatment was studied, with different effects seen both between 2D and monoclonal spheroid culture, and between the different subtypes with varying morphological changes following treatment. The results show that spheroid culture is a promising method in GBM model development. However, problems were encountered that hindered imaging of polyclonal spheroids. More work is needed to optimise the method to improve spheroid size uniformity and fluorescent signal of the cell lines.

# CONTENTS

# 1. INTRODUCTION

Glioma is the most common form of primary brain tumour, accounting for approximately 80% of all malignant central nervous system (CNS) tumours (Agnihotri et al., 2012). Gliomas histologically resemble types of glial cells, such as astrocytes and oligodendrocytes, and are classified (according to the 2007 WHO classification, Louis et al., 2007) based on their presumed cell of origin, such as astrocytomas, oligodendrogliomas and oligoastrocytomas. The tumours are then further classified into four histopathological grades, based on the degree of malignancy, which provide information on prognosis and are characterised by features associated with proliferation, angiogenesis and necrosis (Louis et al., 2007; Vitucci et al., 2011).

Glioblastoma (GBM), a grade IV astrocytoma, is the most common and most aggressive glioma (Ostrom et al., 2013). There is currently no cure; GBM patients have a poor prognosis with a median survival of just 4.6 months, increasing to only 14.6 months upon therapy (Stupp et al., 2005). The current treatment involves surgery to remove the bulk of the tumour, followed by concomitant radiotherapy and chemotherapy with the alkylating agent temozolomide (TMZ). The location and extensive diffusion of the tumour throughout the brain often means it is impossible to remove the tumour entirely without causing damage (Mrugala, 2013), while the blood-brain barrier hinders drug delivery to the site of tumour, with only low concentrations being found around the tumour of even effective drugs (Portnow et al., 2009). Tumour recurrence consistently occurs, along with the

development of therapy resistance (Omuro et al., 2007). Thus, a better understanding of GBM is needed in order to improve the management and treatment of the disease.

Many high dimensional profiling studies have been conducted to further understand tumourigenesis in GBM (TCGA, 2008; Parsons et al., 2008). The Cancer Genome Atlas (TCGA) research network underwent a study to characterise the genome alterations in GBM (TCGA, 2008). They analysed DNA copy number, gene expression and DNA methylation aberrations in 206 GBM samples, plus nucleotide sequence aberrations in 601 genes from 91 samples using Sanger sequencing and microarray technology. The results revealed numerous novel mutations and genome aberrations, as well as confirming previously known mutations. Mapping of the genetic alterations onto major signalling pathways implicated in GBM, namely the p53, RB and receptor tyrosine kinase (RTK) pathways (Furnari et al., 2007) (Fig. 1), showed that 87%, 78% and 88% of the GBM samples harboured genetic alterations in these pathways, respectively. Indeed, the majority of the samples (74%) possessed genetic alterations in all three pathways (TCGA, 2008), helping the tumour cell to promote proliferation and survival, while escaping cell-cycle checkpoints, senescence and apoptosis (Chen et al., 2012). These results suggest that deregulation of the three pathways is an essential requirement for GBM pathogenesis (TCGA, 2008).

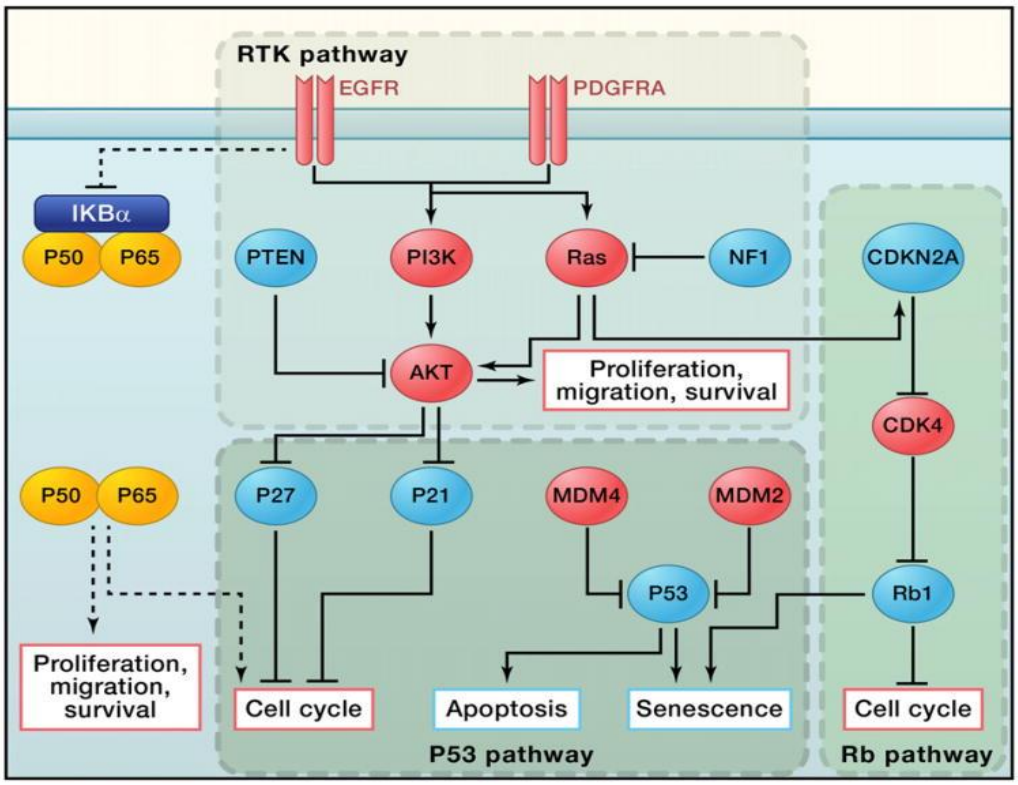


**Figure 1 – Major signalling pathways in GBM tumourigenesis**
Illustration of the key signalling pathways – the RTK, p53, and Rb pathways - that are mutated in GBM pathogenesis. Oncogenes are highlighted in red, while blue indicates tumour suppressor genes (Chen et al., 2012).

Although there are some conserved aberrations in GBM, there is great variability in biological behaviour between different tumours, with differences in prognosis and response to treatment commonly seen despite tumours sharing the same WHO histopathological grade (Vitucci et al., 2011). There are two main categories of GBM: primary and secondary (Louis et al., 2007). Primary GBM accounts for around 95% of all GBM cases and mainly occurs in older patients, with a mean of 62 years old (Ohgaki et al., 2004). These tumours arise de novo, resulting from the accumulation of multiple genetic aberrations. Secondary GBM, on the other hand, has a median patient age of 45 years old and develops over 5-10 years from low-grade astrocytoma (Ohgaki and Kleihues, 2007). These categories are

morphologically and clinically indistinguishable, but genome-wide analyses have shown there are marked genomic differences between primary and secondary GBM (Maher et al., 2006), suggesting that different types of treatment may be needed for each.

As well as differences between tumours, significant intratumoural heterogeneity has been found (Zheng et al., 2012). Gene expression profiling studies have revealed differences between samples from different regions of the same tumour, which are unrelated to differences in histology (Liang et al., 2005). Furthermore, DNA copy number analysis of various samples taken from one tumour showed that GBM tumours have genetic alterations that are common to all areas of the tumour, as well as some that are area-specific (Nobusawa et al., 2010).

Several studies have used gene expression profiling to classify histologically-indistinguishable GBM tumour samples into specific subtypes (Huse et al., 2011; Dunn et al., 2012). Initial profiling studies identified subclasses of GBM by analysing gene expression signatures associated with prognosis/survival or response to therapy (Nutt et al., 2003; Freije et al., 2004; Phillips et al., 2006). Phillips et al. (2006) used 107 grade III and grade IV astrocytoma samples, separating them into groups of short and long survival. Microarrays were used to profile the gene expression in the two groups and two-way cluster analysis performed with the genes whose expression most strongly correlated with survival. Three subclasses were identified, characterised by a 35-gene signature, named Proneural, Proliferative or Mesenchymal, based on the expression of genes

characteristic of the corresponding tissues (Phillips et al., 2006). Similar groups were also found by Freije et al. (2004), who looked at survival-associated transcription in 85 diffuse gliomas of all types. The Proneural subtype was the least aggressive and had the best outcome, while the Proliferative and Mesenchymal subtypes had a worse outcome and had higher expression of markers for proliferation and angiogenesis (Freije et al., 2004; Phillips et al., 2006).

More recently, gene expression profiling studies were used to identify GBM subtypes with transcriptional signatures associated with alterations in DNA sequence and copy number (Verhaak et al., 2010). Verhaak et al. (2010) analysed the TCGA microarray gene expression data (thus only GBMs were included), isolated the variably expressed genes (totalling at 1740, not specifically related to survival) and performed unsupervised hierarchical clustering. This resulted in four significantly different subtypes, with a 210-characteristic gene signature per class, named (following the previously established subtype titles) Classical, Mesenchymal, Proneural and Neural. These subtypes were validated using an independent data set of 260 GBM samples (including those analysed by Phillips et al.) and gene expression data obtained from a collection of xenografts (patient specimens implanted in null mice, Hodgson et al., 2009). The patterns of the four subtypes were well recapitulated by the validation data set, while Proneural, Classical and Mesenchymal subtypes were also reflected in the xenografts (Verhaak et al., 2010), supporting the use of this subclassification in GBM.

The four subtypes can be characterised by specific genomic events (Verhaak et al., 2010; Huse et al., 2011; Omuro and DeAngelis, 2013) (Fig. 2, Table 1). The Classical subtype is characterised by *EGFR* amplification, which was observed in 97% of the Classical samples while infrequently in other subtypes, as well as a point (or vIII) *EGFR* mutation leading to constitutive receptor activation. *CDKN2A* (*INK4A/ARF*) deletion is frequently present, although there is a lack of TP53 mutations in the Classical subtype, despite it being the most commonly mutated gene in GBM (TCGA, 2008). The Mesenchymal subtype is associated with *NF1* mutation/deletion and high expression of mesenchymal markers, such as *CHI3L1* and *MET*, and genes involved in the tumour necrosis factor and NF-κB pathways. The Proneural subtype is enriched for mutations in *IDH1* and *TP53* (as well as *TP53* loss of heterozygosity), plus amplification of *PDGFRA*. Finally, the Neural subtype shows high expression of neuronal markers, but has no distinct aberrations from the other classes.

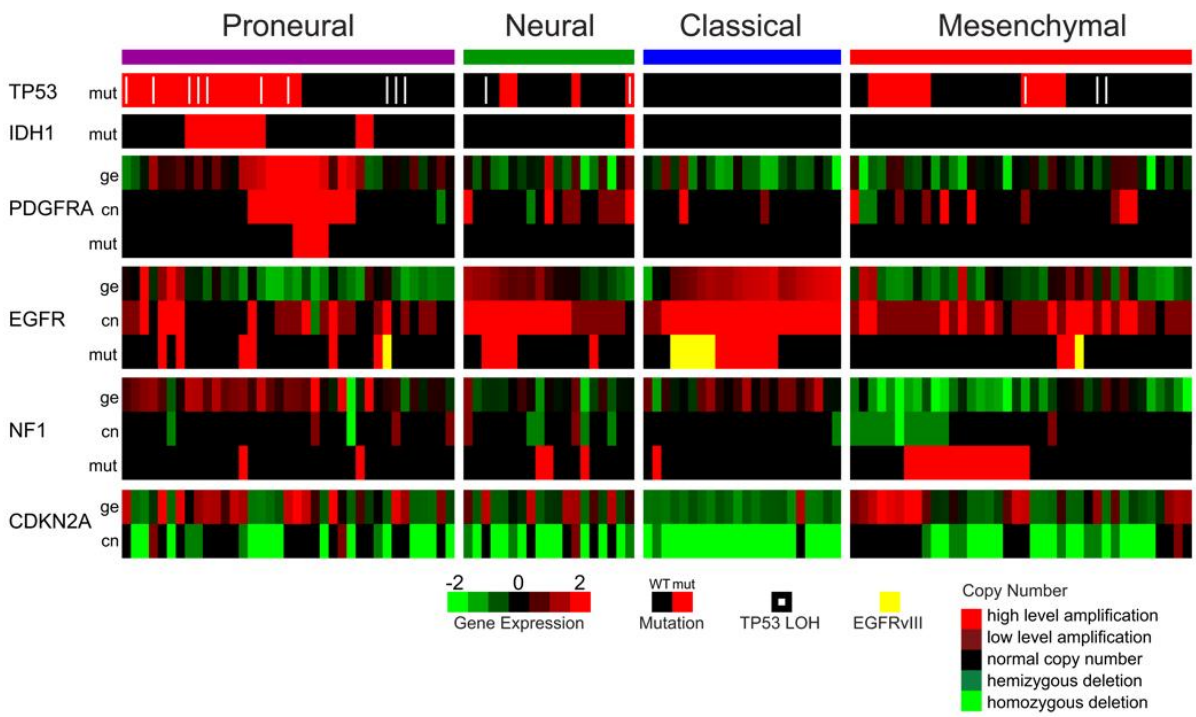


**Figure 2 – Genomic alterations in different GBM subtypes**

Diagram showing the data for gene expression, mutations and copy number changes for 116 GBM samples, organised into the four subtypes. Gene expression (ge) data was standardised (mean equal to zero, standard deviation equal to 1) and levels illustrated, with green for low expression and red for high expression. Mutations (mut) are indicated by a red square (EGFRvIII is specifically shown by a yellow square) and loss of heterozygosity by a white line. Copy number changes (cn) are indicated with bright red for high level amplification, dark red for low level amplification, dark green for hemizygous deletions and bright green for homozygous deletions. Black shows no alterations present in the sample. (Verhaak et al., 2010)

| Gene | Proneural (n=37) | Neural (n=19) | Classical (n=22) | Mesenchymal (n=38) | Total #Mut |
|---|---|---|---|---|---|
| **TP53** | **20 (54%)** | 4 (21%) | **0 (0%)** | 12 (32%) | 36 |
| **PTEN** | 6 (16%) | 4 (21%) | 5 (23%) | 12 (32%) | 27 |
| **NF1** | 2 (5%) | 3 (16%) | 1 (5%) | **14 (37%)** | 20 |
| **EGFR** | 6 (16%) | 5 (26%) | 7 (32%) | 2 (5%) | 20 |
| **IDH1** | **11 (30%)*** | 1 (5%) | 0 (0%) | 0 (0%) | 12 |
| **PIK3R1** | 7 (19%) | 2 (11%) | 1 (5%) | 0 (0%) | 10 |
| **RB1** | 1 (3%) | 1 (5%) | 0 (0%) | 5 (13%) | 7 |
| **ERBB2** | 2 (5%) | 3 (16%) | 1 (5%) | 1 (3%) | 7 |
| **EGFRvIII** | 1 (3%) | 0 (0%) | 5 (23%) | 1 (3%) | 7 |
| **PIK3CA** | 3 (8%) | 1 (5%) | 1 (5%) | 1 (3%) | 6 |
| **PDGFRA** | 4 (11%) | 0 (0%) | 0 (0%) | 0 (0%) | 4 |

**Table 1 – Frequency of aberrations in frequently-mutated genes between the different GBM subtypes**
The number of samples in which alterations in each gene were detected within the Verhaak et al., dataset is shown. The significance of the frequency of each event in each subtype compared to the remaining subtypes was determined (two-sided Fisher's test) and significant aberrations indicated using bold ($p<0.1$) and an asterisk ($p<0.01$) (Verhaak et al., 2010).

However, mRNA levels do not always correlate with protein levels. Thus, Brennan et al. (2009) performed proteomic analysis on 27 surgical glioma samples. Using unsupervised clustering, they found three distinct subtypes based on the pattern of activation of glioma-associated signalling pathways, each associated with EGFR activation, PDGFRA activation, or loss of NF1 (Brennan et al., 2009). These classes correspond well with the Classical, Proneural and Mesenchymal subclasses of GBM determined using TCGA data, in which aberrations of E*GFR*, *PDGFRA* and *NF1* are signature events, respectively (Verhaak et al., 2010).

Across several studies, the number of GBM subtypes varies between 2 and 4, with no consensus as of yet. Part of the reason for this is likely due to lack of consistency in samples sets and methodology (Zheng et al., 2012). Re-analysis of both the Phillips et al. and Verhaak et al. samples using the other's subtype signatures revealed good agreement between the Mesenchymal and Proneural subtypes. However, there was little concordance between the other subtypes. One reason for this may be that while the Proneural and Mesenchymal signatures in the Phillips et al. study were mostly mutually exclusive, elements of the Proliferative signature were often found in the other signatures and so may not have been defined as a subtype using the Verhaak method (Huse et al., 2011).

The classification of GBM into subtypes has been linked to differences in survival (Phillips et al., 2004) and treatment efficacy (Verhaak et al., 2010). Comparison of data from patients undergoing intensive radio-/chemotherapy compared to those undergoing noncurrent or short chemotherapy treatments showed that aggressive therapy significantly reduced mortality in the Verhaak Classical and Mesenchymal subtypes, with some effect in Neural subtypes too, but there was no change in survival in the Proneural subtype (the subtype which also correlated with longer patient survival) (Verhaak et al., 2010) (Fig. 3). This suggests different subtypes may require different therapies. Thus, studies have been done to try and improve diagnosis of GBM to be able to identify the subtypes present and so give improved prognosis and, potentially, personalised treatment. One such study led to the development of an immunohistochemical method to look for expression of EGFR, p53 and PDGFR to allow classification into Classical (high EGFR, low

p53/PDGFR) or Proneural subtypes (high p53 and/or high PDGFR), showing the potential to be able to classify GBM with a simple method in daily practice (Le Mercier et al., 2012).

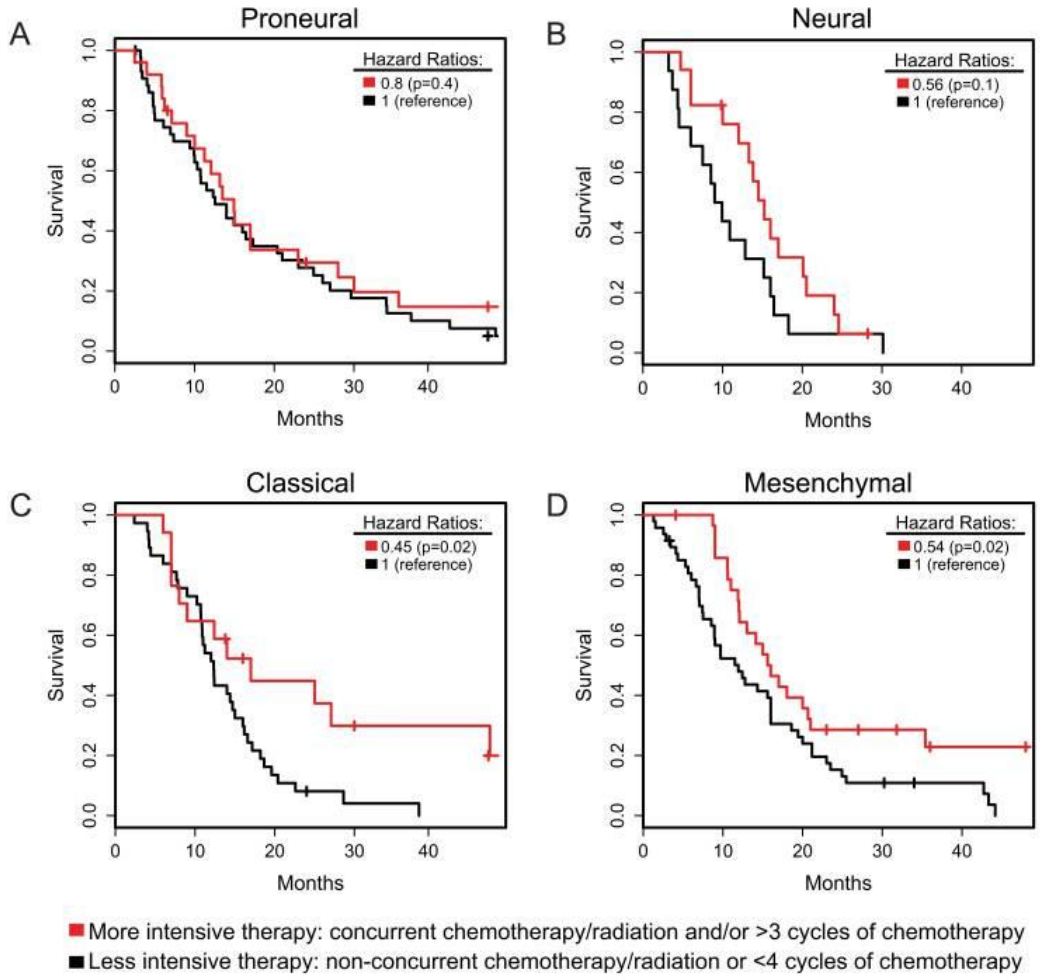


**Figure 3 – Different responses are shown by the four GBM subtypes to conventional therapy**

Patients within a dataset were classified based on the therapy given – a red line indicates intensive therapy (including concurrent radio- and chemotherapy or extended chemotherapy) and a black line represents less intensive therapy (non-concurrent radio- and chemotherapy or less than four cycles of chemotherapy). Patient survival (expressed as a ratio, starting at 1 before treatment) was plotted against time for each GBM subtype (Verhaak et al., 2010).

Several GBM cell lines have been established, some of which can be used to represent the distinct Verhaak subtypes Classical, Mesenchymal and Proneural, such as U343, U373 and U87 respectively. Each possesses the characteristic genomic aberration of the corresponding subtypes (namely, changes in *EGFR*, *IDH1* or *NF1* [Table 1, Table 2]). However, certain genetic alterations are lost in culture, including EGFR amplification (Schulte et al., 2012) and IDH1 mutation (Piaskowski et al., 2011). Although the cause is still debated, the observation that the genotype of cells cultured in xenografts, 3D culture or serum-free conditions more closely reflects that of the primary tumours suggests that these cell types could have stem cell-like properties and so are lost during normal cell culture (Lee et al., 2006; De Witt Hamer et al., 2008). Therefore, U87 has been engineered to contain a vector that expresses the IDH1 mutant (R132H) and so is not lost as it is not integrated into the genome, whereas U343 instead contains a mutation to give overexpression of *EGFR*, rather than amplification of the gene. These cell lines have greatly aided the investigation to further understand GBM.

| | **U343 (Classical)** | **U373 (Mesenchymal)** | **U87 (Proneural)** |
|---|---|---|---|
| **EGFR** | High expression | WT | WT |
| **NF1** | WT | Low/deletion | WT |
| **IDH1** | WT | WT | Heterozygous mutant (R132H) |
| P53 | WT | Mutant (R273Q) | WT |
| CDKN2A | Homozygous deletion | WT | Homozygous deletion |
| PDGFRA | WT | WT | Amplification |

**Table 2 – GBM tumour cell lines possess aberrations characteristic of the different GBM subtypes**
(Ishii et al., 1999; Hollinshead, personal communication)

Cellular spheroids are large clusters formed by spontaneous aggregation of cells and were among the first 3D cell culture models discovered and applied in research, often acting as tumour models (Hirschhaeuser et al., 2010; Pampaloni et al., 2013). They provide an intermediate between 2D monolayers and in vivo tumours. They have more complexity than monolayers and are more representative of tumours by better recreating cell-cell interactions and displaying areas of heterogeneity with, for example, proliferative cells focused on the edges of the spheroid, areas of necrosis and the presence of nutrient/oxygen gradients throughout to view hypoxic effects (Sutherland, 1998; Loessner et al., 2013). They are often used in drug development studies, displaying more resistance to drugs than 2D monolayers (Elliot and Yuan, 2011) and allowing the drug response to be modelled with relevant pathophysiological gradients/microenvironments, including hypoxia, which is associated with tumour aggressiveness and resistance to therapy in vivo (Amberger-Murphy, 2009)). Spheroids have also been shown to be more representative of GBM, specifically. Genomic profiling of primary cell and spheroid cultures from GBMs showed substantial genetic changes in 2D cell culture compared to the parental tumours, whereas spheroid cultures were genetically stable and retained characteristic aberrations, such as EGFR amplification (De Witt Hamer et al., 2008), suggesting spheroid culture allows a closer comparison to in vivo conditions.

### *1.1 Hypothesis and Aims*

Previous work has shown that the three GBM cell lines, U373, U343 and U87, can be cultured as 3D spheroids. The hypothesis of the present study was that spheroid cultures could be used as a more representative model of GBM tumours, using U373, U343 and U87 to represent intratumoural heterogeneity. The model could lead to a better understanding of the spatial arrangement of the three subtypes in a GBM tumour and their cellular interactions. Previous studies have also revealed differential sensitivity to conventional therapy between the subtypes. Thus, a further hypothesis was that a spheroid model of GBM could provide insights into the mechanism of preferential action of the drug TMZ between GBM subtypes in vivo. The aims were, therefore, to:

1. Develop a spheroidal model of GBM using fluorescently labelled U373, U343 and U87 to allow imaging by confocal microscopy
2. Investigate the response of the different cell lines in a spheroid culture to TMZ treatment

# 2. MATERIALS AND METHODS

*2.1 Cell and Spheroid Culture*

GBM cell lines (Table 2) were grown in Dulbecco's Modified Eagle's Medium (DMEM) supplemented with 2 mM L-glutamine and 10% (v/v) foetal calf serum (FCS), and incubated at 37°C C and 5% $CO_2$ in a humidified environment until confluent. For cell passaging, the medium was removed, before the cells were washed in PBS and incubated with trypsin solution (Gibco, Life Technologies) until all cells had detached from the dish. DMEM was then added to neutralise the trypsin and the cells re-plated at the appropriate density.

For spheroid culture, cells were seeded at a cell count of $1x10^6$ in 10 ml medium onto 0.5% (w/v) low melting point (LMP) agarose plates to prevent the cells adhering to the plastic dish. The plates were incubated at 37°C for 3 days, before the spheroids were harvested. The spheroids were collected on a 40 µm filter, the filter washed with PBS and the spheroids transferred to an Eppendorf tube. The samples were centrifuged (8000 rpm, 1 min) to pellet the spheroids, the liquid removed and the spheroids fixed by incubating at room temperature (RT) with 10% formalin for 1 hour.

Where appropriate, on the third day of growth on agarose plates, spheroids were treated with 1 mM TMZ, dissolved in DMSO, (plus a control plate treated with an equal volume of DMSO) and incubated for a further 3 days before harvesting.

*2.2 TMZ-Sensitivity Assay*

Each cell line was seeded onto 12-well plates at a cell density appropriate for rate of growth: U87 at $0.3x10^5$, U343 at $0.4x10^5$ and U373 at $0.1x10^5$ cells per well. The plates were incubated overnight at 37°C. The medium was aspirated and fresh medium added containing various concentrations of TMZ ranging 0 – 1 mM (with 3 wells for each concentration). For each TMZ plate, a control plate was used in which the equal volume of DMSO was added to account for any cell death due to DMSO alone. The plates were incubated at 37°C for 72 hours, before the cells were fixed by incubation for 30 mins at 4°C with 200 µl of 20% (w/v) *trichloroacetic acid (*TCA) per well. The plates were washed with water, allowed to dry and 0.4% (w/v) sulforhodamine B (SRB) in 1% (v/v) acetic acid added for 10 mins at RT to stain the cells. The plates were washed four times with 1% (v/v) acetic acid to remove any unbound dye and allowed to dry. The protein-bound dye was dissolved in 50 mM Tris solution (pH 8.8) and the absorbance at 510 nm measured using a microplate reader (FLUOstar Omega, BMG Labtech) with the absorbance proportional to cell number. TMZ cytotoxicity was calculated by dividing the absorbance of the non-treated cells by that of the TMZ-treated cells and normalising the value to that of the corresponding DMSO-treated plate.

*2.3 Western Blotting*

For 2D cell culture, the medium was removed from the plate and the cells washed three times in PBS. The cells were then harvested by scraping in ~500 µl RIPA buffer (plus protease inhibitors). For spheroid culture, cell spheroids were collected from the agarose plates and centrifuged (2000 rpm, 5 mins) to pellet the

cells. The supernatant was removed and the cells were washed with PBS, before the pellet was resuspended in ~150 µl RIPA buffer (with protease inhibitors).

Samples were incubated on ice for 20 minutes to lyse the cells and centrifuged at 13000 rpm for 15 mins at 4°C. The supernatant was retained and the protein concentration measured using a BCA protein assay (Thermo Scientific). Samples were diluted to give equal concentrations and added to an equal volume of 2x Laemmli sample buffer (Sigma-Aldrich), before boiling at 100°C for 10 mins to denature the proteins.

The proteins were separated using sodium dodecyl sulphate-polyacrylaminde gel electrophoresis (SDS-PAGE) and subsequently transferred to a nitrocellulose membrane using a wet-transfer method. The membranes were incubated with 5% (w/v) milk in PBST (0.1% (v/v) Tween 20 in 1x PBS) for 1 hour to block the membranes, before being incubated with the primary antibody (made to the correct dilution in 5% milk) (Table 3) and left on a rocker overnight at 4°C. The blots were washed in PBST to remove any unbound antibody and incubated with secondary antibody, mouse- or rabbit-IgG reactive HRP-linked antibody (cell signalling), for 1 hour on a shaker. Blots were then washed with PBST for 3x10 mins to remove unbound secondary antibody. Enhanced chemiluminescent (ECL) reagent (GE Healthcare) was added to the membrane to allow detection of the protein. The blots were exposed to x-ray film for the appropriate time and the film was developed.

*2.4 Immunofluorescence*

Spheroids were harvested and fixed, before centrifugation (8000 rpm, 1 min) to pellet the spheroids, the supernatant removed and the cells permeablised with 0.1% (v/v) Triton-X-100 in PBS for 20 mins. The samples were again centrifuged (8000 rpm, 1 min) and the spheroids incubated in 5% (w/v) BSA for 1 hour at RT. The BSA was removed and the samples incubated at 4°C overnight with 500 µl primary antibody (Table 3) in 1% (w/v) BSA on a spinner.

The spheroids were washed with PBS, centrifuged (8000 rpm, 1 min) and the supernatant removed. Secondary antibody, conjugated to a fluorescent dye (Dylight 649 Anti-rabbit/mouse-IgG, Vector Labs), was added in 250 µl PBS and incubated in the dark for 2 hours. The antibody was removed and the wash repeated. 500 µl PBS was added, along with a drop of Hoescht dye (Hoescht33342, Life Technologies) to stain the nuclei. The spheroids were added to chamber slides and 200 µl 1% (w/v) LMP agarose added to the top of the well to fix them in place.

| **Antibody** | **Western blot dilution** | **Immunofluorescence dilution** | **Species** | **Supplier** |
|---|---|---|---|---|
| β-actin | 1:2000 | - | Mouse | Sigma-Aldrich |
| EGFR | 1:500 | 1:50 | Rabbit | Santa Cruz |
| EGFR | - | 1:50 | Rabbit | Cell Signalling |
| HIF1α | - | 1:50 | Mouse | BD Biosciences |
| IDH1 R132H | 1:500 | - | Mouse | Dianova |
| NF1 | 1:500 | - | Rabbit | Abcam |

**Table 3 – Primary Antibodies**

*2.5 Confocal Microscopy*

Samples were imaged using a Zeiss LSM 510 confocal microscope, connected to an inverted Axiovert 200M microscope. The objective lens used was an EC Plan – Neofluar 20x with a numerical aperture of 0.5. Images were processed using the Zeiss LSM Image Browser software.

*2.6 Spheroid Size Measurements*

Spheroids were imaged on the agarose plates using a Zeiss Axiovert 25 inverted light microscope and subsequently captured and processed using the Scion VisiCapture software. The area of each spheroid was measured using ImageJ software and the value used to calculate the average radius of the spheroid according to $A = \pi r^2$. The volume was then approximated, assuming a sphere shape, using $V = \frac{4}{3}\pi r^3$.

*2.7 FACS*

Cells were grown in a monolayer until confluent. The medium was removed, the plate washed with PBS and the cells trypsinised. The trypsin was neutralised with the addition of medium and the cell solution centrifuged (1500 rpm, 5 mins). The supernatant was aspirated and the pellet resuspended in 1 ml PBS with gentamycin. The cells were passed through a 70 µm filter to remove any contaminants and subsequently sorted using FACS. The sorted cells were plated with antibiotic-containing medium to prevent infection following the FACS procedure.

# 3. RESULTS

*3.1 GBM Cell Lines Can be Classified into Distinct GBM Subtypes*

The aim of the present study was to use GBM-derived cell lines to develop a model of a GBM tumour. In order to confirm the supposed genetic alterations of the three cell lines, U87, U343 and U373, a Western blot was performed to analyse the relative levels of the NF1, EGFR and IDH1 (R132H) proteins in each cell type (Fig. 3).

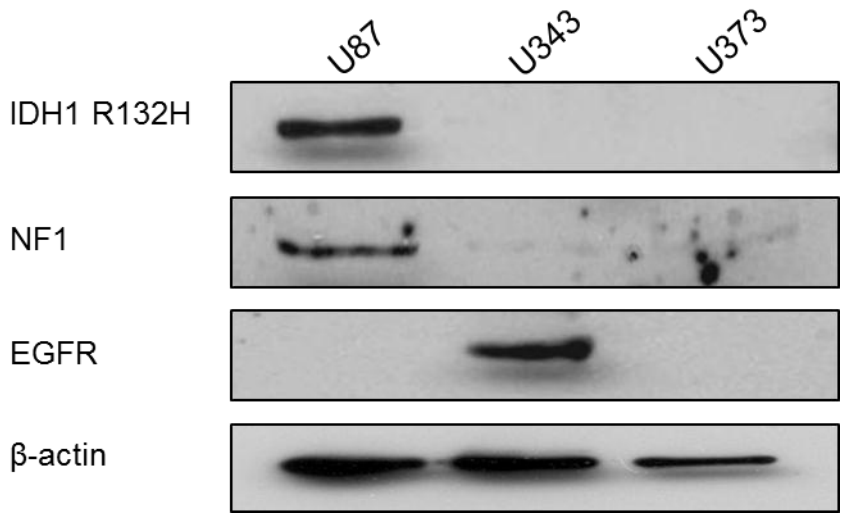


**Figure 3 – Expression of key protein markers for GBM subtypes in the cell lines U87, U343 and U373**
Cells were grown as a monolayer until confluent, harvested by scraping and lysed. The protein concentrations in each sample were measured and a Western Blot performed to observe the relative levels of EGFR, NF1 and IDH1 with the R132H mutation. β-actin was used as a loading control.

The results revealed that U87 cells solely expressed the IDH1 mutant protein, while possessing normal levels of both EGFR and NF1, whereas U373 cells displayed no/low NF1 protein levels, with no other aberrations detected. This

suggests that the U87 and U373 cell lines can be used to represent the Proneural and Mesenchymal GBM subtypes, respectively. U343 cells, however, also showed only low levels of NF1 (at levels similar to those in U373). Nonetheless, EGFR could only be detected in U343 cells, indicating the *EGFR* gene is indeed overexpressed in this cell line, which is a marker of the Classical subtype and thus, allowed the U343 cell line to be used to represent the Classical phenotype.

### *3.2 Sensitivity to TMZ Treatment Differs for Each Subtype In Vitro*

Previous studies have suggested that each GBM subtype has a different response to conventional therapy (radiotherapy with concomitant TMZ chemotherapy) in patients (Verhaak et al., 2010). The effects of TMZ treatment on each cell type grown as a 2D monolayer were analysed using a cell viability/SRB assay to monitor cell numbers at varying concentrations of TMZ. The results were normalised to a DMSO-treated control plate (as the TMZ drug is dissolved in DMSO) to account for any non-TMZ specific cell killing (Fig. 4).

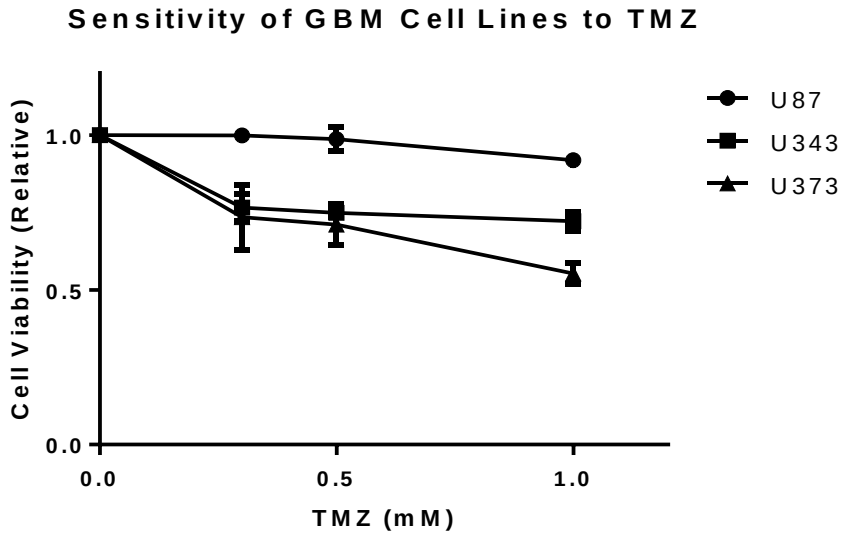


**Figure 4 – Varying sensitivity of U87, U343 and U373 to TMZ treatment**
Cells grown in a monolayer were treated with varying concentrations of TMZ and incubated for 72 hours. The cells were fixed and an SRB assay performed to measure cell viability. The results were normalised to cell count when no TMZ was added and are shown relative to the results from the treatment of an equal volume of DMSO. N=3, error bars indicate standard error of the mean.

The findings show varying levels of sensitivity to TMZ between the three cell types. U373/Mesenchymal cells were the most responsive to TMZ treatment, with U343/Classical cells also showing substantial cell death upon TMZ treatment. U87/Proneural cells were the most resistant to TMZ therapy. This indicates that each cell line possesses distinct characteristics and that TMZ has different efficacies per GBM subtype in vitro.

*3.3 GBM Cell Lines Can Form Monoclonal Spheroids*

Spheroids have been shown to be more representative of GBM tumours than 2D monolayer culture (De Witt Hamer et al., 2008). GBM cell lines engineered to endogenously express a fluorescent protein – U87-GFP, U343-YFP, and U373-RFP – were seeded onto agarose plates and cultured for three days to form spheroids. Following incubation with Hoescht stain (to label the nuclei) and immunofluorescent labelling of HIF1α, a protein marker of hypoxia, the spheroids were imaged using confocal microscopy (Fig. 5).

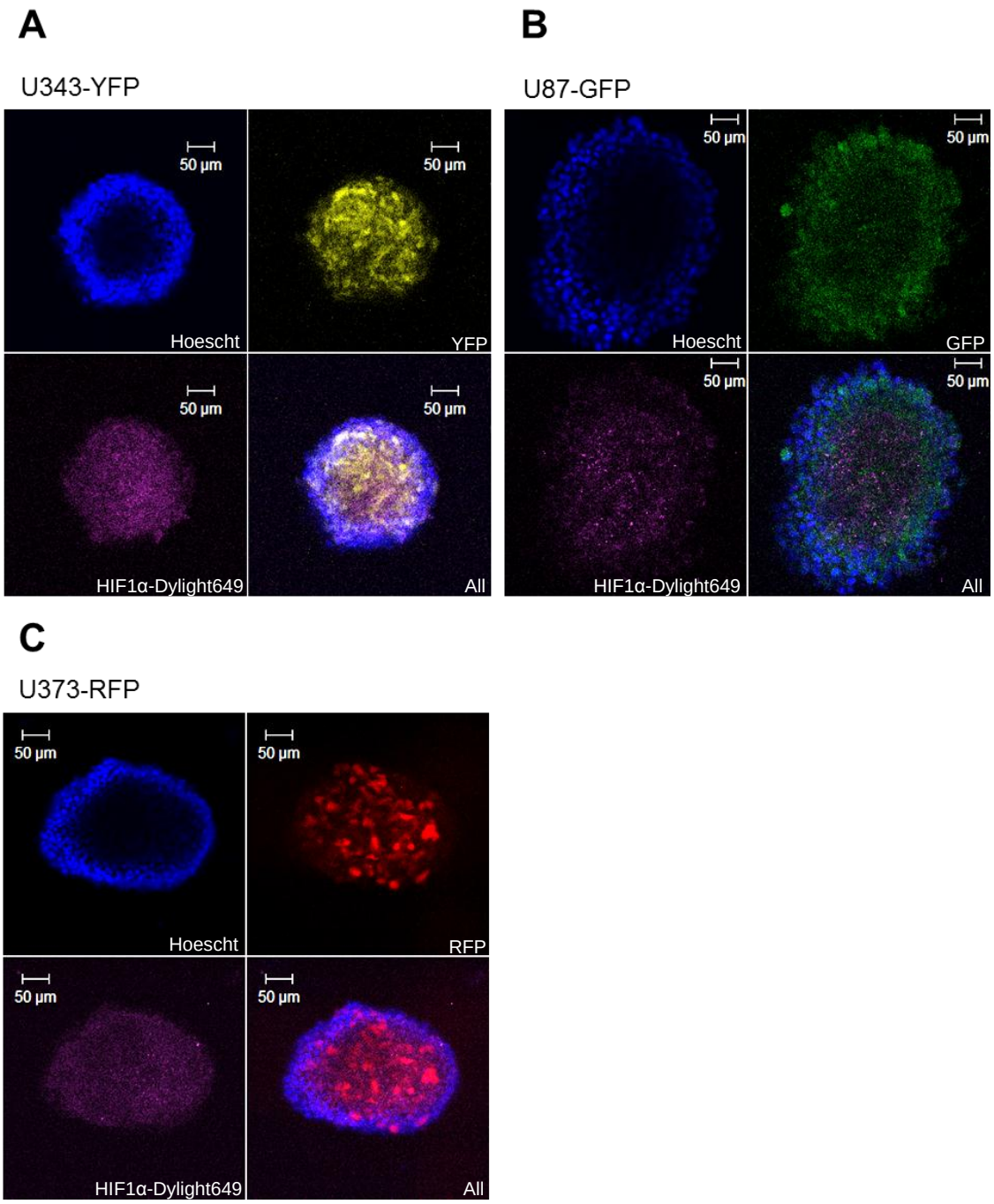


**Figure 5 – GBM cell lines can be cultured as spheroids**
U343-YFP (A), U87-GFP (B) or U373-RFP (C) cells were seeded onto individual agarose plates to form spheroids, then harvested and fixed after three days growth. The spheroids were permeablised and incubated with an antibody against HIF1α, followed by incubation with a secondary antibody tagged with a far-red dye (Dylight649), to indicate hypoxic regions. Hoescht stain was also added to label the nuclei. The spheroids were imaged using confocal microscopy at wavelengths appropriate for Hoescht (top left of each picture), the endogenous fluorescent protein (top right) and HIF1α-Dylight649 (bottom left), with the collective image displaying all three fluorescent signals at the bottom right of each picture.

The results show that each of the cell lines can spontaneously form multicellular spheroid structures. The Hoescht stain only labelled cells on the periphery of the spheroid. Replacement of Hoescht stain (a live cell stain) with DAPI (a fixed cell stain) showed no change in the coverage of the dye. It is possible that the solution could not penetrate into the centre of the spheroid. The endogenous fluorescence indicates cells are present throughout the spheroid in both U343 and U373 cultures, suggesting they form solid, tightly-packed structures. The GFP fluorescence of the U87 cells, however, is mainly focussed around the edges of the spheroid, with the centre showing a dimmer fluorescence that also has a less cellular appearance with fewer distinct shapes, suggesting the U87 spheroids are not solid. Immunofluorescence to see the localisation of HIF1α revealed a hypoxic environment in the core of each spheroid. Indeed, a distinction can be seen between the position of the outer cells, stained with Hoescht, and where the HIF1α far-red staining begins within the spheroid. The presence of oxygen gradients/hypoxia is consistent with previous studies that suggest spheroids are more representative of tumours than 2D cell culture and are, therefore, a better model to use in understanding GBM tumours. Interestingly, the HIF1α staining in the U87 spheroids is different, displaying more distinct spots of fluorescence compared to diffuse staining with the other two cell lines. The staining could be an artefact of antibody binding to cell debris in the necrotic core.

*3.4 Confocal Imaging Can be Improved Using Cells Sorted by FACS*

The previous images showed a poor fluorescent signal of the endogenous GFP in U87 cells, while only a small proportion of the U373 cells displayed a strong RFP signal. Therefore, these cell lines underwent a FACS procedure to select those cells with the strongest fluorescent signal. Confocal imaging of the sorted U87-GFP cells (Fig. 6) showed a substantial improvement in the GFP fluorescence and the images obtained. However, due to contamination during the FACS procedure, the U373-RFP cells were unable to be sorted and re-cultured, and the U87-GFP cells were eventually also lost to infection. Nevertheless, the images obtained show the benefits that sorting the fluorescently-labelled cells by FACS can bring to confocal microscopy imaging.

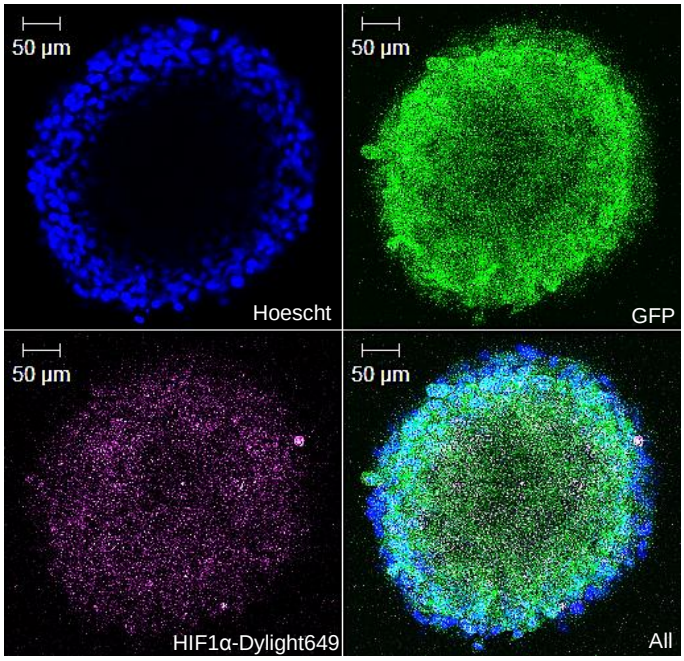


**Figure 6 – Sorting of U87-GFP cells using FACS improves confocal imaging**
U87-GFP cells were sorted using a FACS protocol to select those with the highest fluorescent signal, before culturing as spheroids. The spheroids were harvested on day 3 of growth, stained with Hoescht, and the HIF1α protein immunofluorescently labelled with a far-red dye, Dylight649. The spheroids were subsequently imaged using confocal microscopy, taking a z-section within the centre of the spheroid, to detect the Hoescht (top left), endogenous GFP (top right) and HIF1α-Dylight649 fluorescent signals (bottom left).

### *3.5 The Effects of TMZ Treatment on Monoclonal Spheroids*

To investigate the effect of chemotherapy on the cell lines in spheroid culture, monoclonal spheroids were treated with TMZ and imaged, along with a control DMSO-treated sample (Fig. 7). As confocal microscopy allows imaging of only a small number of spheroids, along with the added bias of selecting those of a suitable size or strong fluorescence, an overall range of the sizes of the spheroids in each sample was obtained to allow comparison between cell lines and conditions (Fig. 8).

The U343-YFP spheroids (Fig. 7a) showed no change in phenotype, as well as no significant change in volume. However, both the U373-RFP and U87-GFP spheroids displayed a change in morphology following TMZ treatment. The U373 spheroids (Fig. 7b) had decreased endogenous and immunofluorescent staining in the spheroid centre, suggesting they may become hollow with treatment. Despite this change in morphology, there was no overall change in size, suggesting low TMZ efficacy. On the other hand, the U87 spheroids (Fig. 7c) demonstrated an increase in spheroid cell density and a smaller necrotic core, with higher endogenous and HIF1α fluorescence towards the centre of the spheroid. There was also a change in volume. The TMZ-treated spheroids formed two populations, some that were indeed smaller than the control samples, indicating cell killing, but some significantly larger. The smaller necrotic core could allow the formation of larger, more stable spheroids. Thus, the three different GBM subtypes respond differently to chemotherapy.

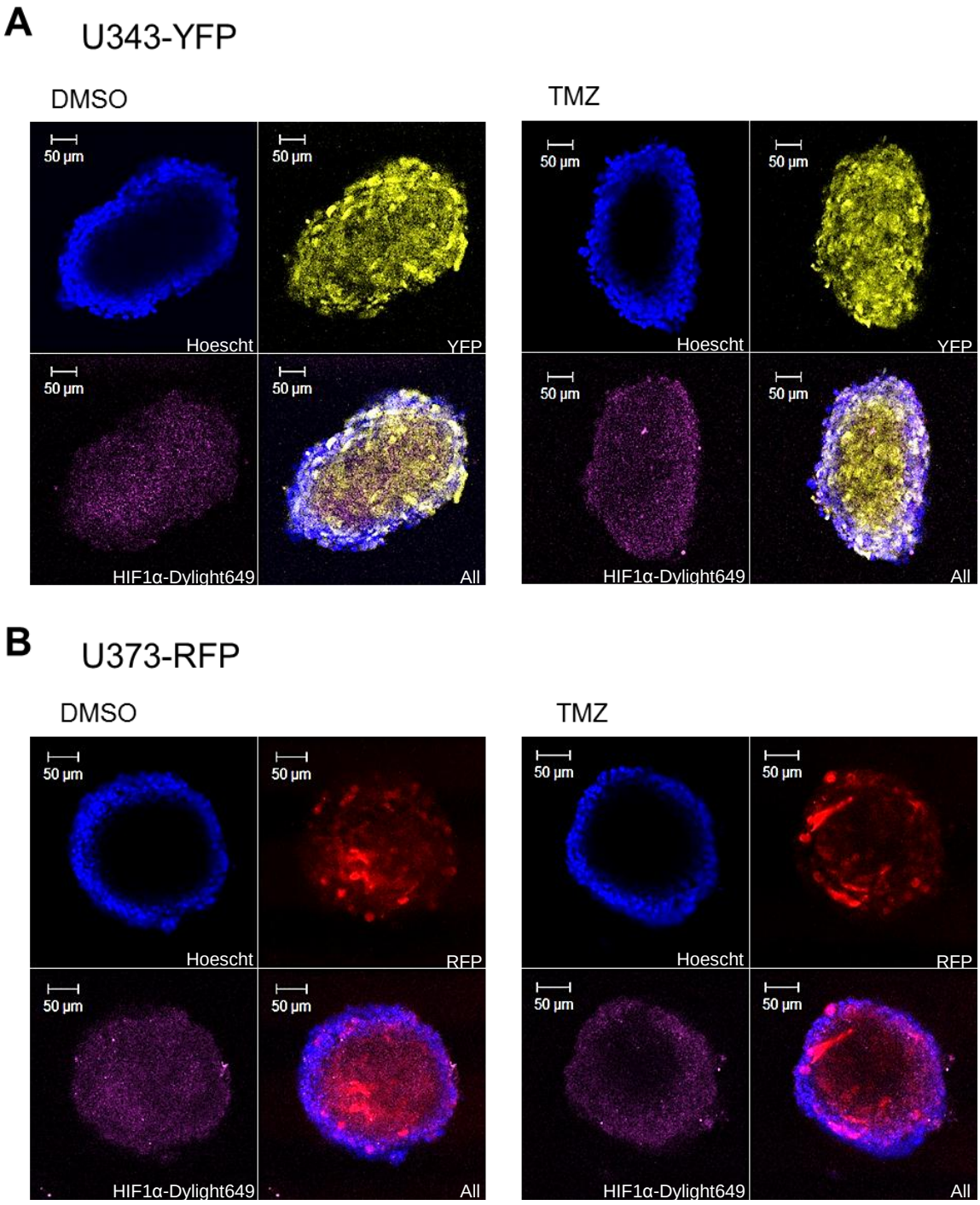
A
U343-YFP
DMSO
TMZ
50 µm
Hoescht
YFP
HIF1α-Dylight649
All
B
U373-RFP
DMSO
TMZ
50 µm
Hoescht
RFP
HIF1α-Dylight649
All

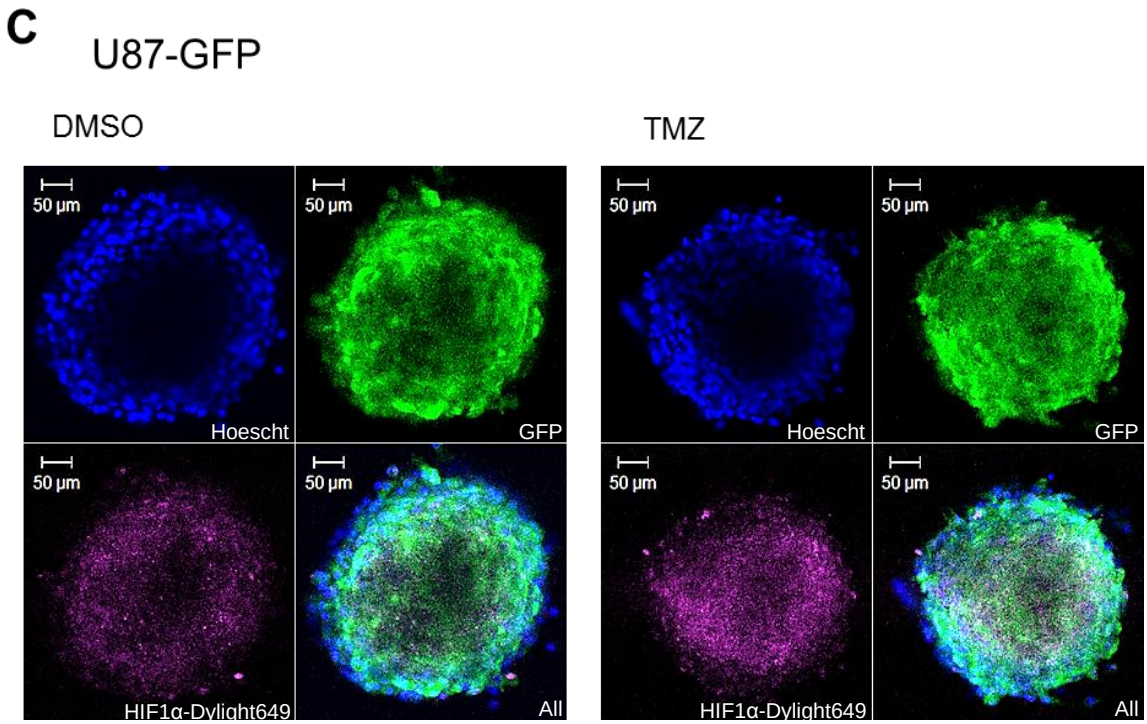


**Figure 7 – Response of spheroid cultures to TMZ treatment**
U343-YFP (A), U373-RFP (B) and U87-GFP (C) spheroids were cultured for 3 days, before treating with 1 mM TMZ (or an equal volume of DMSO) and incubating for a further 3 days. Spheroids were harvested, fixed and permeablised, and HIF1α immunofluorescently labelled with Dylight349 and the nuclei stained with Hoescht. Confocal microscopy was used to image the samples, taking a z-stack from near the centre of the spheroid, using wavelengths suitable to detect the fluorescence of Hoescht, endogenous fluorescent protein and HIF1α-Dylight649, as indicated.

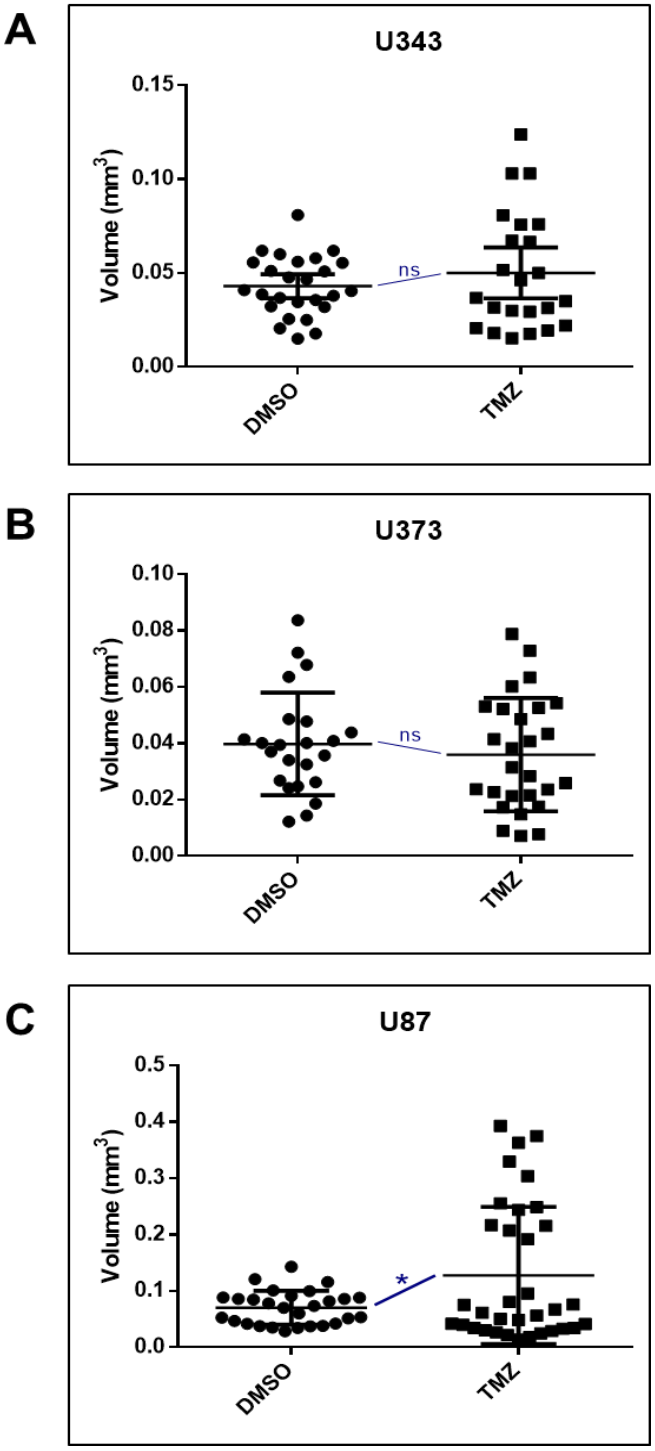


**Figure 8 – The effect of TMZ treatment on spheroid size**
**(A)** U343 spheroids were treated with 1 mM TMZ for 72 hours, or an equal volume of DMSO as a control. The resulting spheroids were imaged using an inverted light microscope and the images subsequently analysed using Image J software to estimate the spheroid volume (assuming a sphere shape). The mean is shown by the black line and the error bars represent the standard deviation. * – significant at $p<0.05$, calculated using an unpaired t test; ns – non-significant at $p<0.05$. (N=2) **(B)** and **(C)** As for (A) but using U373 and U87 spheroids, respectively.

*3.6 GBM Subtypes Have a Distinct Arrangement Within a Polyclonal Spheroid*

Next, U343-YFP, U373-RFP and U87-GFP cells were cultured together to form polyclonal spheroids. However, upon imaging, the GFP and YFP signals could not be distinguished due to the overlap between their emission spectra (Fig. 9a).

To allow the different colours in a polyclonal spheroid to be differentiated during confocal microscopy, 'unmixing' software was used. Spectra were first obtained for each of the fluorescent colours separately. Then, upon imaging of the polyclonal spheroids, the LSM unmixing software was used, with which the individual spectra were applied to the spheroid to separate and identify the various emission wavelengths (Fig. 9b).

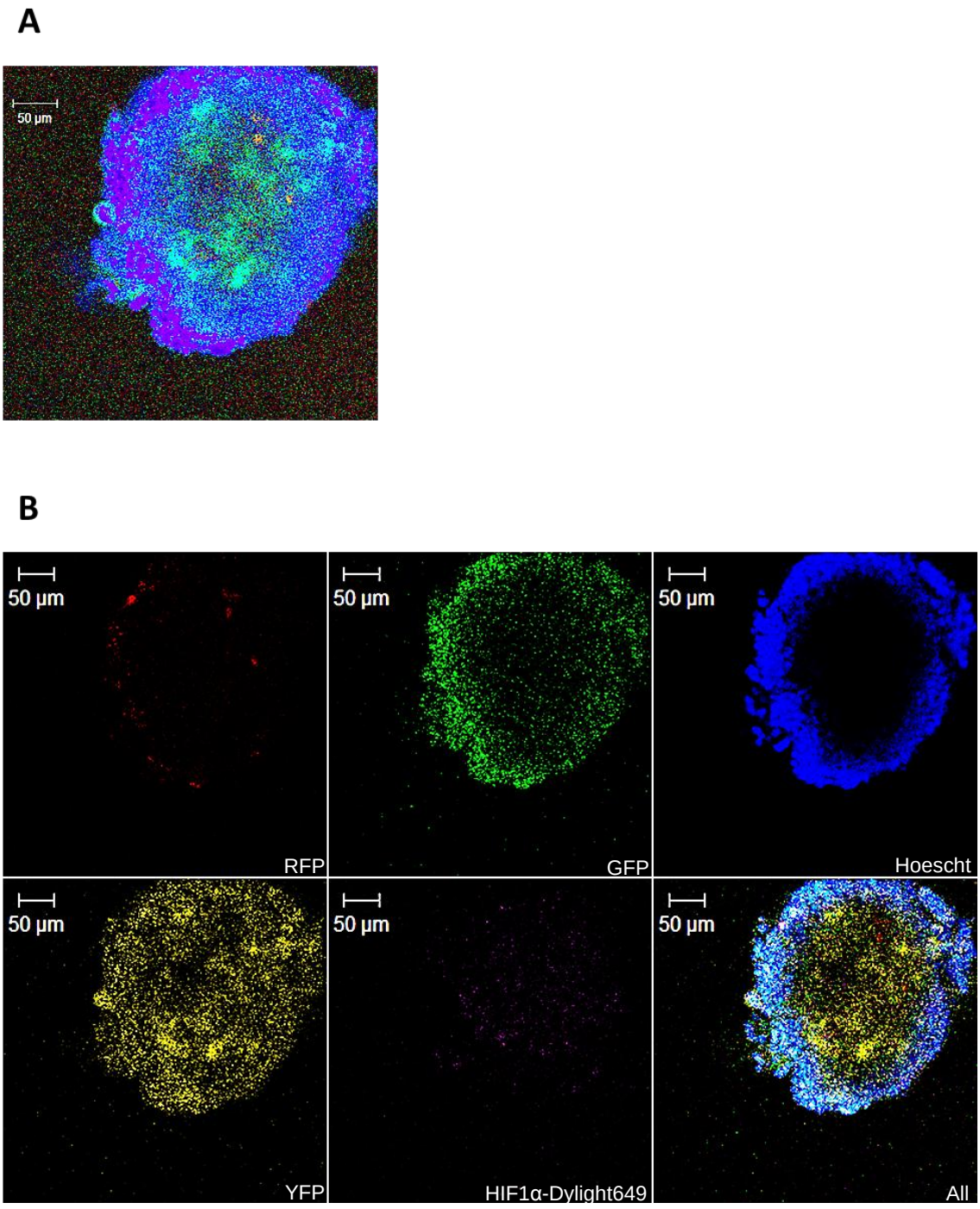


**Figure 9 – Arrangement of cell types in a polyclonal spheroid**
**(A)** U87-GFP, U343-YFP and U373-RFP cells were cultured together for 3 days to form spheroids. The spheroids were harvested, fixed and permeablised, before immunofluorescently labelled with far-red Dylight649 against the HIF1α protein. They were then imaged by confocal microscopy, with the resulting image shown. **(B)** The polyclonal spheroid images (A) were processed using LSM unmixing software to allow the different fluorescent colours to be distinguished from one another. The image of each individual fluorescent signal is shown (as labelled) as well as the collective signals in one image.

The results reveal that, rather than the different cell types displaying a random distribution throughout the spheroid, they instead form distinct populations. The U343-YFP cells were consistently found to pack tightly together through the centre of the spheroid, while the U87-GFP cells were found focussed at the periphery of the spheroid (in line with that seen in the U87 monoclonal spheroids). However, there still appears to be some overlap between these two signals. It was difficult to image the U373-RFP cells in the polyclonal spheroids due to their low intensity fluorescence, but upon dramatically increasing the RFP brightness in various samples, the results suggest they are more diffuse through the spheroid, with more variable positions. Thus, it may be the U343 and U87 cells that determine the structure and cell organisation of the spheroid. Furthermore, only low levels of HIF1α were seen in the polyclonal spheroids compared to the monoclonal spheroids, suggesting that the conditions within the spheroid core are not right for stabilisation of the HIF1α protein. Therefore, it may be the different subtypes arrange in the most beneficial organisation to give the least cellular stress.

### *3.7 The Impact of TMZ Treatment on Polyclonal Spheroids*

TMZ has been shown to affect the spheroids of the different cell lines in different ways. To further investigate the effects of chemotherapy on GBM tumours, polyclonal spheroids were treated with TMZ for 72 hours, before viewing any changes in spheroid morphology using confocal imaging and analysing volume change (Fig. 10).

**A**

DMSO

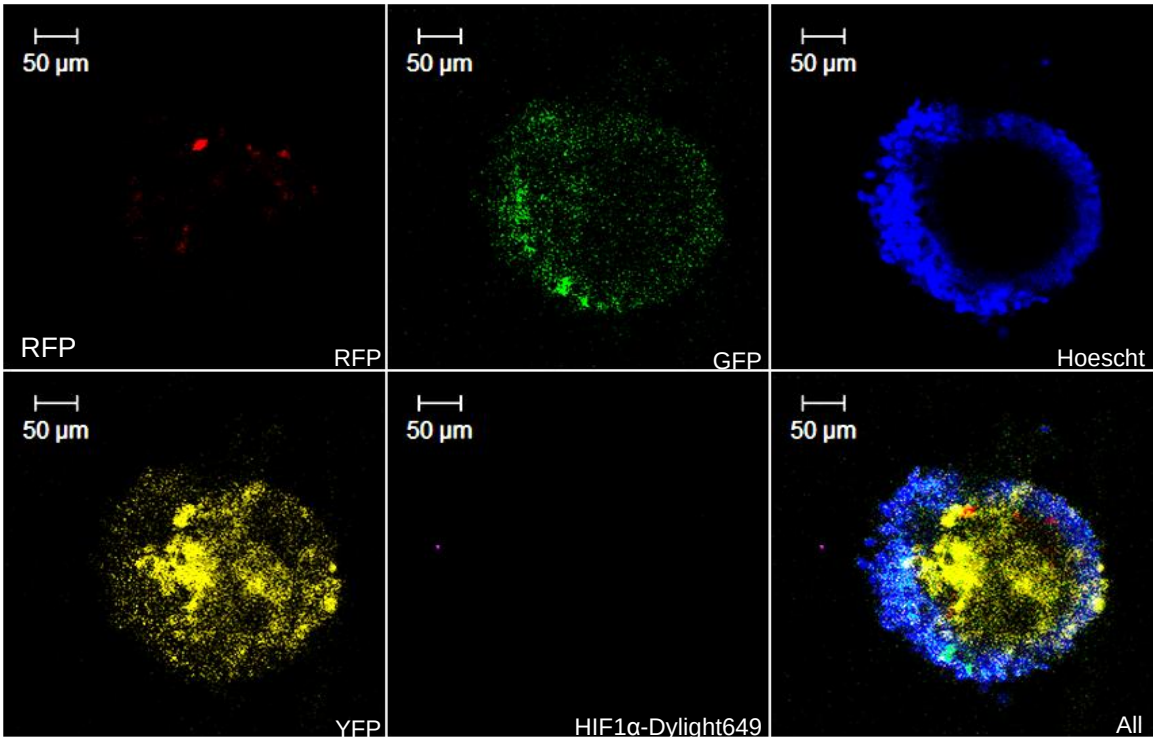
50 µm
RFP
RFP
50 µm
GFP
50 µm
Hoescht
50 µm
YFP
50 µm
HIF1α-Dylight649
50 µm
All

**B**

TMZ

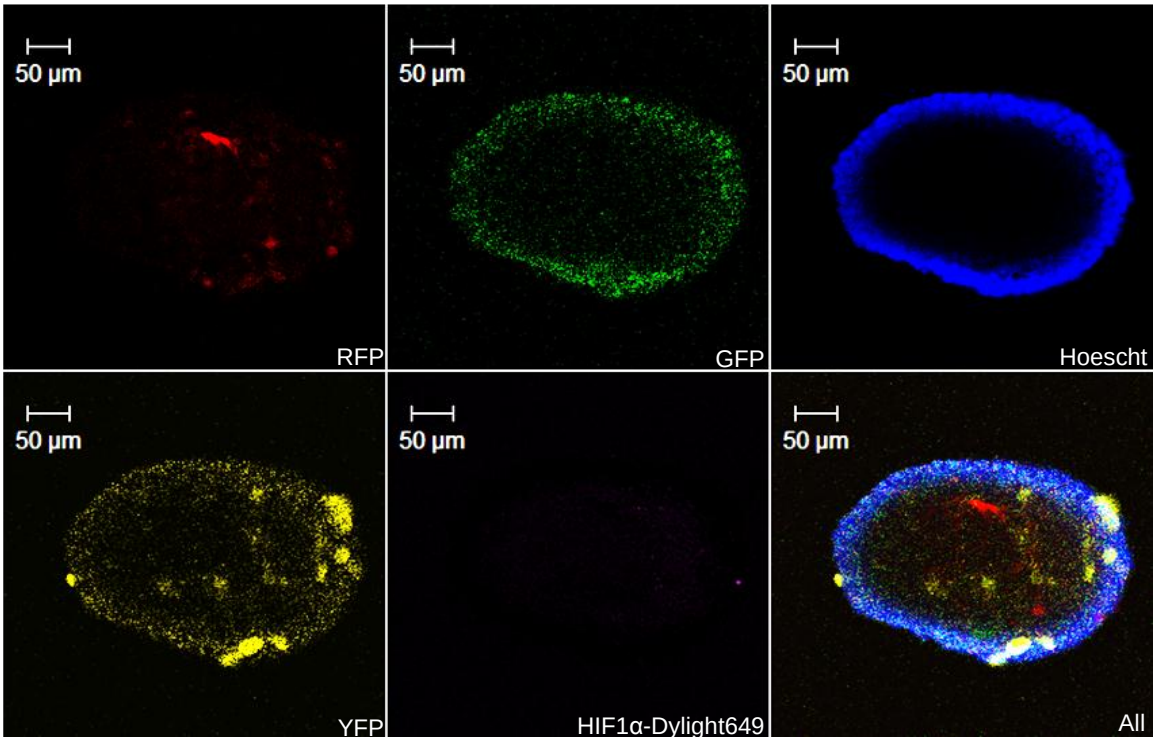
50 µm
RFP
50 µm
GFP
50 µm
Hoescht
50 µm
YFP
50 µm
HIF1α-Dylight649
50 µm
All

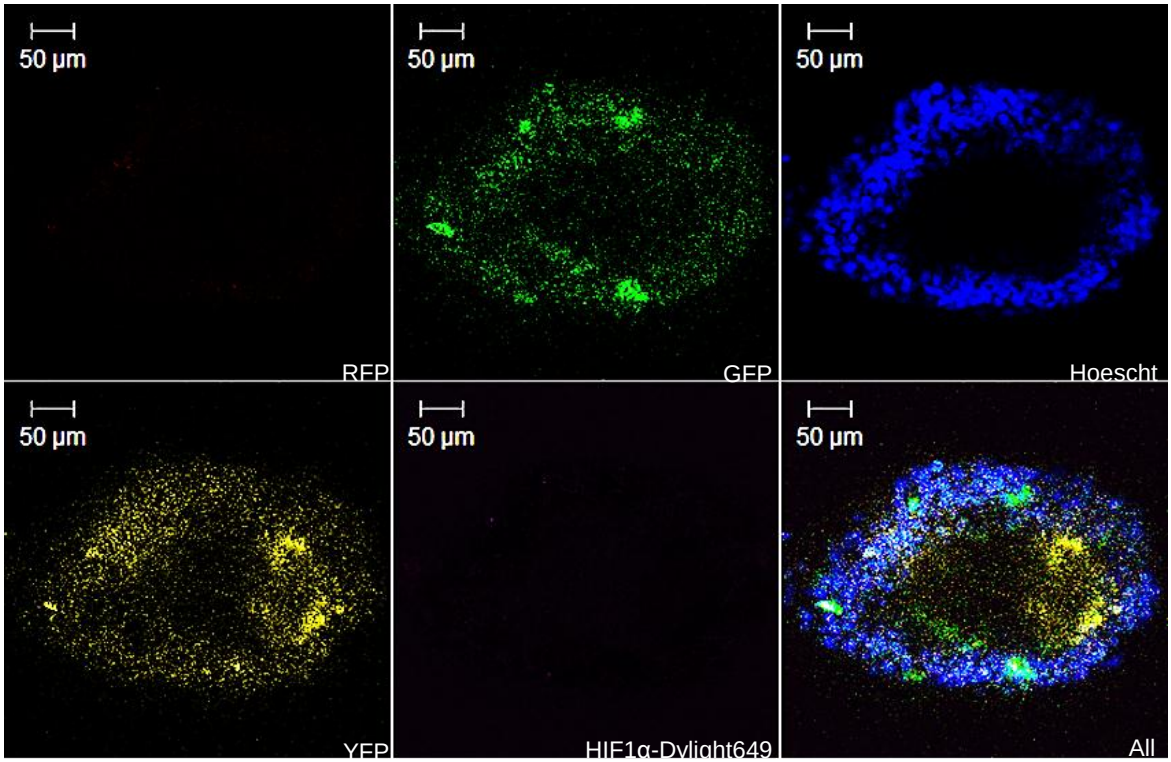
50 µm
RFP
50 µm
GFP
50 µm
Hoescht
50 µm
YFP
50 µm
HIF1α-Dylight649
50 µm
All

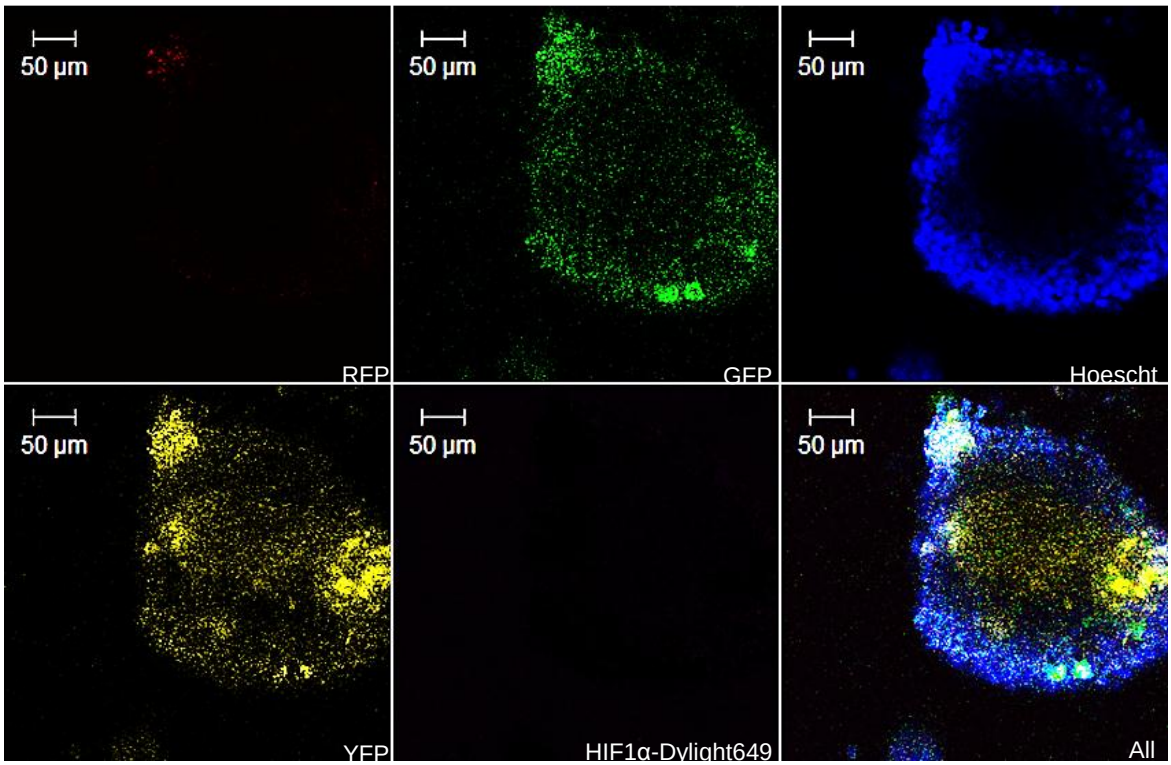
50 µm
RFP
50 µm
GFP
50 µm
Hoescht
50 µm
YFP
50 µm
HIF1α-Dylight649
50 µm
All

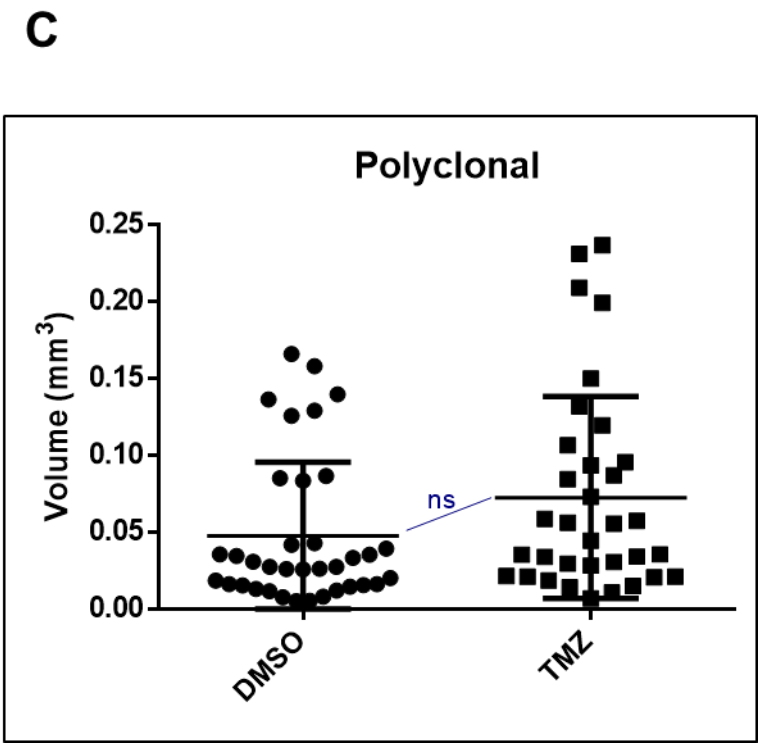


**Figure 10 – The effect of TMZ on polyclonal spheroids**
**(A)** U343-YFP, U373-RFP and U87-GFP cells were incubated together for 3 days to form polyclonal spheroids, before treating with DMSO for a further 72 hours. Spheroids were harvested, fixed and permeablised, followed by immunofluorescent staining of HIF1α with a far-red Dylight649 fluorescent dye. The samples were imaged using confocal microscopy and processed using LSM unmixing software to separate between the different colours. The images show: RFP - top right; GFP - top middle; Hoescht - top right; YFP - bottom left; Dylight649 - middle bottom, collective colours – bottom right. **(B)** As for (A), except treating the spheroids with 1 mM TMZ. **(C)** Polyclonal spheroids were treated with 1 mM TMZ or an equal volume of DMSO for 72 hours. The spheroids were imaged using an inverted light microscope and analysed using Image J software to enable estimation of spheroid volume (assuming a sphere shape).

The images show a change in cell organisation within the spheroid following TMZ treatment. Generally, while there is little change in U87-GFP positions, there is a decrease of U343-YFP in the spheroid core. This could be due to cell death leading to a larger necrotic core, or the U343-YFP cells moving towards the edges of the spheroid as they can no longer cope with the increased cellular stress, in

addition to the low nutrient and oxygen status in the spheroid centre. Again, it is difficult to visualise the U373-RFP cells due to the poor fluorescent signal. The analysis of spheroid volumes (Fig. 10C) revealed no significant change compared to DMSO-treated spheroids, showing that despite the change in phenotype, the drug has little overall effect on the spheroids.

### *3.8 EGFR Immunofluorescence of U343/Classical Cells*

Spectral overlap between the YFP and GFP fluorescence of U343 and U87, respectively, was shown to be a problem in imaging polyclonal spheroids due to difficulties in distinguishing between the two colours. Therefore, non-fluorescently labelled U343 could be used along with immunofluorescence staining of EGFR – the expression of which was shown to be only detectable in U343 cells (Fig. 3) – to instead label the U343 cells with Dylight649 far-red fluorescence and thus allow distinction between the three cell types in a single spheroid. To confirm that EGFR immunofluorescence is suitable for imaging and allows good coverage throughout the spheroid, it was first used with U343 monoclonal spheroids. To ensure there would be no cross-labelling of the other cell lines, the procedure was simultaneously performed with U87 and U373 monoclonal spheroids (Fig. 11).

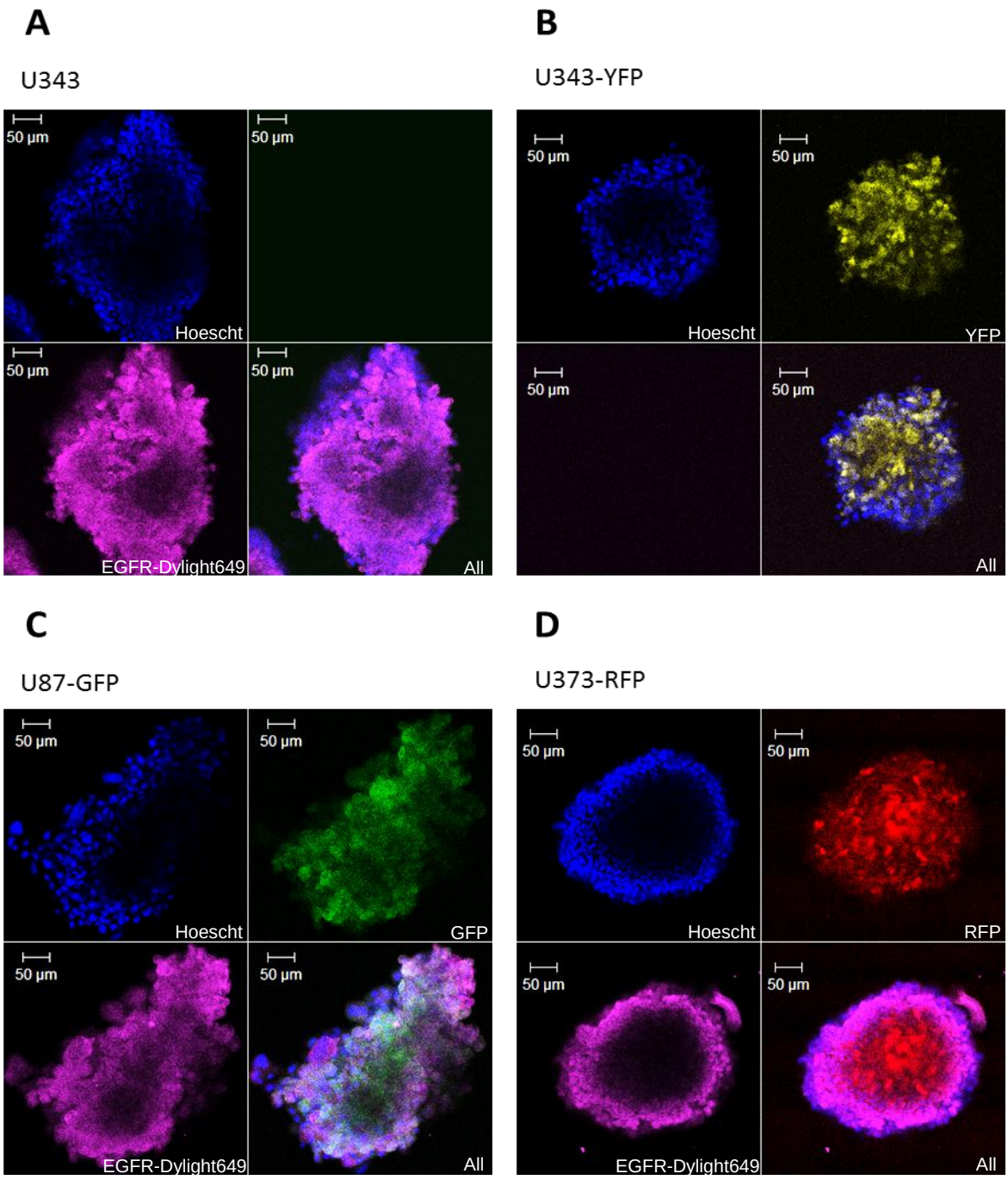


**Figure 11 – Immunofluorescence of U343 cells using an EGFR-reactive antibody shows cross-reactivity between the different strains.**
**(A)** U343 spheroids were harvested, fixed and immunofluorescence performed using an antibody specific for EGFR and a secondary antibody with a far-red tag (Dylight649) at 1:50 dilution. The spheroids were imaged using confocal microscopy. **(B)** U343-YFP spheroids were harvested, fixed and stained with Hoescht before imaging with confocal microscopy. **(C,D)** As for (A), except with U87-GFP and U373-RFP, respectively. The images show each fluorescent signal

The results show that labelling the U343 cells with EGFR immunofluorescence allows good coverage of the spheroids and a strong fluorescent signal (as compared to that seen with endogenous YFP [Fig. 11b]). However, staining of both the U87 and U373 spheroids was also observed, suggesting the EGFR antibody could also bind to these cell lines.

Next, as the cross-reactivity may have been due to high antibody concentrations, the immunofluorescence was repeated on U343 spheroids using varying dilutions of primary antibody to identify the lowest concentration of antibody allowing staining of the spheroids (Fig. 12). The confocal images still show strong fluorescence at 1:250 dilution, but there seems to be no further change at dilutions above 1:500. Therefore, the immunofluorescence was repeated at 1:250 dilution of EGFR antibody with all cell lines and imaged using confocal microscopy. Again, the Dylight659 fluorescence could be seen across all spheroid lines. This result was also obtained using non-fluorescent protein expressing cell lines (Fig. 13), suggesting that there was no interference from the fluorescent tag on antibody binding.

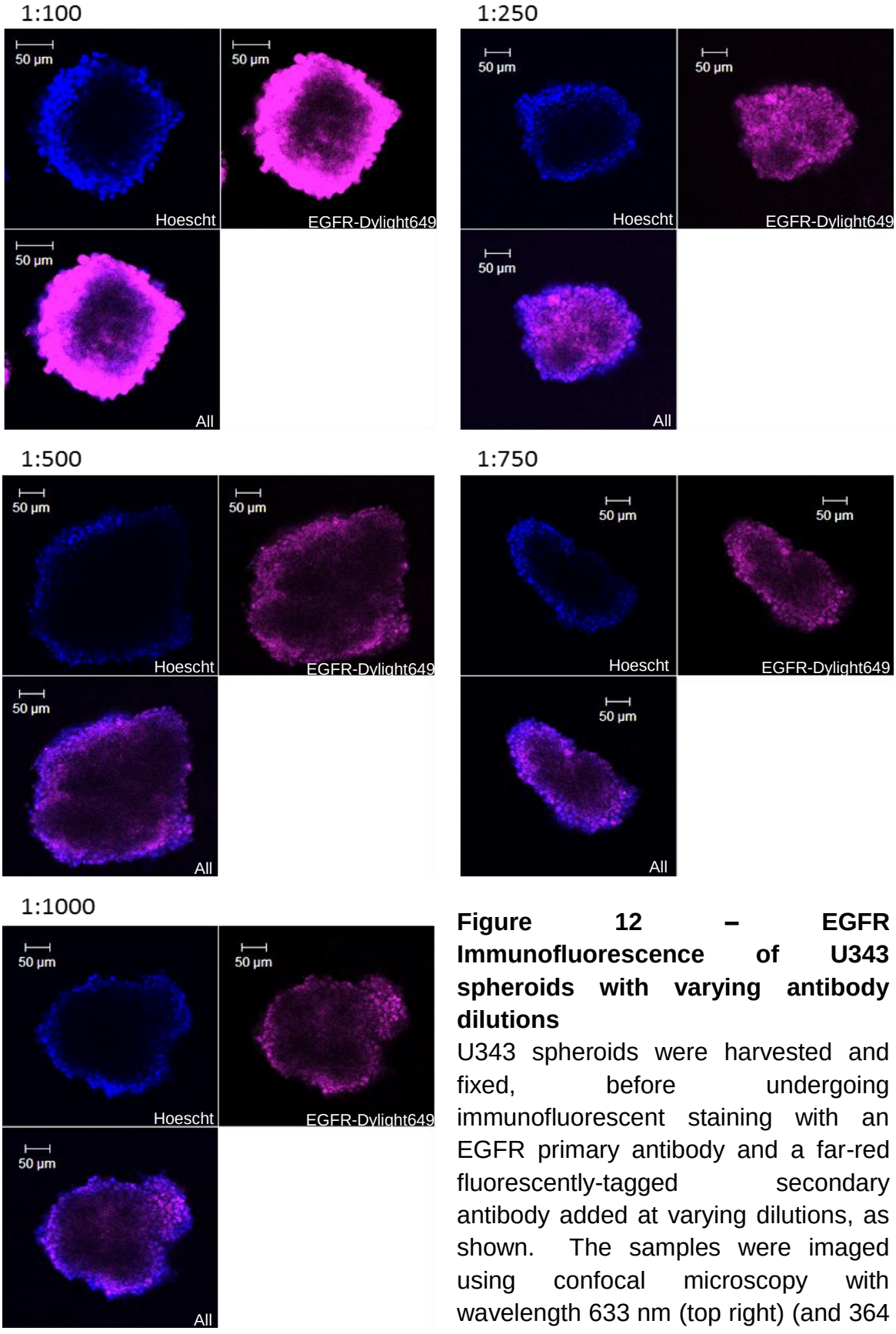


**Figure 12 – EGFR Immunofluorescence of U343 spheroids with varying antibody dilutions**

U343 spheroids were harvested and fixed, before undergoing immunofluorescent staining with an EGFR primary antibody and a far-red fluorescently-tagged secondary antibody added at varying dilutions, as shown. The samples were imaged using confocal microscopy with wavelength 633 nm (top right) (and 364 nm for Hoescht blue staining, top left).

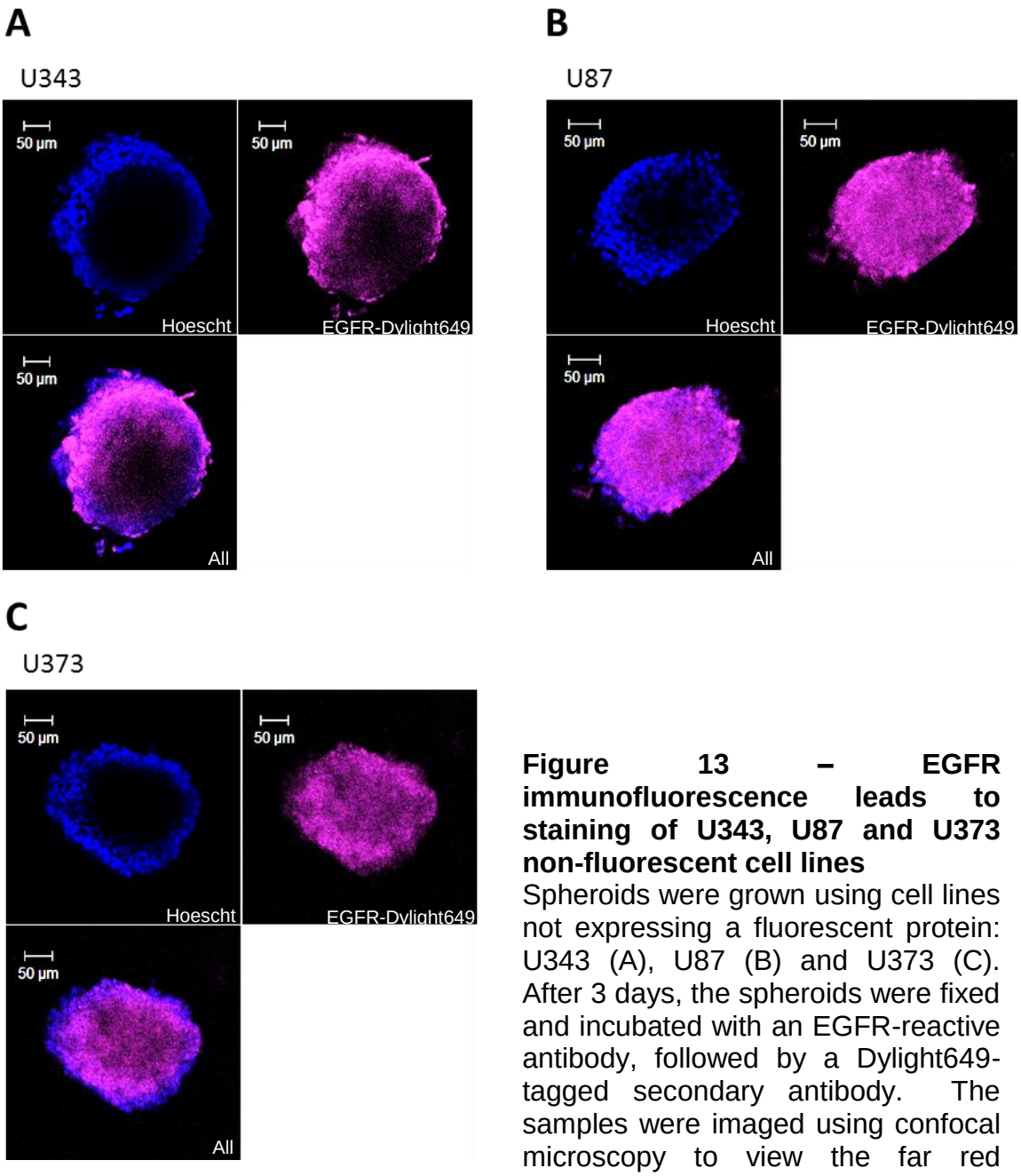


**Figure 13 – EGFR immunofluorescence leads to staining of U343, U87 and U373 non-fluorescent cell lines**
Spheroids were grown using cell lines not expressing a fluorescent protein: U343 (A), U87 (B) and U373 (C). After 3 days, the spheroids were fixed and incubated with an EGFR-reactive antibody, followed by a Dylight649-tagged secondary antibody. The samples were imaged using confocal microscopy to view the far red fluorescent signal (Dylight649, top right) and Hoescht (top left).

As it is possible that the expression of growth factor receptors is altered in 3D culture, a Western blot was performed using cells harvested from a spheroid culture and the levels of EGFR in each cell line measured (Fig. 14).

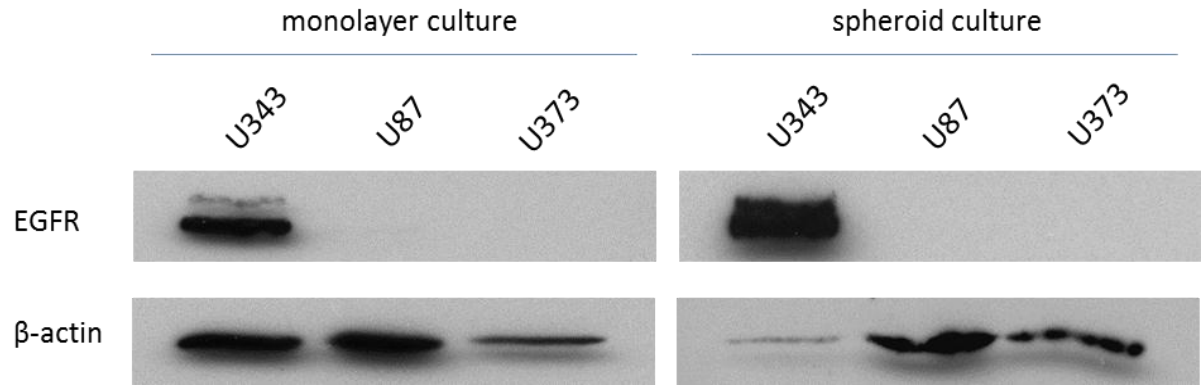


**Figure 14 – EGFR protein levels are maintained in spheroid culture**
U343, U87 and U373 monoclonal spheroids were cultured for 3 days, before harvesting, cell lysing and measuring the protein concentrations. A Western blot was performed with the three samples and the levels of EGFR measured compared to samples obtained from a monolayer culture. β-actin was used as a loading control.

The Western blot shows that EGFR protein levels in spheroid culture are consistent with those from 2D monolayers, as EGFR can only be detected in U343 cells. Therefore, it was likely that antibody non-specificity was causing the staining to occur on all cell type spheroids. The experiment was repeated using a different EGFR-reactive antibody (Fig. 15).

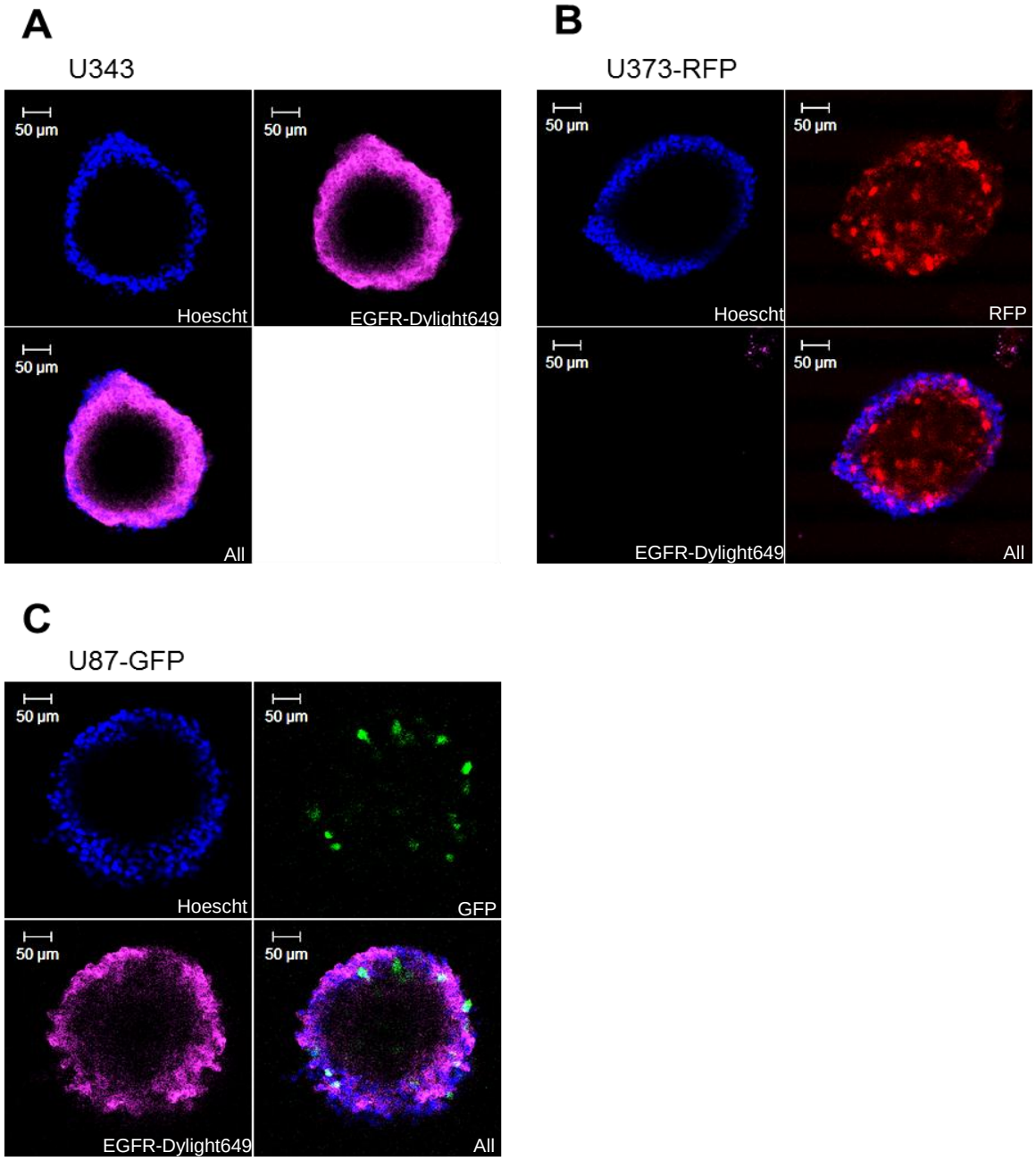


**Figure 15 – A new EGFR antibody still demonstrates cross-reactivity between cell lines**
**(A)** U343 cells were cultured for 3 days as spheroids, before fixing and permeablising. EGFR (Cell Signalling primary antibody) immunofluorescence, using a far-red Dylight649-tagged secondary antibody, was then used to visualise the cells using confocal microscopy. **(B,C)** As for (A), but using U373-RFP and U87-GFP cell lines, respectively. The images show the individual fluorescent colours, plus the collective, as indicated.

The images of the U343 immunofluorescence were promising, suggesting higher specificity as distinct cell outlines could be seen (as expected for reactivity to a cell surface receptor), but they also showed poor permeability of the antibody. Accordingly, no EGFR immunofluorescence was detected for the U373-RFP spheroids. However, a strong far-red fluorescent signal was seen in the U87-GFP spheroids. As Western blotting showed EGFR expression in U343 spheroids specifically, it suggests again the antibody is non-specific and cross-reacting with another molecule present on the surface U87, but not U373 cells. Use of a third EGFR-reactive antibody led to immunofluorescence of all three cell lines once again. Therefore, further optimisation would be required to use immunofluorescence to overcome the problem of GFP/YFP spectral overlap.

In conclusion, spheroid culture of GBM cells lines provides a more representative model of a GBM tumour than 2D monolayers, as indicated by the presence of hypoxia and altered responses to therapy. Polyclonal spheroids provided insight into the arrangement of the different GBM subtypes within a tumour, each showing preference for particular locations within the spheroid. The distinct subtype organisation is also affected by TMZ treatment, highlighting a potential mechanism of TMZ action. However, more work is required to obtain reliable images of the polyclonal spheroids without the issue of spectral overlap.

# 4. **DISCUSSION**

The aim of the present study was to develop a new model of GBM using spheroid culture of different GBM cells lines, which can represent the different subtypes found in a GBM tumour. This model was then used to analyse the interaction between the different subtypes and observe the effects of TMZ chemotherapy. A Western blot was used to confirm the cell lines could be used to represent the specific subtypes by looking at the expression of the signature proteins EGFR, NF1 and IDH1 R132H (Fig. 3). While the U87 and U373 cells lines were shown to be representative of Proneural and Mesenchymal subtypes, respectively, U343 cells were shown to have both an NF1 deletion (characteristic of Mesenchymal) and EGFR overexpression (characteristic of Classical). This challenges the reliability of the use of the U343 cells to represent the Classical subtype of GBM. Furthermore, the use of the expression of just three proteins to distinguish between the subtypes is an oversimplification. A number of genetic alterations have been shown to be characteristic of the individual subtypes (Fig. 2) which could additionally be considered when selecting the most appropriate cell lines for this study. Epigenetics is also well-known to influence the phenotype of cells and recently, that of GBM subtypes specifically. G-CIMP methylation, for example, is correlated with the Proneural subtype and is involved in conferring a survival advantage (Brennan et al., 2013), therefore epigenetic status of the cell line can also influence how well their behaviour exemplifies the corresponding subtype. Clark et al., 2010, found limited similarity between the U87 cell line and primary GBM samples, while 2D culture has been shown to cause genetic changes from primary samples (De Witt Hamer et al., 2008). This calls into question the use of

monolayer-cultured cell lines to develop a physiologically-relevant GBM model. Potentially, primary cell lines could be cultured as spheroids, providing a better representation of GBM and allowing the genetic modifications to be maintained.

Imaging of the fluorescently-labelled GBM cell lines cultured as a polyclonal spheroid revealed a specific organisation of the different cell lines (Fig. 9). U343-YFP cells were consistently found to pack tightly in the spheroid core, while U373-RFP spheroids seemed to be more diffuse through the spheroid. U87-GFP cells, on the other hand, were concentrated around the edges of the spheroid. These localisations are consistent with those seen for the monoclonal spheroids, in which U343-YFP and U373-RFP cells formed solid structures, but U87-GFP spheroids appeared more hollow. This suggests that the cell lines each have preferences for the different conditions experienced throughout the spheroid. U343-YFP cells seem to be highly resistant to hypoxia and nutrient deprivation and so are positioned in the spheroid core. U373-RFP cells similarly seem to be resistant to such stress, but do not have a preference for position in the spheroid. U87-GFP cells are typically located at the spheroid periphery. IDH1 mutation has been linked to hypoxia in two conflicting theories. The first suggests that mutation of IDH1 leads to lower levels of its catalytic product α-ketoglutarate, which normally promotes degradation of the HIF1α protein, thus leading to increased HIF1α in the cell and a ‘pseudohypoxic’ phenotype (Zhao et al., 2009). The second theory states that the IDH1 mutant protein gains the ability to produce R-2-hydroxyglutarate, which stimulates HIF1α degradation, therefore leading to lower HIF1α levels. In support, the HIF signature was seen to be diminished in

Proneural tumours in the TCGA data (Koivunen et al., 2012). This suggests that Proneural cells may not be able to adapt to hypoxic conditions, supporting the results of the present study and explaining their preference for the spheroid edges. Therefore, these results suggest that GBM subtypes form distinct populations within a tumour, with organisation based on minimising the cellular stress of each subtype.

However, the polyclonal spheroids in this experiment did not contain any Neural subtype cells. Although such cell lines would be difficult to obtain due to the lack of defining genetic alterations, their presence may affect the cellular organisation within the tumour. Moreover, despite using software to differentiate between the various emission spectra in the polyclonal spheroid, considerable overlap can still be seen between the GFP and YFP fluorescence. This questions the reliability of the results seen here. Therefore, the next steps in this study would be to reduce spectral overlap between the different cell lines. Attempts to replace the YFP signals of the U343 cell line with far-red EGFR immunofluorescence were unsuccessful due to antibody non-specificity. The use of one EGFR antibody (Fig. 15) caused immunofluorescent staining of U343 cells, overexpressing EGFR, but not U373 cells, showing this method has potential. However, staining could also be seen with U87 cells. This suggests that the U87 cell line expresses a surface receptor, not present on the U373 cells, that possesses structural similarity to EGFR. It is possible that this molecule is in the PDGFR family, the expression of which is known to be up-regulated in Proneural cells and is associated with stem-like cells, explaining its expression in spheroid culture. A microarray of the three

cell lines could be performed to determine the molecule causing the cross-staining. Another EGFR-specific antibody could be tested for use in this method.

However, the next step would be to re-engineer the cell lines to express a different coloured fluorescent tag – specifically change the U343-YFP label to endogenously express a protein with an emission spectra distant from that of GFP and RFP, e.g. BFP. The U373-RFP fluorescence has also demonstrated a poor signal, making it difficult to visualise the cells, particularly in the polyclonal spheroid. FACS could be repeated to select the cells expressing the RFP with the strongest fluorescence or the U373 cells could be engineered to express a different, possibly brighter, tag such as mCherry. The consistent loss of endogenously expressed fluorescent protein from these cells has also been an issue. The new transfections could therefore be performed using lentiviral vectors, which show high frequency transduction of dividing and non-dividing cells, resulting in stable/long-term integration into the genome (Naldini et al., 1996).

The sensitivity of each of the cell lines to TMZ was investigated. Spheroids have been shown to display a significant reduction in drug sensitivity compared to 2D culture (Durand and Olive, 2001). Concordantly, both the U373 and U343 cell lines showed substantial cell death upon TMZ treatment in 2D culture (Fig. 4), but showed no significant change in spheroid volume in monoclonal 3D culture (despite some change in morphology in the U373 spheroids) (Fig. 7/8), suggesting increased resistance to therapy in spheroid culture. The U87 cells exhibited a

change in morphology, with a smaller necrotic core, plus changes in volume size. Some spheroids appeared smaller, suggesting cell killing, while others were significantly larger than the control. This indicates cells in a spheroid behave differently to a monolayer and are a better model to study drug efficacy. The increased size of some spheroids could be due to the smaller necrotic core allowing the formation of larger, more stable structures. It could also be that the cell size has increased, as the TMZ may affect cell division. This could be further studied by increasing the magnification when imaging the treated cells, or using flow cytometry of disaggregated spheroids to measure differences in cell size or DNA content. Polyclonal spheroids also displayed no significant change in volume, suggesting low treatment efficacy, but there was a change in morphology (Fig. 10), with a decrease in cells in the core perhaps due to killing of the cells already under increased cellular stress due to nutrient/oxygen deficiency.

However, the current treatment given to patients involves concomitant chemo- and radiotherapy, while TMZ given as a single agent has limited benefits (Stupp et al., 2001). The next steps would therefore be to study the effects of both radiation and TMZ therapy on spheroid phenotype and size. The results could then be compared to the treatment efficacy for each subtype from primary samples by Verhaak et al. (2010) to assess how representable the cell lines are of their corresponding GBM subtype. Cell viability in the spheroids could also be analysed in the treated vs. control samples. Immunofluorescent staining of proliferative (e.g. Ki67) and apoptotic (e.g. caspases) markers could be used (Loessner et al., 2013), followed by confocal microscopy, to indicate cell viability in different regions

of the spheroid upon treatment. Alternatively, the APH assay, based on levels of cytosolic acid phosphatase, could be used to indicate cytotoxicity in spheroid cultures (as described in Mikhail et al., 2013).

The measurement of spheroid volumes highlighted the variability of sizes (and shapes) of the spheroids within each sample and between experiments. This also added bias to the confocal microscopy, as only those spheroids of an appropriate size, fitting into the field of vision, were imaged. Recently, new methods of spheroid growth have been developed, which allow the formation of spheroids with a uniform size and shape. They involve using microwells, coated with non-adherent substances, to restrict the spheroids to defined sizes, while microfluidics allow continued contact with growth medium (Hirschhauser et al., 2010). Another method adapts the 'hanging drop' procedure of spheroid culture, in which cells are suspended in drops of medium. The cells are confined by the diameter of the plateau on the bottom surface, giving consistent geometry, plus access holes in the hanging drop plate allow easy access, e.g. to change media or add drugs (Mehta et al., 2012). These methods are both more high-throughput and would allow higher reproducibility between experiments for future work in this study.

In conclusion, this study used a spheroid model to study the polyclonal nature of GBM. The results showed distinct populations of the different subtypes are formed within a single spheroid that appear to arrange in a way most beneficial for tumour survival. The presence of nutrient gradients, hypoxia and a necrotic core,

as well as an increased resistance to chemotherapy, suggests that spheroids are a better model of GBM tumours than using 2D monolayer cell lines. However, it is unlikely the findings can be applied in vivo. There are a number of other factors that influence the in vivo situation, for example drug delivery is different, rather having to pass through blood vessel walls to reach the tumour site. Cooper et al., 2012, suggested that the microenvironment is related to the specific gene expression patterns of the subtypes, which would not be comparable in spheroids in vitro. The use of engineered cell lines to represent the subtypes also questions the applicability of the results. This highlights the importance of recently developed mouse models of GBM, which have been engineered to develop the same genetic aberrations and allow the study of their relevance to gliomagenesis (Huse and Holland, 2009). Thus, although spheroids are a simplified model of GBM, their use is still an important step in model design, bridging the gap between in vivo and monolayer culture.

# 5. REFERENCES


Agnihotri, S., Burrell, K. E., Wolf, A., Jalali, S., Hawkins, C., Rutka, J. T., et al. (2013). Glioblastoma, a brief review of history, molecular genetics, animal models and novel therapeutic strategies. *Arch.Immunol.Ther.Exp.(Warsz), 61*(1), 25-41.

Brennan, C., Momota, H., Hambardzumyan, D., Ozawa, T., Tandon, A., Pedraza, A., et al. (2009). Glioblastoma subclasses can be defined by activity among signal transduction pathways and associated genomic alterations. *PLoS One, 4*(11), e7752.

Brennan, C. W., Verhaak, R. G., McKenna, A., Campos, B., Noushmehr, H., Salama, S. R., et al. (2013). The somatic genomic landscape of glioblastoma. *Cell, 155*(2), 462-477.

Cancer Genome Atlas Research Network. (2008). Comprehensive genomic characterization defines human glioblastoma genes and core pathways. *Nature, 455*(7216), 1061-1068.

Chen, J., McKay, R. M., & Parada, L. F. (2012). Malignant glioma: Lessons from genomics, mouse models, and stem cells. *Cell, 149*(1), 36-47.

Clark, M. J., Homer, N., O'Connor, B. D., Chen, Z., Eskin, A., Lee, H., et al. (2010). U87MG decoded: The genomic sequence of a cytogenetically aberrant human cancer cell line. *PLoS Genet., 6*(1), e1000832.

De Witt Hamer, P. C., Van Tilborg, A. A., Eijk, P. P., Sminia, P., Troost, D., Van Noorden, C. J., et al. (2008). The genomic profile of human malignant glioma is altered early in primary cell culture and preserved in spheroids. *Oncogene, 27*(14), 2091-2096.

Dunn, G. P., Rinne, M. L., Wykosky, J., Genovese, G., Quayle, S. N., Dunn, I. F., et al. (2012). Emerging insights into the molecular and cellular basis of glioblastoma. *Genes Dev., 26*(8), 756-784.

Durand, R. E., & Olive, P. L. (2001). Resistance of tumor cells to chemo- and radiotherapy modulated by the three-dimensional architecture of solid tumors and spheroids. *Methods Cell Biol., 64*, 211-233.

Elliott, N. T., & Yuan, F. (2011). A review of three-dimensional in vitro tissue models for drug discovery and transport studies. *J.Pharm.Sci., 100*(1), 59-74.

Freije, W. A., Castro-Vargas, F. E., Fang, Z., Horvath, S., Cloughesy, T., Liau, L. M., et al. (2004). Gene expression profiling of gliomas strongly predicts survival. *Cancer Res., 64*(18), 6503-6510.

Furnari, F. B., Fenton, T., Bachoo, R. M., Mukasa, A., Stommel, J. M., Stegh, A., et al. (2007). Malignant astrocytic glioma: Genetics, biology, and paths to treatment. *Genes Dev., 21*(21), 2683-2710.

Hirschhaeuser, F., Menne, H., Dittfeld, C., West, J., Mueller-Klieser, W., & Kunz-Schughart, L. A. (2010). Multicellular tumor spheroids: An underestimated tool is catching up again. *J.Biotechnol., 148*(1), 3-15.

Hodgson, J. G., Yeh, R. F., Ray, A., Wang, N. J., Smirnov, I., Yu, M., et al. (2009). Comparative analyses of gene copy number and mRNA expression in glioblastoma multiforme tumors and xenografts. *Neuro Oncol., 11*(5), 477-487.

Huse, J. T., & Holland, E. C. (2009). Genetically engineered mouse models of brain cancer and the promise of preclinical testing. *Brain Pathol., 19*(1), 132-143.

Huse, J. T., Phillips, H. S., & Brennan, C. W. (2011). Molecular subclassification of diffuse gliomas: Seeing order in the chaos. *Glia, 59*(8), 1190-1199.

Ishii, N., Maier, D., Merlo, A., Tada, M., Sawamura, Y., Diserens, A., et al. (1999). Frequent co-alterations of TP53, p16/CDKN2A, p14ARF, PTEN tumor suppressor genes in human glioma cell lines.*9*(3), 469-479.

Koivunen, P., Lee, S., Duncan, C. G., Lopez, G., Lu, G., Ramkissoon, S., et al. (2012). Transformation by the (R)-enantiomer of 2-hydroxyglutarate linked to EGLN activation. *Nature, 483*(7390), 484-488.

Le Mercier, M., Hastir, D., Moles Lopez, X., De Neve, N., Maris, C., Trepant, A. L., et al. (2012). A simplified approach for the molecular classification of glioblastomas. *PLoS One, 7*(9), e45475.

Lee, J., Kotliarova, S., Kotliarov, Y., Li, A., Su, Q., Donin, N. M., et al. (2006). Tumor stem cells derived from glioblastomas cultured in bFGF and EGF more closely mirror the phenotype and genotype of primary tumors than do serum-cultured cell lines.*9*(5), 391-403.

Liang, Y., Diehn, M., Watson, N., Bollen, A. W., Aldape, K. D., Nicholas, M. K., et al. (2005). Gene expression profiling reveals molecularly and clinically distinct subtypes of glioblastoma multiforme. *Proceedings of the National Academy of Sciences of the United States of America, 102*(16), 5814-5819.

Loessner, D., Flegg, J. A., Byrne, H. M., Clements, J. A., & Hutmacher, D. W. (2013). Growth of confined cancer spheroids: A combined experimental and mathematical modelling approach. *Integr.Biol., 5*(3), 597-605.

Loessner, D., Little, J. P., Pettet, G. J., & Hutmacher, D. W. (2013). A multiscale road map of cancer spheroids--incorporating experimental and mathematical modelling to understand cancer progression. *J.Cell.Sci., 126*(Pt 13), 2761-2771.

Louis, D. N., Ohgaki, H., Wiestler, O. D., Cavenee, W. K., Burger, P. C., Jouvet, A., et al. (2007). The 2007 WHO classification of tumours of the central nervous system. *Acta Neuropathol., 114*(2), 97-109.

Maher, E. A., Brennan, C., Wen, P. Y., Durso, L., Ligon, K. L., Richardson, A., et al. (2006). Marked genomic differences characterize primary and secondary glioblastoma subtypes and identify two distinct molecular and clinical secondary glioblastoma entities. *Cancer Res., 66*(23), 11502-11513.

Mehta, G., Hsiao, A. Y., Ingram, M., Luker, G. D., & Takayama, S. (2012). Opportunities and challenges for use of tumor spheroids as models to test drug delivery and efficacy. *J.Control.Release, 164*(2), 192-204.

Mikhail, A. S., Eetezadi, S., & Allen, C. (2013). Multicellular tumor spheroids for evaluation of cytotoxicity and tumor growth inhibitory effects of nanomedicines *in vitro*: A comparison of docetaxel-loaded block copolymer micelles and taxotere┬«. *Plos One, 8*(4), e62630.

Mrugala, M. M. (2013). Advances and challenges in the treatment of glioblastoma: A clinician's perspective. *Discov.Med., 15*(83), 221-230.

Naldini, L., Blomer, U., Gallay, P., Ory, D., Mulligan, R., Gage, F. H., et al. (1996). In vivo gene delivery and stable transduction of nondividing cells by a lentiviral vector. *Science, 272*(5259), 263-267.

Nobusawa, S., Lachuer, J., Wierinckx, A., Kim, Y. H., Huang, J., Legras, C., et al. (2010). Intratumoral patterns of genomic imbalance in glioblastomas. *Brain Pathol., 20*(5), 936-944.

Nutt, C. L., Mani, D. R., Betensky, R. A., Tamayo, P., Cairncross, J. G., Ladd, C., et al. (2003). Gene expression-based classification of malignant gliomas correlates better with survival than histological classification. *Cancer Res., 63*(7), 1602-1607.

Ohgaki, H., Dessen, P., Jourde, B., Horstmann, S., Nishikawa, T., Di Patre, P. L., et al. (2004). Genetic pathways to glioblastoma: A population-based study. *Cancer Res., 64*(19), 6892-6899.

Ohgaki, H., & Kleihues, P. (2007). Genetic pathways to primary and secondary glioblastoma. *Am.J.Pathol., 170*(5), 1445-1453.

Omuro, A., & DeAngelis, L. M. (2013). Glioblastoma and other malignant gliomas: A clinical review. *Jama, 310*(17), 1842-1850.

Omuro, A. M. P., Faivre, S., & Raymond, E. (2007). Lessons learned in the development of targeted therapy for malignant gliomas. *Molecular Cancer Therapeutics, 6*(7), 1909-1919.

Ostrom, Q. T., Gittleman, H., Farah, P., Ondracek, A., Chen, Y., Wolinsky, Y., et al. (2013). CBTRUS statistical report: Primary brain and central nervous system tumors diagnosed in the united states in 2006-2010. *Neuro Oncol., 15 Suppl 2*, ii1-56.

Pampaloni, F., Ansari, N., & Stelzer, E. H. (2013). High-resolution deep imaging of live cellular spheroids with light-sheet-based fluorescence microscopy. *Cell Tissue Res., 352*(1), 161-177.

Parsons, D. W., Jones, S., Zhang, X., Lin, J. C., Leary, R. J., Angenendt, P., et al. (2008). An integrated genomic analysis of human glioblastoma multiforme. *Science, 321*(5897), 1807-1812.

Phillips, H. S., Kharbanda, S., Chen, R., Forrest, W. F., Soriano, R. H., Wu, T. D., et al. (2006). Molecular subclasses of high-grade glioma predict prognosis, delineate a pattern of disease progression, and resemble stages in neurogenesis. *Cancer.Cell., 9*(3), 157-173.

Piaskowski, S., Bienkowski, M., Stoczynska-Fidelus, E., Stawski, R., Sieruta, M., Szybka, M., et al. (2011). Glioma cells showing IDH1 mutation cannot be propagated in standard cell culture conditions. *Br.J.Cancer, 104*(6), 968-970.

Portnow, J., Badie, B., Chen, M., Liu, A., Blanchard, S., & Synold, T. W. (2009). The neuropharmacokinetics of temozolomide in patients with resectable brain tumors: Potential implications for the current approach to chemoradiation. *Clin.Cancer Res., 15*(22), 7092-7098.

Schulte, A., Gunther, H. S., Martens, T., Zapf, S., Riethdorf, S., Wulfing, C., et al. (2012). Glioblastoma stem-like cell lines with either maintenance or loss of high-level EGFR amplification, generated via modulation of ligand concentration. *Clin.Cancer Res., 18*(7), 1901-1913.

Stupp, R., Gander, M., Leyvraz, S., & Newlands, E. (2001). Current and future developments in the use of temozolomide for the treatment of brain tumours. *Lancet Oncol., 2*(9), 552-560.

Stupp, R., Mason, W. P., van, d. B., Weller, M., Fisher, B., Taphoorn, M. J. B., et al. (2005). Radiotherapy plus concomitant and adjuvant temozolomide for glioblastoma. *N.Engl.J.Med., 352*(10), 987-996.

Sutherland, R. (1988). Cell and environment interactions in tumor microregions: The multicell spheroid model. *Science, 240*(4849), 177-184.

Verhaak, R. G., Hoadley, K. A., Purdom, E., Wang, V., Qi, Y., Wilkerson, M. D., et al. (2010). Integrated genomic analysis identifies clinically relevant subtypes of glioblastoma characterized by abnormalities in PDGFRA, IDH1, EGFR, and NF1. *Cancer.Cell., 17*(1), 98-110.

Vitucci, M., Hayes, D. N., & Miller, C. R. (2011). Gene expression profiling of gliomas: Merging genomic and histopathological classification for personalised therapy. *Br.J.Cancer, 104*(4), 545-553.

Zhao, S., Lin, Y., Xu, W., Jiang, W., Zha, Z., Wang, P., et al. (2009). Glioma-derived mutations in IDH1 dominantly inhibit IDH1 catalytic activity and induce HIF-1alpha. *Science, 324*(5924), 261-265.

Zheng, S., Chheda, M. G., & Verhaak, R. G. (2012). Studying a complex tumor: Potential and pitfalls. *Cancer J., 18*(1), 107-114.